

國立臺灣大學工學院材料科學與工程學系暨研究所



碩士論文

Department of Materials Science and Engineering

College of Engineering

National Taiwan University

Master Thesis

以第一原理與ReaxFF力場模擬計算探討矽氧碳陶瓷負  
極材料之微結構及鋰化機制

First-principles and ReaxFF Modeling and Simulations on the  
Structure and Lithiation Mechanism of Silicon Oxycarbide

闕立弘

Li-Hung Chueh

指導教授：郭錦龍 博士

Advisor: Chin-Lung Kuo, Ph.D.

中華民國 109 年 7 月

July, 2020



# 論文口試委員審定書



## 國立臺灣大學碩士學位論文 口試委員會審定書

論文中文題目：以第一原理與 ReaxFF 力場模擬計算探討矽  
氧碳陶瓷負極材料之微結構及鋰化機制

論文英文題目：First-principles and ReaxFF Modeling  
and Simulations on the Structure and  
Lithiation Mechanism of Silicon  
Oxycarbide

本論文係闕立弘君(R07527004)在國立臺灣大學材料  
科學與工程學系、所完成之碩士學位論文，於民國 109 年 7  
月 30 日承下列考試委員審查通過及口試及格，特此證明

口試委員：郭錦龍  
(指導教授)

吳鉉忠

許文東

林士剛

陳馨怡

系主任、所長

謝宗霖

(簽名)



## 致謝



從 2018 年 7 月入學到台大，到 2020 年 7 月口試結束，轉眼間碩士兩年的時光也悄悄來到尾聲。這兩年過程中，學習到了許多，也受到太多人的幫助，在此要致上最真誠的感謝，感謝這兩年間的一切。

首先最重要的就是指導教授，郭錦龍老師，從最基礎的模擬練習和搜尋文獻方法到第一原理計算研究技巧以及論文研究的進度討論，老師總是投注非常多時間與精力在訓練與培養我們的能力，不僅不遺餘力的授與我們許多與材料相關的物理知識，更在研究上給予我們很多寶貴的建議，真的非常感謝老師的指導。同時也要感謝口試委員吳鉉忠老師、許文東老師、林士剛老師與陳馨怡老師在口試時所給予的指導與建議，使我的論文更臻完整。另外也要感謝兩年來幾乎朝夕相處、同甘共苦的 304 研究室夥伴們。謝謝有仁、立毅學長在研究與課業上所提供的知識與建議；靖瑜、季紘、祐儀學長在碩一練習上的協助；霈聲、陳譽從碩一修課、練習到碩二的論文研究，一路以來的合作與陪伴，以及即將升上碩二的子郡、唐存、以喆在口試前後所提供的協助。最後，我要感謝我的家人、女友和朋友們，謝謝你們一直以來的支持、關心與鼓勵，讓我在壓力大的時候可以有人傾吐、分擔，更謝謝你們總是能給我力量讓我度過學習路上的重重關卡，最後完成碩士的研究與論文。

完成了這篇碩士論文後，也象徵著我的人生即將邁向一個新的里程碑。一路走來，酸甜苦辣或多或少都曾體會，也藉此學習到太多重要的知識、態度與待人處事的方法。期望在接下來的人生階段中，能謹記這段期間的所學，有勇氣面對並克服未來將遭遇的挑戰，努力活出獨一無二的精采人生。

## 摘要



本研究分別利用 ReaxFF 與第一原理模擬計算探討矽氧碳陶瓷負極材料之微結構，以及其碳氧濃度對其微結構之影響。接著利用第一原理計算進一步進行矽氧碳材料的電子結構以及鋰化機制的分析。

論文的第一部分，本文以 Ponomarev 等人的參數(UTA1)出發，進行參數的調整，並驗證這些參數對於各一元及二元對系統的結構、機械常數和內聚能的描述。基於以上性質的改善，由我們所調整得到的參數建置的結構中可以看到碳原子相較於 UTA1 參數所建置的非晶矽氧碳結構來說更傾向進到矽氧碳玻璃相中，因而使聚集碳相(free carbon phase)變得更加平整。另外原來 UTA1 參數對於系統中配位缺陷過高的容忍度也有所改善。有了以上的參數調整以及改善，利用我們所調整參數建置的非晶矽氧碳結構在熱力學穩定度上明顯優於由 UTA1 參數所建置的結構。

在第二部分中，本文利用第一原理計算產生六組不同濃度的矽氧碳結構，討論碳與氧濃度對微結構以及電子性質的影響。結果顯示當碳與氧的濃度下降時，聚集碳相的比例會隨之下降。此外，當碳濃度上升或是氧濃度下降時，系統中  $\text{SiC}_4$  與  $\text{SiC}_3\text{O}$  四面體的比例會隨之而上升，而  $\text{SiCO}_3$  與  $\text{SiO}_4$  四面體的比例會隨之而下降，致使系統的孔洞體積以及比表面積也因而降低。接著在電子性質方面，結果顯示碳原子的加入有效使矽氧碳玻璃相的能隙縮小，此外隨著氧濃度的降低，Si-C 與 Si-Si 鍵結在系統中的比例逐漸提升，造成能隙逐漸減小的現象。

在最後一部分的鋰化計算中，結果顯現矽氧碳的鋰化過程主要分為兩階段：第一階段電子主要填在聚集碳相的碳原子上而鋰離子吸附在聚集碳相與矽氧碳玻璃相的界面之間的氧原子上；第二階段電子開始填入矽氧碳玻璃相造成系統中明顯的 Si-O 斷鍵以及 Li-O 鍵結生成的現象。聚集碳相在鋰化過程中扮演著電子儲存槽以及緩衝系統體積膨脹的角色。最後，我們發現越高的碳濃度將驅使越高的電容量。此外高碳濃度以及低氧濃度將使矽氧碳系統在充放電可逆性上有較佳的表現。

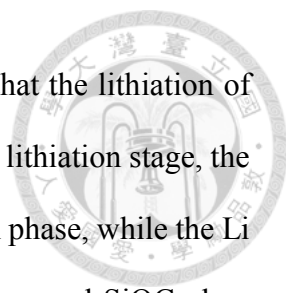
# Abstract



In this thesis, ReaxFF and first principles calculations are employed to explore the effect of carbon and oxygen contents on nanostructures of amorphous silicon oxycarbide (SiOC). The electronic structures as well as the lithiation mechanism are further studied by first principles calculations.

In the first part of this thesis, we modified the Si/O/C ReaxFF parameter set based on the parameters from Ponomarev et al. (UTA1), and validated its performance on lattice constants, elastic constants and cohesive energies of the unary and binary systems. Thanks to the calibrations above, the carbon atoms are more likely to be discovered in the SiOC glass phase, leading to the flatter free carbon phase in structures constructed via our new developed parameters. Moreover, the too-high tolerance of coordination defects in UTA1 is also improved. Finally, our new developed parameter set is able to construct the amorphous SiOC structures that are thermodynamically more stable than the structures built by UTA1 parameters.

In the second part of this thesis, we constructed amorphous SiOC structures in six different concentrations by first principles calculations to investigate the influences of carbon and oxygen contents on nanostructures and electronic structures of amorphous SiOCs. The results suggest that the decrease of carbon and oxygen contents will make the proportion of free carbon decrease. Furthermore, the increase of carbon concentration and the decrease of oxygen concentration will both induce the rising in the proportion of  $\text{SiC}_4$  and  $\text{SiC}_3\text{O}$  tetrahedra as well as the drop in the proportion of  $\text{SiCO}_3$  and  $\text{SiO}_4$  tetrahedra. In terms of electronic properties, the results show that the introduction of carbon atoms in SiOC glass effectively decrease the band gap. Besides, the decrease of oxygen concentration induces the increase in fractions of Si-C bond and Si-Si bond in the system, leading to the narrower band gaps in the SiOC glass region.



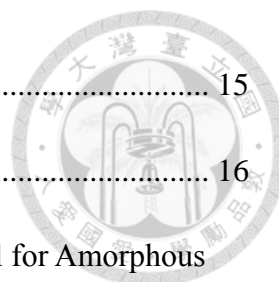
In the third part of this thesis, the lithiation calculations show that the lithiation of amorphous SiOCs can be roughly divided into two stages. In the first lithiation stage, the electrons from Li mostly fill the states on carbon atoms in free carbon phase, while the Li ions are absorbed on the oxygen atoms at the interface of free carbon and SiOC glass phase. In the second lithiation stage, Li ions start to interact with the SiOC glass phase with the electron from them fill the Si-O anti-bonding states, leading to the break of Si-O bonds and the formation of Li-O bonds. In the whole process, the carbon atoms in free carbon phase are keeping gaining electrons from Li, suggesting the role of reservoir of electrons that free carbon phase plays. Furthermore, the SiOCs with higher carbon concentrations present smaller relative volumes in the process of lithiation, indicating the function of limiting the volume expansions by free carbon phase. Finally yet importantly, the amorphous SiOCs with higher carbon concentration possess the higher theoretical capacities, and additionally, the high carbon concentration as well as the low oxygen concentration will make better performances of amorphous SiOCs on reversibility.



# Contents



致謝 .....	i
摘要 .....	ii
Abstract.....	iii
Contents.....	v
List of Figures.....	viii
List of Tables .....	xiii
Chapter 1    Introduction .....	1
Chapter 2    Theoretical Background .....	6
2.1      First principles calculation.....	6
2.2      Density functional theory (DFT) .....	6
2.2.1    Thomas-Fermi model .....	7
2.2.2    Hohenberg-Kohn theorem .....	8
2.2.3    Kohn-Sham equation .....	9
2.2.4    Exchange-correlation functional.....	10
2.2.5    Self-consistent field method .....	11
2.2.6    Pseudopotential.....	12
2.2.7    Dispersion corrections for density functional theory .....	12
2.3      Reactive Force Field (ReaxFF) .....	13
2.3.1    Introduction to ReaxFF.....	13
2.3.2    Potential parameters optimization .....	14
2.4      Molecular dynamics .....	15



2.4.1	Verlet algorithm.....	15
2.4.2	Nosé-Hoover thermostat.....	16
<b>Chapter 3 Development of Reactive Force Field Potential Model for Amorphous</b>		
<b>Silicon Oxycarbide .....</b> 20		
3.1	Introduction .....	20
3.2	Methodology.....	25
3.2.1	ReaxFF parametrization .....	25
3.2.2	Mechanical properties calculation.....	26
3.2.3	Melt-and-quench procedures to construct amorphous silicon oxycarbide .....	26
3.2.4	Computational details .....	29
3.3	Results and discussion.....	30
3.3.1	Validation of ReaxFF parameters.....	30
3.3.2	Structures of amorphous SiOC.....	35
3.3.3	Stability of amorphous SiOC.....	48
3.4	Summary.....	49
<b>Chapter 4 First-principles Study of the Structure and Electronic Properties of</b>		
<b>Amorphous Silicon Oxycarbide .....</b> 50		
4.1	Introduction .....	50
4.2	Computational details .....	52
4.2.1	Melt-and-quench procedures to construct amorphous silicon oxycarbide .....	52
4.2.2	Connolly Surface .....	54

4.2.3	SiO <sub>x</sub> C <sub>4-x</sub> tetrahedra and free carbon calculation .....	55
4.3	Results and discussion .....	56
4.3.1	Structures of amorphous SiOC .....	56
4.3.2	Free carbon distribution in amorphous SiOC .....	63
4.3.3	SiO <sub>x</sub> C <sub>4-x</sub> tetrahedra distribution in amorphous SiOC .....	66
4.3.4	Pore volume and specific surface area of SiOC .....	69
4.3.5	Electronic structures of SiOC .....	72
4.4	Summary .....	82
Chapter 5	Lithiation Mechanism of Amorphous Silicon Oxycarbide .....	83
5.1	Introduction .....	83
5.2	Computational details .....	85
5.3	Results and discussion .....	86
5.3.1	First lithiation stage of SiOC .....	86
5.3.2	Second lithiation stage of SiOC .....	94
5.3.3	Structural evolution during the lithiation process .....	98
5.3.4	Effects of carbon and oxygen contents on specific capacity .....	102
5.4	Summary .....	109
Chapter 6	Conclusions .....	110
Reference	.....	112
Appendix	.....	120

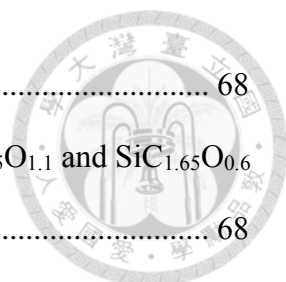


## List of Figures



Figure 1.1 Raman spectra of SiOC samples.....	5
Figure 1.2 <sup>29</sup> Si MAS NMR spectra of SiC <sub>0.68</sub> O <sub>1.5</sub> .....	5
Figure 3.1 Precursors of polymer-derived amorphous SiOC: (a) polysiloxane, (b) polystyrene, (c) divinylbenzene.....	23
Figure 3.2 Schematic representation of SiOC proposed by Sorarù et al. ....	23
Figure 3.3 Schematic representation of SiOC proposed by Saha et al. ....	24
Figure 3.4 Amorphous models of SiC <sub>2.2</sub> O <sub>1.6</sub> (192 atoms) generated via melt-and-quench MD simulation with a cooling rate of 1.25×10 <sup>13</sup> K/s starting from 5000 K: (a) DFT, (b) ReaxFF using UTA1 parameters. ....	24
Figure 3.5 Melt-and-quench procedure of amorphous SiOC construction .....	27
Figure 3.6 Flow chart of amorphous SiOC construction.....	28
Figure 3.7 The energy volume curve of diamond.....	32
Figure 3.8 The energy volume curve of graphite .....	32
Figure 3.9 The structure of SiC <sub>2.2</sub> O <sub>1.6</sub> constructed by the parameters developed in this work: (a) unit cell, (b) overview of the 2×2 supercell.....	38
Figure 3.10 The structure of SiC <sub>2.2</sub> O <sub>1.6</sub> constructed by UTA1: (a) unit cell, (b) overview of the 2×2 supercell .....	39
Figure 3.11 The structure of SiC <sub>1.65</sub> O <sub>1.6</sub> constructed by the parameters developed in this work: (a) unit cell, (b) overview of the 2×2 supercell.....	40
Figure 3.12 The structure of SiC <sub>1.65</sub> O <sub>1.6</sub> constructed by UTA1: (a) unit cell, (b) overview of the 2×2 supercell .....	41
Figure 3.13 The structure of SiC <sub>0.8</sub> O <sub>1.6</sub> constructed by the parameters developed in this work: (a) unit cell, (b) overview of the 2×2 supercell.....	42
Figure 3.14 The structure of SiC <sub>0.8</sub> O <sub>1.6</sub> constructed by UTA1: (a) unit cell, (b) overview	

of the 2×2 supercell .....	43
Figure 3.15 The structure of $\text{SiC}_{1.65}\text{O}_{0.6}$ constructed by the parameters developed in this work: (a) unit cell, (b) overview of the 2×2 supercell.....	44
Figure 3.16 The structure of $\text{SiC}_{1.65}\text{O}_{0.6}$ constructed by UTA1: (a) unit cell, (b) overview of the 2×2 supercell .....	45
Figure 3.17 Atomistic coordination distribution of $\text{SiC}_{2.2}\text{O}_{1.6}$ : (a) this work, (b) UTA1	46
Figure 3.18 Atomistic coordination distribution of $\text{SiC}_{1.65}\text{O}_{1.6}$ : (a) this work, (b) UTA1 .....	46
Figure 3.19 Atomistic coordination distribution of $\text{SiC}_{0.8}\text{O}_{1.6}$ : (a) this work, (b) UTA1	47
Figure 3.20 Atomistic coordination distribution of $\text{SiC}_{0.8}\text{O}_{1.6}$ : (a) this work, (b) UTA1	47
Figure 4.1 Amorphous SiOC structures: (a) $\text{SiC}_{1/3}\text{O}_{4/3}$ , (b) $\text{SiC}_{2/5}\text{O}_{6/5}$ , (c) $\text{SiCO}_{6/5}$ , (d) $\text{SiC}_{8/5}\text{O}_{6/5}$ , (e) $\text{SiC}_{11/5}\text{O}_{6/5}$ .....	51
Figure 4.2 The structure of $\text{SiC}_{2.43}\text{O}_{1.5}$ .....	51
Figure 4.3 Schematic illustration of Connolly surface .....	54
Figure 4.4 $\text{SiO}_x\text{C}_{4-x}$ tetrahedra: (a) $\text{SiC}_4$ , (b) $\text{SiC}_3\text{O}$ , (c) $\text{SiC}_2\text{O}_2$ , (d) $\text{SiCO}_3$ , (e) $\text{SiO}_4$ ...	55
Figure 4.5 The structure of $\text{SiC}_{3.3}\text{O}_{1.6}$ : (a) unit cell, (b) overview of the 2×2 supercell.	57
Figure 4.6 The structure of $\text{SiC}_{2.2}\text{O}_{1.6}$ : (a) unit cell, (b) overview of the 2×2 supercell.	58
Figure 4.7 The structure of $\text{SiC}_{1.65}\text{O}_{1.6}$ : (a) unit cell, (b) overview of the 2×2 supercell	59
Figure 4.8 The structure of $\text{SiC}_{0.8}\text{O}_{1.6}$ : (a) unit cell, (b) overview of the 2×2 supercell.	60
Figure 4.9 The structure of $\text{SiC}_{1.65}\text{O}_{1.1}$ : (a) unit cell, (b) overview of the 2×2 supercell	61
Figure 4.10 The structure of $\text{SiC}_{1.65}\text{O}_{0.6}$ : (a) unit cell, (b) overview of the 2×2 supercell .....	62
Figure 4.11 Free carbon proportions of $\text{SiC}_{3.3}\text{O}_{1.6}$ , $\text{SiC}_{2.2}\text{O}_{1.6}$ , $\text{SiC}_{1.65}\text{O}_{1.6}$ and $\text{SiC}_{0.8}\text{O}_{1.6}$ .....	65
Figure 4.12 Free carbon proportions of $\text{SiC}_{1.65}\text{O}_{1.6}$ , $\text{SiC}_{1.65}\text{O}_{1.1}$ and $\text{SiC}_{1.65}\text{O}_{0.6}$ .....	65
Figure 4.13 Distributions of $\text{SiO}_x\text{C}_{4-x}$ tetrahedra in $\text{SiC}_{3.3}\text{O}_{1.6}$ , $\text{SiC}_{2.2}\text{O}_{1.6}$ , $\text{SiC}_{1.65}\text{O}_{1.6}$ and	



SiC<sub>0.8</sub>O<sub>1.6</sub>..... 68

Figure 4.14 Distributions of SiO<sub>x</sub>C<sub>4-x</sub> tetrahedra in SiC<sub>1.65</sub>O<sub>1.6</sub>, SiC<sub>1.65</sub>O<sub>1.1</sub> and SiC<sub>1.65</sub>O<sub>0.6</sub> ..... 68

..... 68

Figure 4.15 The microporous space in: (a) SiC<sub>3.3</sub>O<sub>1.6</sub>, (b) SiC<sub>2.2</sub>O<sub>1.6</sub>, (c) SiC<sub>1.65</sub>O<sub>1.6</sub>, (d) SiC<sub>0.8</sub>O<sub>1.6</sub>, (e) SiC<sub>1.65</sub>O<sub>1.1</sub>, (f) SiC<sub>1.65</sub>O<sub>0.6</sub>, ..... 70

Figure 4.16 (a) pore volume and, (b) specific surface area of SiC<sub>3.3</sub>O<sub>1.6</sub>, SiC<sub>2.2</sub>O<sub>1.6</sub>, SiC<sub>1.65</sub>O<sub>1.6</sub> and SiC<sub>0.8</sub>O<sub>1.6</sub>..... 71

Figure 4.17 (a) pore volume and, (b) specific surface area of SiC<sub>1.65</sub>O<sub>1.6</sub>, SiC<sub>1.65</sub>O<sub>1.1</sub> and SiC<sub>1.65</sub>O<sub>0.6</sub> ..... 71

Figure 4.18 Local density of state of SiC<sub>3.3</sub>O<sub>1.6</sub> ..... 73

Figure 4.19 Local density of state of SiC<sub>2.2</sub>O<sub>1.6</sub> ..... 73

Figure 4.20 Local density of state of SiC<sub>1.65</sub>O<sub>1.6</sub> ..... 74

Figure 4.21 Local density of state of SiC<sub>0.8</sub>O<sub>1.6</sub> ..... 74

Figure 4.22 Local density of state of SiC<sub>1.65</sub>O<sub>1.1</sub> ..... 75

Figure 4.23 Local density of state of SiC<sub>1.65</sub>O<sub>0.6</sub>..... 75

Figure 4.24 The charge distribution of SiC<sub>3.3</sub>O<sub>1.6</sub> in the range between: (a) E-E<sub>f</sub>= -1.5 ~ 0 eV, (b) E-E<sub>f</sub>= 0 ~ 1.6 eV ..... 76

Figure 4.25 The charge distribution of SiC<sub>2.2</sub>O<sub>1.6</sub> in the range between: (a) E-E<sub>f</sub>= -1.7 ~ 0 eV, (b) E-E<sub>f</sub>= 0 ~ 1.7 eV ..... 77

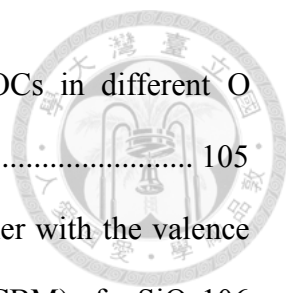
Figure 4.26 The charge distribution of SiC<sub>1.65</sub>O<sub>1.6</sub> in the range between: (a) E-E<sub>f</sub>= -1.6 ~ 0 eV, (b) E-E<sub>f</sub>= 0 ~ 1.7 eV ..... 78

Figure 4.27 The charge distribution of SiC<sub>0.8</sub>O<sub>1.6</sub> in the range between: (a) E-E<sub>f</sub>= -1.0 ~ 0 eV, (b) E-E<sub>f</sub>= 0 ~ 2.0 eV ..... 79

Figure 4.28 The charge distribution of SiC<sub>1.65</sub>O<sub>1.1</sub> in the range between: (a) E-E<sub>f</sub>= -0.5 ~ 0 eV, (b) E-E<sub>f</sub>= 0 ~ 0.7 eV ..... 80

Figure 4.29 The charge distribution of SiC<sub>1.65</sub>O<sub>1.1</sub> in the range between E-E<sub>f</sub>= 0 ~ 0.7 eV

.....	81
Figure 5.1 Lithiation/delithiation capacity and Coulombic efficiency of $\text{SiC}_{7.78}\text{O}_{0.51}$ ...	84
Figure 5.2 Formation of $\text{Li}_x\text{O}$ and $\text{Li}_y\text{Si}$ in $\text{Li}_2\text{SiC}_{2/5}\text{O}_{6/5}$ .....	84
Figure 5.3 Structure of the first stage lithiated $\text{SiC}_{2.2}\text{O}_{1.6}$ .....	88
Figure 5.4 Structure of the first stage lithiated $\text{SiC}_{1.65}\text{O}_{1.6}$ .....	88
Figure 5.5 Structure of the first stage lithiated $\text{SiC}_{0.8}\text{O}_{1.6}$ .....	89
Figure 5.6 Structure of the first stage lithiated $\text{SiC}_{1.65}\text{O}_{0.6}$ .....	89
Figure 5.7 Local density of state of the first stage lithiated SiOCs: (a) $\text{SiC}_{2.2}\text{O}_{1.6} + 21\text{Li}$ , (b) $\text{SiC}_{1.65}\text{O}_{1.6} + 21\text{Li}$ , (c) $\text{SiC}_{0.8}\text{O}_{1.6} + 6\text{Li}$ , (d) $\text{SiC}_{1.65}\text{O}_{0.6} + 21\text{Li}$ .....	90
Figure 5.8 Charge gain in the first stage lithiated $\text{SiC}_{2.2}\text{O}_{1.6}$ .....	91
Figure 5.9 Charge gain in the first stage lithiated $\text{SiC}_{1.65}\text{O}_{1.6}$ .....	91
Figure 5.10 Charge gain in the first stage lithiated $\text{SiC}_{0.8}\text{O}_{1.6}$ .....	92
Figure 5.11 Charge gain in the first stage lithiated $\text{SiC}_{1.65}\text{O}_{0.6}$ .....	92
Figure 5.12 Distribution of charge gain of the first stage lithiated SiOCs: (a) $\text{SiC}_{2.2}\text{O}_{1.6} + 21\text{Li}$ , (b) $\text{SiC}_{1.65}\text{O}_{1.6} + 21\text{Li}$ , (c) $\text{SiC}_{0.8}\text{O}_{1.6} + 6\text{Li}$ , (d) $\text{SiC}_{1.65}\text{O}_{0.6} + 21\text{Li}$ .....	93
Figure 5.13 Schematic representation of electric field generated after the first stage lithiation in amorphous SiOCs .....	95
Figure 5.14 Fully lithiated structure of $\text{SiC}_{2.2}\text{O}_{1.6}$ .....	96
Figure 5.15 Fully lithiated structure of $\text{SiC}_{1.65}\text{O}_{1.6}$ .....	96
Figure 5.16 Fully lithiated structure of $\text{SiC}_{0.8}\text{O}_{1.6}$ .....	97
Figure 5.17 Fully lithiated structure of $\text{SiC}_{1.65}\text{O}_{0.6}$ .....	97
Figure 5.18 Average coordination numbers of: (a) O-Si, (b) O-Li in lithiated amorphous SiOCs.....	100
Figure 5.19 Structure of $\text{Li}_6\text{O}$ complex .....	101
Figure 5.20 Relative volume of lithiated amorphous SiOCs, Si and $\text{SiO}_{1/3}$ .....	101
Figure 5.21 (a) Formation energies of lithiated SiOCs, (b) voltage of lithiated SiOCs in	



different C concentrations, (c) voltage of lithiated SiOCs in different O concentrations..... 105

Figure 5.22 alignment of Si dangling bond, O dangling bond together with the valence band maximum (VBM) and conduction band minimum (CBM) of a-SiO<sub>2</sub> 106

Figure 5.23 Local density of state of fully lithiated SiC<sub>2.2</sub>O<sub>1.6</sub>..... 106

Figure 5.24 Local density of state of fully lithiated SiC<sub>1.65</sub>O<sub>1.6</sub>..... 107

Figure 5.25 Local density of state of fully lithiated SiC<sub>0.8</sub>O<sub>1.6</sub>..... 107

Figure 5.26 Local density of state of fully lithiated SiC<sub>1.65</sub>O<sub>0.6</sub>..... 108



# List of Tables



Table 3.1 Atomistic compositions of SiOC samples .....	29
Table 3.2 Validation of structural properties at 0 K of diamond and graphite.....	33
Table 3.3 Validation of mechanical properties of diamond and graphite .....	33
Table 3.4 Validation of structural properties at 0 K of SiO <sub>2</sub> and SiC .....	34
Table 3.5 Validation of mechanical properties of SiO <sub>2</sub> and SiC.....	34
Table 3.6 The formation energy of amorphous SiOC.....	48
Table 4.1 Atomistic compositions of SiOC samples .....	53
Table 4.2 Fraction of Si-C bond, fraction of Si-Si bond and band gap of amorphous SiOCs .....	81
Table 5.1 Charge gain in different atoms of fully lithiated SiOCs .....	108
Table 5.2 Capacities and reversibility of the amorphous SiOCs .....	108

# Chapter 1 Introduction



Lithium-ion batteries (LIBs) are currently the most popular and promising choice for powering portable electronic devices, electric vehicles as well as various applications of energy storage <sup>[1]-[4]</sup>. The capacity of LIBs are theoretically limited by the electrodes materials. Nowadays, the most commonly used anode in LIBs is graphite on account of its stable cycle ability, high Coulombic efficiency and structural stability <sup>[5]</sup>. However, the crucial drawback of relatively low reversible capacity (372 mAh/g) limits its application in high-energy-density batteries <sup>[6]-[8]</sup>.

To meet the need of high power density, silicon, which presents a high specific capacity of 3579 mAh/g is an attractive candidate for the next generation anode in LIBs, but the severe volume expansion (up to 400%) during lithium insertion and extraction causes tremendous mechanical issues in the practical utilization of silicon anodes <sup>[9]</sup>. <sup>[9]</sup>. In fact, capacity and structural stability are mutually exclusive properties of most electrodes <sup>[11]</sup>. To mitigate the structural failure of high-capacity electrodes, several efforts have been made, such as silicon-carbon composite and some novel hybrid chemistries <sup>[12]-[17]</sup>. Nevertheless, large capacity loss and the continuous shedding of Si during the charge-discharge cycles still remain a great challenge for these clever designs of composite structures.

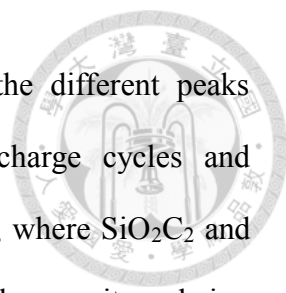
Among several alternatives, polymer-derived silicon oxycarbide (SiOC) ceramics present high temperature stability and the ability to store the lithium reversibly. They deliver a remarkable reversible capacity of around 600 mAh/g and are believed to be promising anode materials for next generation LIBs <sup>[18]-[26]</sup>.

SiOCs belong to the branch of polymer-derived ceramics (PDC), which are obtained from preceramic polymers through a pyrolysis process in controlled temperature and atmosphere <sup>[27]</sup>. SiOC glasses are derived from cross-linked polysiloxanes. After

pyrolysis at  $T \geq 800^\circ\text{C}$  in an inert atmosphere, the precursors will form a SiOC phase and the excessive carbon atoms are transformed into a  $\text{sp}^2$  carbon phase, which is usually called the free carbon phase.

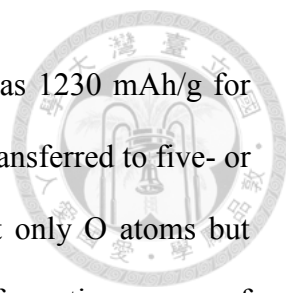
Amorphous SiOC ceramics consist of three main characteristic structures, which are free carbon, SiOC glasses mentioned above, and finally micropores [22]. First, for the free carbon phase, Wilamowska-Zawlocka et al. [28] synthesized several SiOC samples in different compositions, and there are clear D and G bands in the Raman spectra of them as shown in Figure 1.1. The G band represents the in-plane bond-stretching motion of  $\text{sp}^2$  carbons, whereas the D band is related to disorder in graphitic layers and is not observed in perfect graphite [29]-[32]. Thus, it can be inferred that the free carbon phase is similar to graphite-like amorphous carbon. Secondly, the SiOC glass phase comprises a random network of Si-O and Si-C bonds forming mixed  $\text{SiO}_x\text{C}_{4-x}$  (where  $0 \leq x \leq 4$ ) tetrahedra, which we can see from the peaks in  $^{29}\text{Si}$  MAS NMR spectra of  $\text{SiC}_{0.68}\text{O}_{1.5}$  presented by Mera et al. [33] in Figure 1.2. Finally, the micropores are located in the SiOC glass phase as well as the interface between free carbon and SiOC glass phase.

It is believed that the high capacity of SiOC ceramics is attributed to the amorphous nanodomain structure. However, the major source of capacity in the system still remains controversial. For example, David et al. [34] designed a SiOC glass-graphene composite paper electrode, which delivered a charge capacity of  $\sim 588$  mAh/g at 1020th cycle. They owed the high reversible capacity of the polymer-derived SiOC to all the three main characteristic structures instead of specifying one of them as the major capacity source. Fukui et al. [22], on the other hand, showed that the major charge capacity of SiOC ceramics came from the free carbon phase, and the lithium storage site could be interstitial spaces or edges of graphene layers. Similarly, Wilamowska-Zawlocka et al. [28] and Dibandjo [35] both indicated that the capacities of SiOC ceramics are strongly related to the carbon content and that the free carbon phase is the major lithiation site. Nevertheless,



Liu et al. [36] used  $^{29}\text{Si}$  MAS NMR to observe the change of the different peaks corresponding to distinct  $\text{SiO}_x\text{C}_{4-x}$  tetrahedra during charge-discharge cycles and considered that SiOC glass phase serves as the major lithiation site, where  $\text{SiO}_2\text{C}_2$  and  $\text{SiO}_3\text{C}$  provide reversible capacity while the others provide irreversible capacity or being inactive to lithium. Lastly, Graczyk-Zajac et al. [37] suggested that the mixed Si-O and Si-C bonds in SiOC would induce the formation of more disordered carbon phase, which thereby increase the reversible storage of Li ions. Hence, it can be concluded that there is an effect of SiOC glass on the Li-storage capacity of the material.

For theoretical studies, Liao et al. [38], [39] sequentially utilized classical force field (Tersoff potential [40]) and first principles molecular dynamics (MD) calculations to construct the initial SiOC system. During the construction, Tersoff potential and the parameters for SiC and  $\text{SiO}_2$  [40], [41] was applied in the first stage, which was melt-and-quench MD. The first principles simulations were then performed to optimize the SiOC structures followed by annealing and final geometry optimization. Later, after conducting the whole lithiation process by first principles calculations, the theoretical specific capacity was predicted around 1400 mAh/g for  $\text{SiC}_{0.4}\text{O}_{1.2}$ . They claimed that the  $\text{Li}_2\text{O}$  would form at the beginning of lithiation with the breaking of Si-O bonds. Then,  $\text{Li}_x\text{O}$  and  $\text{Li}_y\text{Si}$  would form with the increasing of Li concentration, which made the major contribution to the capacity of SiOC. Besides, the carbon segregation made small contributions on lithium storage, and stabilized the whole system by forming three-dimensional network, resulting in small volume expansion and stable mechanical properties during lithiation. Sun et al. [11], on the other hand, used evolutionary algorithm implemented in the USPEX program [42] to construct the initial SiOC structure instead of carrying out melt-and-quench MD, and annealed the whole amorphous cell by ab initio MD. They suggested that the two-step lithiation was proceeded by the absorption of Li at the nanovoid sites, followed by the chemical interactions of Li with the  $\text{SiO}_x\text{C}_{4-x}$



tetrahedral units and the C phase, and the full lithiation capacity was 1230 mAh/g for  $\text{SiC}_{2.43}\text{O}_{1.5}$ . During the lithiation process, the electron from lithium transferred to five- or seven-membered rings in graphene-like C network and around not only O atoms but unsaturated C atoms in SiOC glass regime. Kroll <sup>[43]</sup> compared the formation energy of one lithium inserted to amorphous  $\text{SiO}_2$ , amorphous SiOC without free carbon and amorphous SiOC with free carbon respectively, and stated that free carbon in the SiOC ceramic provides low-lying unoccupied states where electrons could go.

Although the experiments above provide some information on the nanostructures of SiOCs, the major source of capacity in the system remains contentious. Moreover, how the actual nano-structure of SiOC would be? How many of carbon atoms will be in the so-called free carbon phase and SiOC glasses phase respectively? How the carbon and oxygen concentration influence the structure as well as lithiation process? And what is the optimal composition of SiOC? In order to gain clear pictures of the role of C and O atoms in SiOC system and the lithiation mechanism of SiOC, a thorough study of the configuration of different SiOC composition and the related lithiation procedure should be carefully done.

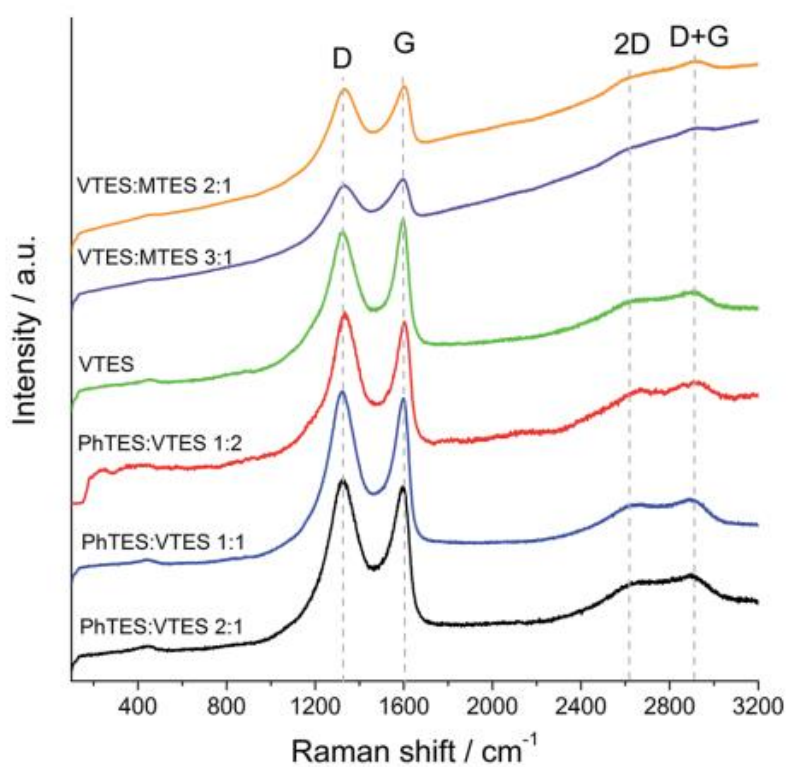


Figure 1.1 Raman spectra of SiOC samples [28]

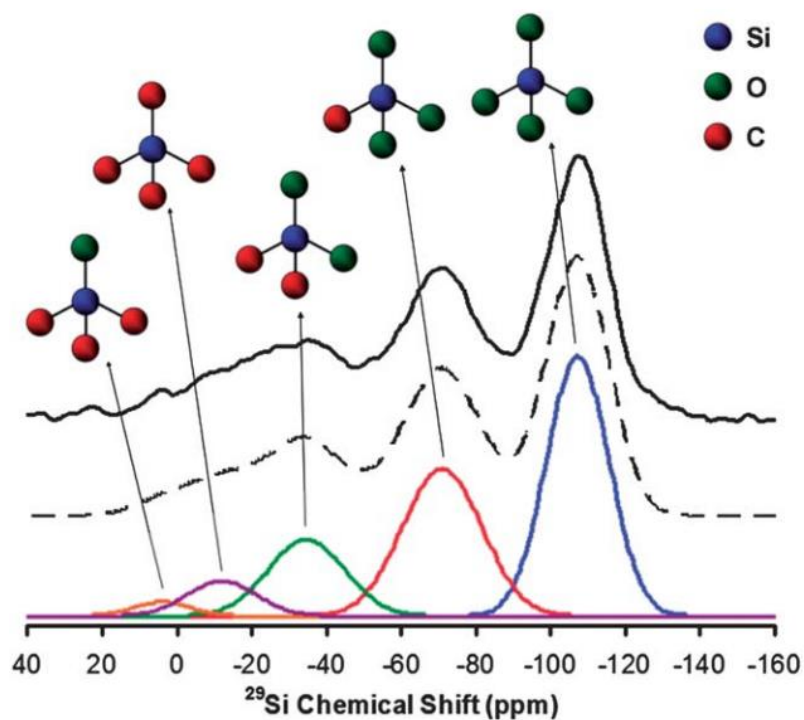


Figure 1.2  $^{29}\text{Si}$  MAS NMR spectra of  $\text{SiC}_{0.68}\text{O}_{1.5}$  [33]

## Chapter 2 Theoretical Background



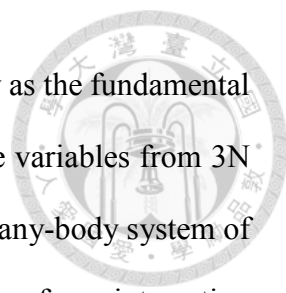
### 2.1 First principles calculation

First principles calculation, also known as *ab initio* simulation, is based on the fundamental laws of physics without any empirical or semi-empirical parameters. With given composition and the position of atoms, properties and electronic structures of materials can be obtained by directly solving Schrödinger equation. Therefore, first principles calculation is now widely used to investigate systems that are hard to perform experiments or lack of experimental data.

In most of the cases, analytic solutions of Schrödinger equation are too complicated to be obtained. Thus, several assumptions and approximations are applied in first principles calculation, such as Born-Oppenheimer approximation. However, even with the various approximations, the scales in both system size and simulation time are confined to a few hundred atoms and tens to hundreds of picoseconds ( $10^{-12}$  s) by the computing devices. If larger systems or longer simulation time are of interest, the use of other computational methods, such as classical force field, is often required.

### 2.2 Density functional theory (DFT)

There are several ways to solve the Schrödinger equation. For example, Hartree-Fock theory deals directly with the many-body wavefunction. However, the computational cost increases with the order of  $3N$ , where  $N$  represents the number of electrons in the system. Thus, this kind of methods seems not efficient enough to be applied on large systems.



Density functional theory (DFT), however, uses electron density as the fundamental property instead of many-body wavefunction, which can reduced the variables from  $3N$  to  $x, y, z$  -only three variables. In DFT calculations, the intractable many-body system of electrons interacting in a static external potential is reduced to a system of non-interacting electrons moving in the effective potential. With simplified calculations, properties of large systems can be obtained much more efficiently.

Density functional theory (DFT) is developed by Hohenberg, Kohn, and Sham in 1960s with its fundamental concepts originated from the Thomas-Fermi model. Nowadays, DFT is wildly used in various field, such as physics, chemistry and materials science. However, there are still some drawbacks in DFT calculations, such as the underestimation of band gap energy and the lack of precise intermolecular forces, especially the van der Waals force. Therefore, several efforts, such as modifying the exchange-correlation functional or adding semi-empirical functions, are having been made to overcome these problems.

### 2.2.1 Thomas-Fermi model

In conventional quantum mechanics, the  $n$ -electron Hamiltonian of a system can be represented as followed:

$$\hat{H} = [\hat{T} + \hat{V} + \hat{U}] = \left[ \sum_i^N \left( -\frac{\hbar^2}{2m} \nabla_i^2 \right) + \sum_i^N V(\vec{r}_i) + \sum_i^N U(\vec{r}_i, \vec{r}_j) \right] \quad (\text{eq. 2-1})$$

Here,  $\hat{T}$  stands for kinetics energy of electrons;  $\hat{V}$  stands for external potential originated from the positively charged nuclei, and  $\hat{U}$  stands for potential between electrons. Since this Hamiltonian is calculated by summing the kinetic energy and potential energy of all the particles in the system, it would be too arduous to deal with large systems.



The Thomas-Fermi model proposed by Thomas and Fermi in 1927 is viewed as the precursor to modern DFT.<sup>[44], [45]</sup> The Thomas-Fermi model treated kinetics energy of electrons as a functional of the electron density. The total energy is calculated by summing the functional and Coulombic electrostatic between particles, which is represented as

$$E = C_f \int [\rho(r)]^{5/3} dr + \int \rho(r) V_N(r) dr + \frac{e^2}{2} \int \frac{\rho(r)\rho(r')}{|r-r'|} dr^3 dr'^3$$

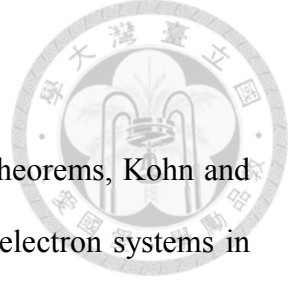
(eq. 2-2)

In the above equation, the first term represents the kinetics energy, which is approximated using charge potential in this model. The second term is the contribution of electron-core interaction. The final term stands for interactions between electrons.

The Thomas-Fermi model can reduce the computational cost to solve the Schrödinger equation. However, the lack of including exchange-correlation energy and Pauli exclusion principle inevitable limits the calculation accuracy. Although Dirac thereafter attempted to add an exchange energy functional term to correct the model in 1930, it can still not meet the demand of accuracy.

## 2.2.2 Hohenberg-Kohn theorem

Hohenberg and Kohn derived two Hohenberg-Kohn theorems, which laid the foundation of density functional theory in 1964.<sup>[46]</sup> The first Hohenberg-Kohn theorem states that with a given external potential, the total energy of the system is a unique function of charge density. The second Hohenberg-Kohn theorem describes that the electron density of a ground state system is the one that brings about the minimum total energy. Once the ground state wave function of a system is solved, the properties of it can be obtained. However, Hohenberg and Kohn did not provide an efficient way to calculate the ground state charge density. It is Kohn and Sham that proposed a method to perform the DFT calculations.



### 2.2.3 Kohn-Sham equation

Based on the Thomas-Fermi model and the Hohenberg-Kohn theorems, Kohn and Sham developed a method to achieve the calculations of the multi-electron systems in 1965, the Kohn-Sham equation.<sup>[47]</sup> The equation simplifies the system described by many body Schrödinger equation into a non-interacting system affected by an effective external potential generated by nuclei.

The main difficulty to separate a multi-electron system into single-particle equations is due to the term  $\hat{U}$  in eq. 2-1. The Kohn-Sham equation deals with electron density,  $n(\vec{r})$ , instead of  $\hat{U}$ . In Kohn-Sham equation the wave function is separated to single-electron wave functions, which is also called Kohn-Sham orbitals. It could be represented by

$$\Psi(\vec{r}_1, \dots, \vec{r}_N) = \prod_i^N \psi_i(\vec{r}_i) \quad (\text{eq. 2-3})$$

The electron density can be obtained by the summation of wave function squares.

$$n(\vec{r}) = \sum_i^N |\Psi_i(\vec{r}_i)|^2 \quad (\text{eq. 2-4})$$

The kinetics energy and the effective potential energy can be represented as functional of the electron density. Thus, the Kohn-Sham equation is expressed as

$$\left( -\frac{\hbar^2}{2m_e} \nabla^2 + V_{eff}(\vec{r}) \right) \Psi_i(\vec{r}) = \varepsilon_i \Psi_i(\vec{r}) \quad (\text{eq. 2-5})$$

where  $\varepsilon_i$  is the energy of Kohn-Sham orbital. The total energy of the system becomes

$$E_T[n(\vec{r})] = T[n(\vec{r})] + V_{ext}(\vec{r}) + V_H[n(\vec{r})] + E_{xc}[n(\vec{r})] \quad (\text{eq. 2-6})$$

The last term  $E_{xc}[n(\vec{r})]$  is the exchange-correlation energy of electrons, which will be discussed in the later part. The effective potential can be derived by minimizing the total energy with variational principles.

$$V_{eff}n(\vec{r}) = V_{ext}n(\vec{r}) + \int d\vec{r}' \frac{n(\vec{r}')}{|\vec{r} - \vec{r}'|} + V_{xc}[n(\vec{r})] \quad (\text{eq. 2-7})$$

By solving Schrödinger equation using the above presentation for potentials, the wave function and electron density can be obtained.

## 2.2.4 Exchange-correlation functional

The exchange-correlation functional term,  $E_{xc}[n(\vec{r})]$ , is a vital part in Kohn-Sham potential. It corrects the error while expanding one-electron systems to multi-electrons systems. In fact, the low accuracy of conventional Thomas-Fermi model is due to the lack of this term. This term includes the exchange energies, which is originated from Pauli's exclusion principle, and the correlation energies, which describe the interaction between electrons in different orbitals. There are two kinds of widely used method, local density approximation (LDA) and generalized gradient approximation (GGA).

### a. Local Density Approximation (LDA)

In this model, the exchange-correlation energies are described as the functionals of the electronic densities.

$$E_{xc}^{LDA}[n] = E_{xc}^{LDA}[n(\vec{r})] \quad (\text{eq. 2-8})$$

In the above equation,  $n(\vec{r})$  is electron density of a certain points in the space. LDA can provide enough accuracy, and the most commonly used methods are CA-PZ for LDA.

b. Generalized Gradient Approximation (GGA)

Not only electron density, but also its gradient is considered in GGA model.

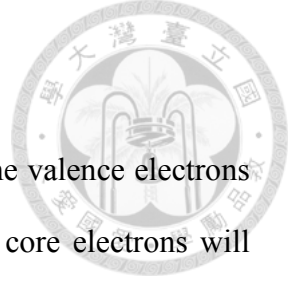
$$E_{xc}^{GGA}[n] = E_{xc}^{GGA}[n(\vec{r}), \nabla n(\vec{r})] \quad (\text{eq. 2-9})$$

There are several kinds of GGA. Two of the most popular functionals are PBE and PW91. In this work PBE is used to perform all calculations. With the exchange-correlation functional, the Schrödinger equation can be solved using the self-consistent scheme.

### 2.2.5 Self-consistent field method

As mentioned above, self-consistent field method is performed to solve the electron density and total energy. The scheme is sketched in Figure 2.1. First, an initial guess for electron density ( $\rho_{in}(r)$ ) is proposed then the corresponding effective Kohn-Sham equation can be determined based on it. The new Kohn-Sham orbitals can be derived by the effective Kohn-Sham equation, and thus the new charge density can be obtained. The new electron density can served as the new initial guess and repeat the cycle.

After several cycles, the difference between initial guess and final produced electron density gradually decreases. Once the difference goes lower than the tolerance set, the converged charge density can be obtained. The electronic properties can be further calculated by the charge density derived from wave functions, which are calculated by self-consistence field method.



## 2.2.6 Pseudopotential

While calculating properties of materials in DFT calculation, the valence electrons play a more critical role than core electrons. The consideration of core electrons will rarely increase the calculation accuracy but significantly raise the computation cost. Thus, pseudopotential is often used to simplify the system by eliminating core states.<sup>[48]</sup> In Figure 2.2 Schematic diagram of pseudopotential, the dashed lines are the exact wave function and potential, while the solid lines are the pseudo wave function and pseudopotential. The core states inside the critical distance  $r_c$  are replaced by a smooth, nodeless wave function, so the computational time can be greatly saved.

The projector augmented wave method (PAW) is a generalization of linear augmented-plane-wave and pseudopotential. With PAW, the wave functions near nuclei are described more accurately, which is necessary for calculations of Born effective charge or the dielectric functions.

## 2.2.7 Dispersion corrections for density functional theory

As mentioned above, traditional DFT fails to describe the long-range dispersion interactions. Thus, several methods are proposed to fix this problem. There are two categories of methods to calculate long-range dispersion interactions. The first type is semi empirical methods, such as D2, D3 methods proposed by Grimme *et al.* In this thesis, D2 method is used to calculate long-range interaction. The formula of D2 is expressed as

$$E_{D2} = -\frac{1}{2} \sum_{i=1}^{N_{at}} \sum_{j=1}^{N_{at}} \sum_L' \frac{C_{6ij}}{r_{ij,L}^6} f_{d,6}(r_{ij,L})$$

(eq. 2-10)

The summations are over all atoms  $N_{at}$  and all translations of the unit cell  $L$ . The prime indicates that  $i \neq j$  for  $L = 0$  to avoid calculating the dispersion interaction

within the same atoms.  $C_{6ij}$  denotes the dispersion coefficient between atom  $i$  and  $j$ .  $r_{ij,L}$  is the distance between atom  $i$  in the center cell and  $j$  in the cell  $L$ .  $f_{d,6}(r_{ij})$  is a damping function that minimize the dispersion interaction within typical bonding distances.  $f_{d,6}(r_{ij})$  can be expressed as

$$f_{d,6}(r_{ij}) = \frac{S_6}{1 + e^{-d\left(\frac{r_{ij}}{(S_R R_{0ij})} - 1\right)}} \quad (\text{eq. 2-11})$$

The  $S_6$  in the above equation is a global scaling factor, and  $d$  is the damping factor.

The second one, instead of adding an semi empirical term to potential, a non-local correlation functional is included for calculating dispersion interactions. This type includes vdW-DF2, optPBE-vdW, optB88-vdW, and optB86b-vdW.

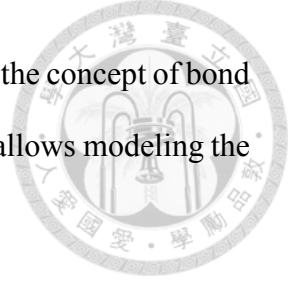
## 2.3 Reactive Force Field (ReaxFF)

### 2.3.1 Introduction to ReaxFF

The ReaxFF is developed for organic system like C/H systems initially by van Duin et al. [49] in 2001, and later modified by Chenoweth et al. [50] in 2008. Most of the simulation packages utilize this functional form, and the user-reaxc package in LAMMPS [51], [52] is a revision from the Aktulga et al.'s implementation [52]. The corresponding parameter description can be found in the supporting information of Chenoweth et al.'s paper.

The energy function of ReaxFF is composed of the following parameters

$$\begin{aligned} E_{system} = & E_{bond} + E_{lp} + E_{over} + E_{under} + E_{val} \\ & + E_{pen} + E_{coa} + E_{C2} + E_{triple} + E_{tors} + E_{conj} \\ & + E_{H-bond} + E_{vdWaals} + E_{Coulomb} \end{aligned} \quad (\text{eq. 2-12})$$



Distinct from the other force field potentials, the ReaxFF applies the concept of bond order (BO) expressed below on describing the energy surface, which allows modeling the bond-breaking events during simulations.

$$\begin{aligned} BO'_{ij} &= BO'_{ij}{}^{\sigma} + BO'_{ij}{}^{\pi} + BO'_{ij}{}^{\pi\pi} \\ &= \exp\left[p_{bo,1}\left(\frac{r_{ij}}{r_0^{\sigma}}\right)^{p_{bo,2}}\right] + \exp\left[p_{bo,3}\left(\frac{r_{ij}}{r_0^{\pi}}\right)^{p_{bo,4}}\right] + \exp\left[p_{bo,5}\left(\frac{r_{ij}}{r_0^{\pi\pi}}\right)^{p_{bo,6}}\right] \end{aligned} \quad (\text{eq. 2-13})$$

The energy of each term in eq.2-12 is the function of the BO. For example, the first term  $E_{bond}$  is expressed as

$$E_{bond} = -D_e^{\sigma} BO_{ij}^{\sigma} \exp[p_{be,1}(1 - (BO_{ij}^{\sigma})^{p_{be,2}})] - D_e^{\pi} BO_{ij}^{\pi} - D_e^{\pi\pi} BO_{ij}^{\pi\pi} \quad (\text{eq. 2-14})$$

Figure 2.3 shows the results of the BO and  $E_{bond}$  with respect to the different Si-Si distance by Si-O ReaxFF published in 2003. It shows that the bond energy will gradually go to zero as the Si-Si distance grows larger, which is different from the harmonic oscillator approximation in tradition force fields. Since the atoms would be thoroughly separated if the distance of atoms are large enough, the behavior of bond breaking could be well described in ReaxFF.

In addition to the bond breaking behavior, ReaxFF is able to describe the charge state in each atom as well. In the ReaxFF implemented by LAMMPS, it used the charge equilibration scheme (Qeq) to calculate the charge for each atom.

### 2.3.2 Potential parameters optimization

Interatomic potential are important in classical modeling calculations; therefore, it is necessary to obtain the reliable parameters. Generally speaking, the parameters can be determined by fitting to data from higher quality calculations, such as first-principles calculations, or experiments. The fitting work is actually a numerical optimization

procedure aiming to minimize the error defined as follows:

$$Err = \sum_{all\ observables} w(f_{calc} - f_{obs})^2$$



(eq. 2-15)

where  $f_{calc}$  and  $f_{obs}$  are respectively the calculated value and target value of observables, and  $w$  is the weighting factors of the observable properties.

## 2.4 Molecular dynamics

Molecular dynamics (MD) was first introduced by Alder and Wainwright in the late 1950s. MD simulates the motions of atoms or molecules with a given potential function  $V$ , which describes the interactions between particles by classical force field or first principles calculations. The trajectories of particles can be calculated by solving the Newton's law of motion if the initial positions and velocities are given. The force acting on atoms can be expressed as the negative gradient of the potential energy.

$$F_i = -\nabla_i V$$

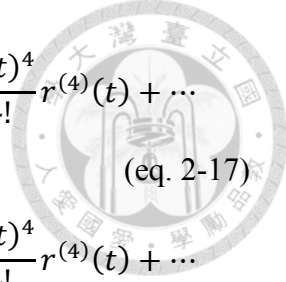
(eq. 2-16)

Once the force is known, the position and velocity of each atom can be obtained by numerical integration methods such as Verlet algorithm.

### 2.4.1 Verlet algorithm

The Verlet algorithm is used to integrate the motion of atoms when applying molecular dynamics simulations.<sup>[53]</sup> It is derived from Taylor expansion and central approximation. The positions of atoms at time= $t + \Delta t$  or  $t - \Delta t$  are represented by Taylor expansion:



$$r(t + \Delta t) = r(t) + \frac{\Delta t}{1!} r'(t) + \frac{(\Delta t)^2}{2!} r''(t) + \frac{(\Delta t)^3}{3!} r'''(t) + \frac{(\Delta t)^4}{4!} r^{(4)}(t) + \dots$$


(eq. 2-17)

$$r(t - \Delta t) = r(t) - \frac{\Delta t}{1!} r'(t) + \frac{(\Delta t)^2}{2!} r''(t) - \frac{(\Delta t)^3}{3!} r'''(t) + \frac{(\Delta t)^4}{4!} r^{(4)}(t) + \dots$$

(eq. 2-18)

The summation of the above two equations gives

$$r(t + \Delta t) = 2r(t) - r(t - \Delta t) + (\Delta t)^2 r''(t) + O(\Delta t^4)$$

(eq. 2-19)

where  $r''(t)$  is the acceleration of the system which can be derived from Newton's equation of motion.

$$r''(t) = a(t) = -\frac{1}{m} \nabla V$$

(eq. 2-20)

With a given potential function, the particles' positions and velocities at every given time can be calculated by the previous two steps.

## 2.4.2 Nosé-Hoover thermostat

There are some constraints should be adopted to MD simulations to keep the system stable. According to various constraints applied, there are some widely used ensembles, such as microcanonical ensemble (NVE), canonical ensemble (NVT), and isothermal-isobaric ensemble (NPT).

In canonical ensemble, the Nosé-Hoover thermostat is used to keep the temperature around an average <sup>[54], [55]</sup>. An imaging heat bath is simulated in Nosé-Hoover thermostat that has a recursive control of energy between the system and the artificial heat bath. An extra degree of freedom is added to the system in order to control the energy transfer.

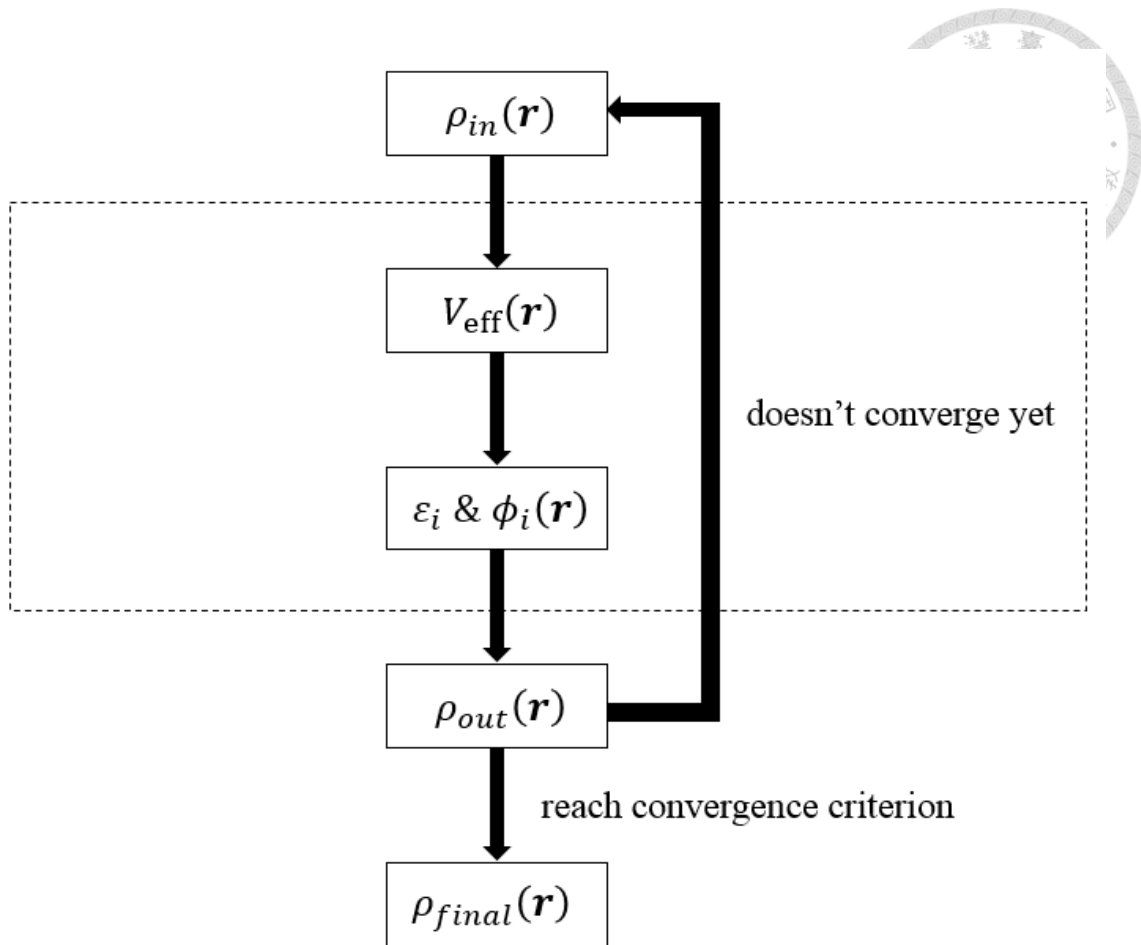


Figure 2.1 Flow chart of self-consistent field methods

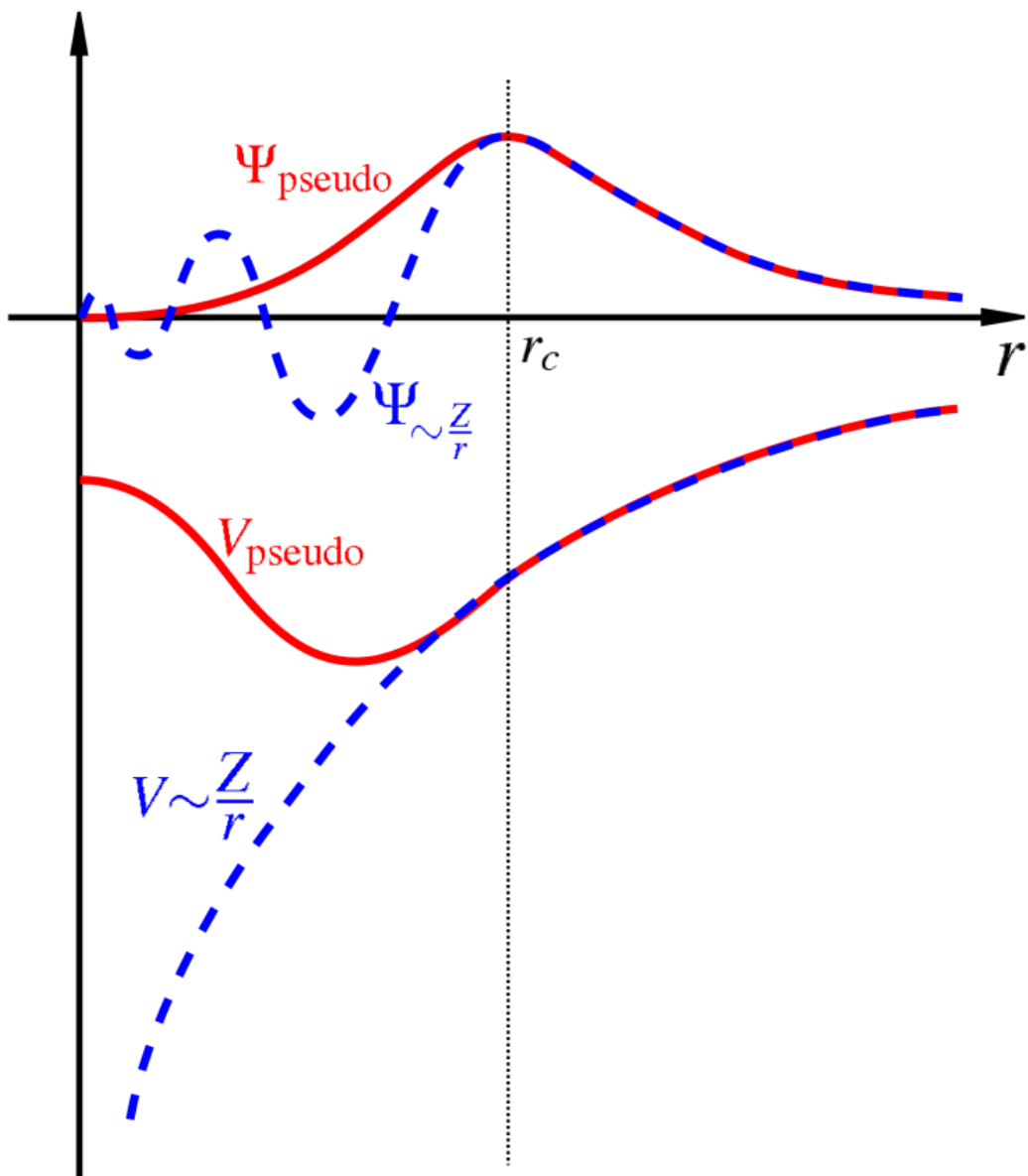
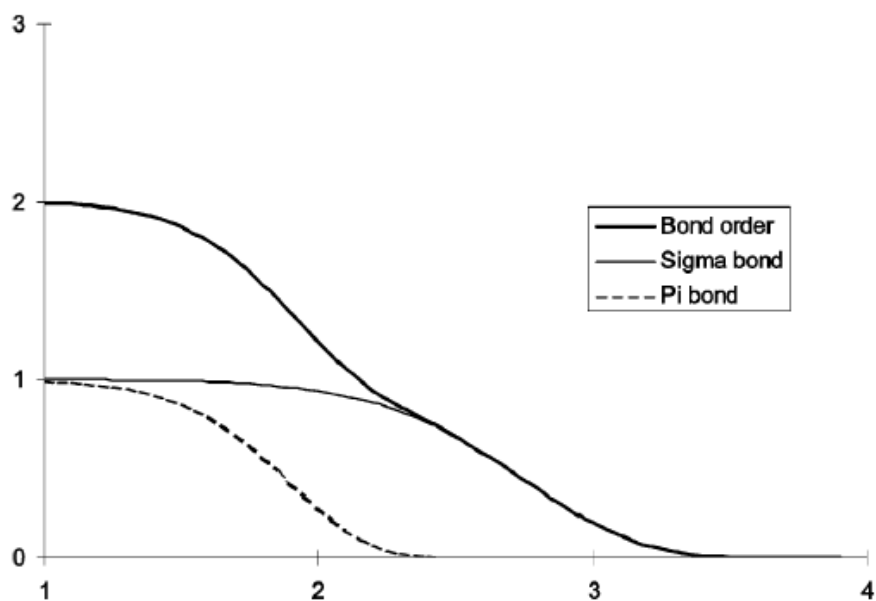
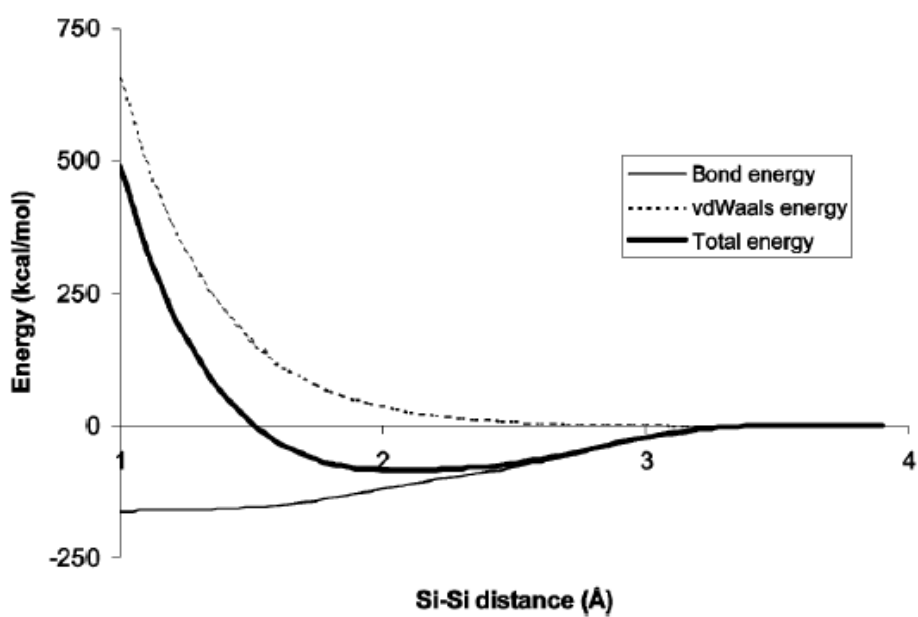


Figure 2.2 Schematic diagram of pseudopotential



The bond order function with respect to distance



The bond breaking energy–distance curve

Figure 2.3 The bond order function and the bond breaking behavior in ReaxFF <sup>[49]</sup>

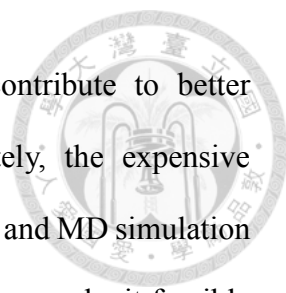
# Chapter 3 Development of Reactive Force Field Potential Model for Amorphous Silicon Oxycarbide



## 3.1 Introduction

As we mentioned in Chapter 1, it is relatively simple to introduce carbon and oxygen atoms into silicon-based anode materials by pyrolysis of polymers such as polysiloxane, polystyrene and divinylbenzene (DVB), as shown in Figure 3.1. The accessible polymer-to-ceramic process combined with the inexpensive raw materials make this kind of anode materials a competitive candidate for the next generation LIBs. There are lots of experimental research showed that amorphous SiOC was composed of three characteristic structures, free carbon, SiOC glasses ( $\text{SiO}_x\text{C}_{4-x}$  tetrahedra) and micropores (nano-voids). However, the morphology of the free carbon, its interface to the SiOC glass matrix, as well as the distribution of  $\text{SiO}_x\text{C}_{4-x}$  tetrahedra are hotly debated issues in concurrent research.

Based on the experimental results, Sorarù et al.<sup>[56]</sup> and Saha et al.<sup>[57]</sup> respectively proposed a probable nanostructure as shown in Figure 3.2 and Figure 3.3. From the model of Sorarù et al., a free carbon phase consisting mainly of graphene-like six-membered rings with several edge defects can be observed. Furthermore, the Si-O and Si-C mixed bonds compose a SiOC glass region full of  $\text{SiO}_x\text{C}_{4-x}$  tetrahedra next to the free carbon phase. Between the two phases are several Si-C bonds formed. From the model of Saha et al., equivalently, the free carbon phase and SiOC glass phase could be observed. Nevertheless, they considered that carbon atoms would only segregate near the free carbon phase instead of being found in SiOC glass phase.



In terms of Atomistic modeling, DFT calculations might contribute to better understanding of local structures in SiOC materials. Unfortunately, the expensive computational cost of it limits the model sizes to a few hundred atoms and MD simulation times to below 1 ns. On the other hand, empirical potential simulations make it feasible to explore the mechanical properties of SiOC in models with millions of atoms extending several nanometers. However, the lack of chemical bonding accuracy, proper atomic environments, and acceptable thermochemistry are found inevitable.

The Reactive force field (ReaxFF) <sup>[49]</sup> bridges the gap between DFT calculations and empirical potential simulations. It achieves a level of accuracy approaching DFT simulations for a wide set of molecular reactions in the gas phase and on surfaces. Simultaneously, it is several orders of magnitude less computationally expensive, allowing modeling in larger systems for longer simulation time as compared to DFT simulations.

Based on the ReaxFF parameter set for modeling the oxidation of silicon carbide developed by Newsome et al. <sup>[58]</sup>, Ponomarev et al. <sup>[59]</sup> further optimized the force field parameters for Si/C/O/H. Then they applied the modified parameter set called UTA1 to construct amorphous SiOC through melt-and-quench MD and finally got the nanostructure shown in Figure 3.4 (b). Compared with the structure constructed via DFT shown in Figure 3.4 (a), we can see that both models comprise a layer of SiCO glass sandwiched between buckled graphene layers of free carbon phase. However, there is barely carbon atoms that can be found in SiOC glass phase in the structure constructed by ReaxFF. While there are a few carbon atoms in SiOC glass phase in the one constructed by DFT. Additionally, in the structure constructed by ReaxFF, a two-coordinated carbon chain, which seems not to be a reasonable structure, can be discovered in the interface between free carbon and SiOC glass. Finally, Ponomarev et al. stated that one of the imperfections of UTA1 parameters is the too-high tolerance for three-coordinated silicon

and oxygen species.

In this chapter, we aimed to modify the ReaxFF parameter set for Si/O/C from the UTA1 parameters. The modification of both unary and binary systems are involved. This version of Si/O/C ReaxFF potential model not only can still be adopted in the construction of SiOC structures with obvious phase separation of free carbon and SiOC glass phase, but also lower the fraction of atoms with coordination defect in amorphous SiOC systems. Owing to the adjustments of parameters, finally, the parameters fitted in this work are able to build amorphous SiOC structures that are thermodynamically more stable than the structures built by UTA1 parameters.



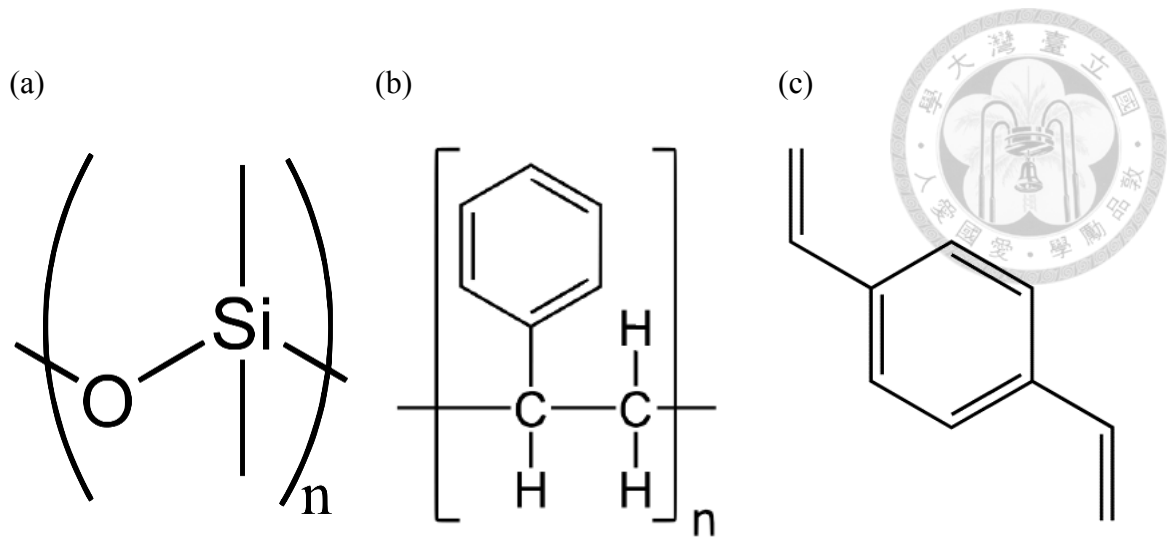


Figure 3.1 Precursors of polymer-derived amorphous SiOC: (a) polysiloxane, (b) polystyrene, (c) divinylbenzene

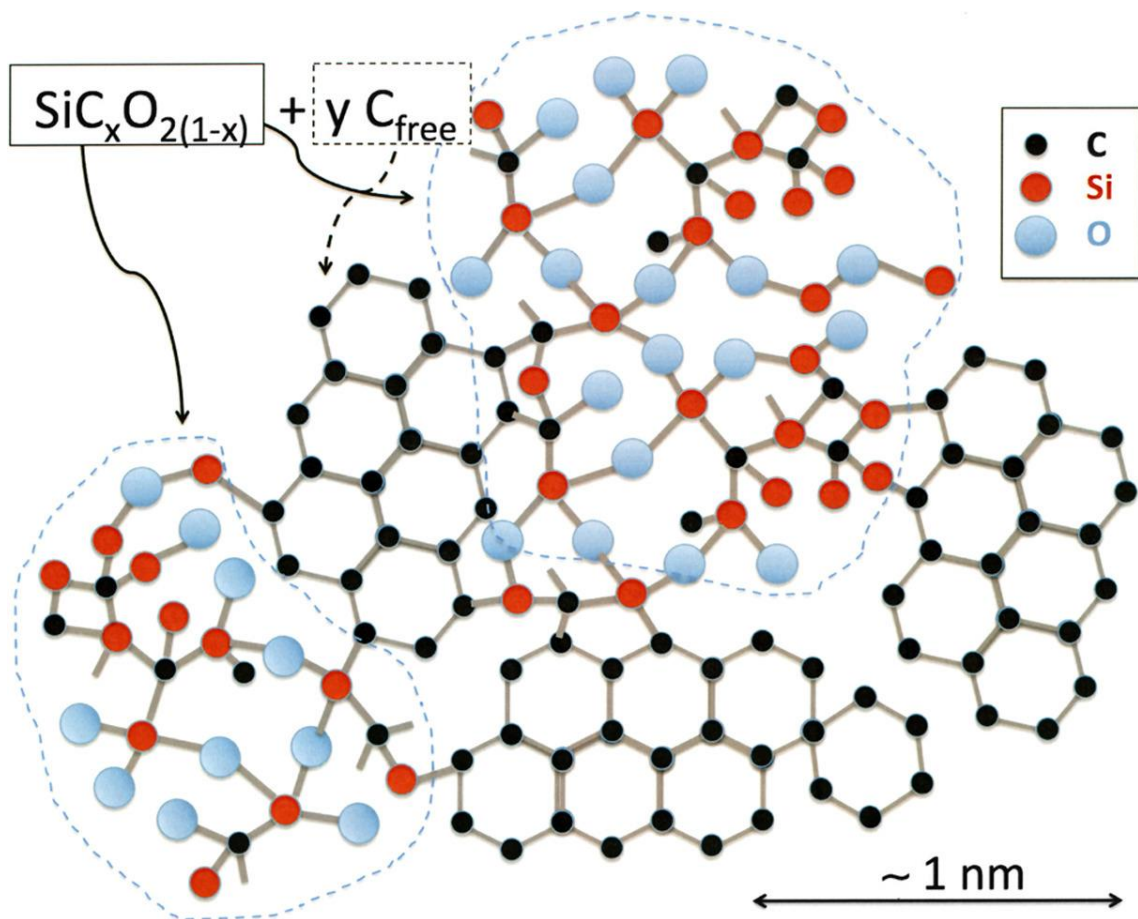


Figure 3.2 Schematic representation of SiOC proposed by Sorarù et al. <sup>[56]</sup>



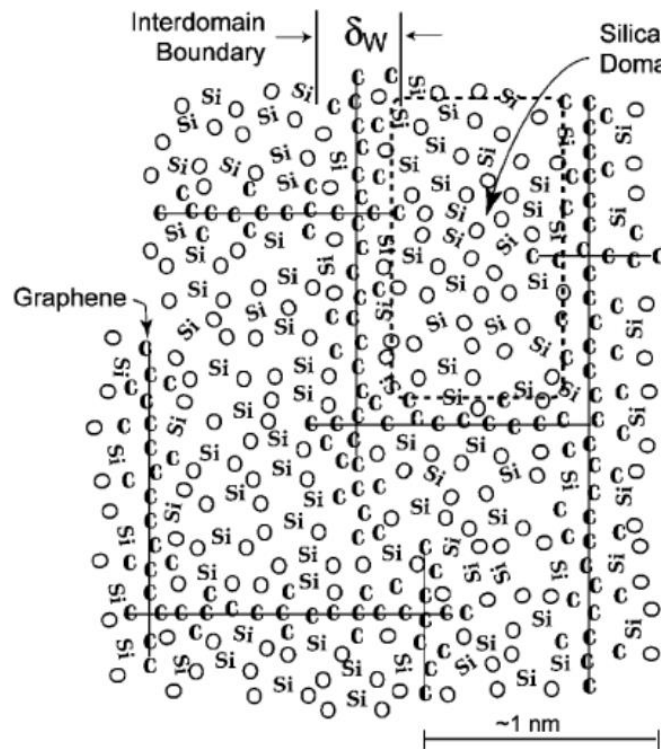


Figure 3.3 Schematic representation of SiOC proposed by Saha et al. [57]

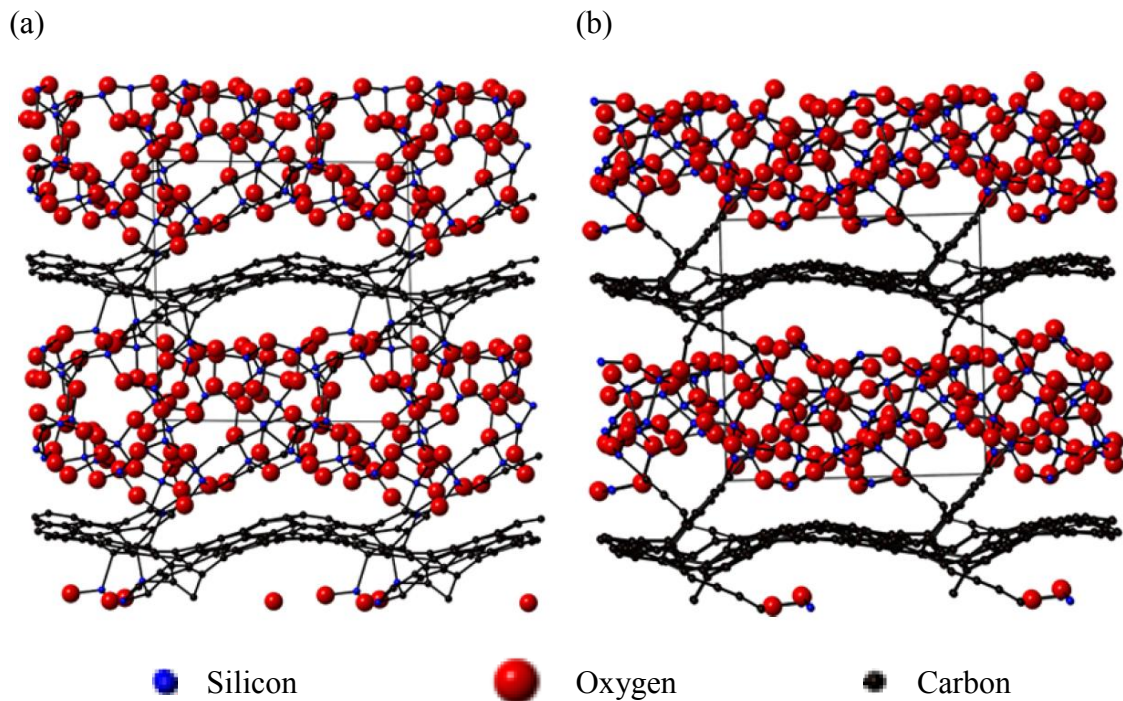


Figure 3.4 Amorphous models of  $\text{SiC}_{2.2}\text{O}_{1.6}$  (192 atoms) generated via melt-and-quench MD simulation with a cooling rate of  $1.25 \times 10^{13}$  K/s starting from 5000 K: (a) DFT, (b)

ReaxFF using UTA1 parameters. [59]



## 3.2 Methodology

### 3.2.1 ReaxFF parametrization

The parameters of the ReaxFF in this work are fitted with general utility lattice program (GULP)<sup>[60], [61]</sup> version 4.0. It is designed to perform a variety of tasks based on force field methods, such as facilitating the fitting of interatomic potentials to both energy surfaces and empirical data. With the aid of GULP, the properties of certain structures can be fitted.

For both unary and binary systems the lattice constants, cohesive energy, elastic constants and some relative relationships among elastic constants like Zener ratio<sup>[62]</sup> calculated from DFT are served as validation data.

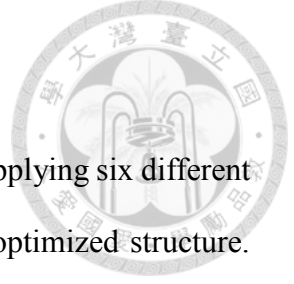
Here, the cohesive energy was defined as the following equation,

$$E_{cohesive} = E_{system} - \sum_i n_i \cdot E_{isolated,i} \quad (\text{eq. 3-1})$$

where  $E_{system}$  is the total energy of the system while  $n_i$  and  $E_{isolated,i}$  correspond to the number of  $i$  atom in the system and the energy of an isolated  $i$  atom, respectively. The Zener ratio is a dimensionless number that is used to quantify the anisotropy for cubic crystals. Its mathematical definition is expressed as

$$\frac{2C_{44}}{(C_{11} - C_{12})} \quad (\text{eq. 3-2})$$

Conceptually, it quantifies how far a material is from being isotropic, and the value of one means an isotropic material.



### 3.2.2 Mechanical properties calculation

The mechanical properties of the systems can be calculated by applying six different strains, including 3 normal strains and 3 shear strains, on an fully optimized structure. The corresponding 6×6 elastic tensor, in which there are 21 independent elements, can then be calculated by the following equation:

$$\begin{pmatrix} \sigma_{xx} \\ \sigma_{yy} \\ \sigma_{zz} \\ \sigma_{yz} \\ \sigma_{zx} \\ \sigma_{xy} \end{pmatrix} = \begin{pmatrix} c_{11} & c_{12} & c_{13} & c_{14} & c_{15} & c_{16} \\ c_{21} & c_{22} & c_{23} & c_{24} & c_{25} & c_{26} \\ c_{31} & c_{32} & c_{33} & c_{34} & c_{35} & c_{36} \\ c_{41} & c_{42} & c_{43} & c_{44} & c_{45} & c_{46} \\ c_{51} & c_{52} & c_{53} & c_{54} & c_{55} & c_{56} \\ c_{61} & c_{62} & c_{63} & c_{64} & c_{65} & c_{66} \end{pmatrix} \begin{pmatrix} \varepsilon_{xx} \\ \varepsilon_{yy} \\ \varepsilon_{zz} \\ \varepsilon_{yz} \\ \varepsilon_{zx} \\ \varepsilon_{xy} \end{pmatrix} \quad (\text{eq. 3-3})$$

Usually, the number of independent elements can be reduced according to the symmetry of the structure. In a cubic system, for example, the required elements can be reduced to  $c_{11}$ ,  $c_{12}$  and  $c_{44}$  only.

### 3.2.3 Melt-and-quench procedures to construct amorphous silicon oxycarbide

The structures of SiOC were constructed by melt-and-quench method simulated via ReaxFF MD simulations performed with the large-scale atomic/molecular massively parallel simulator (LAMMPS) software<sup>[51]</sup>. In this MD simulation, we used a time step of 0.2 fs for the integration of the equations of motion. We considered four SiOC concentrations: SiC<sub>2.2</sub>O<sub>1.6</sub>, SiC<sub>1.65</sub>O<sub>1.6</sub>, SiC<sub>0.8</sub>O<sub>1.6</sub> and SiC<sub>1.65</sub>O<sub>0.6</sub>. For each concentration, we set the total amount of atom up to around 200 in the systems to ensure the structural characteristics could be observed. The exact atomistic compositions of the systems are shown in Table 3.1.

According to the atomistic compositions of each concentration, three initial

structures were constructed by randomly arranging the atoms in the simulation box with density of  $2.2 \text{ g/cm}^3$ . The temperature procedure of melt-and-quench is displayed in Figure 3.5. The systems were first annealed at 5000K for 20ps until equilibrium. Then they were quenched to 4000K with a quench rate of  $10^{14} \text{ K/s}$ . Next, during 4000K to 1000K, which is close to the melting point of SiOC glasses, the quench rate was adjusted to  $10^{13} \text{ K/s}$  to let the systems have enough time to reach the most stable structure. Besides, the volume of the systems was adjusted every 1000K to release the stress formed during the quench process, followed by a 10ps of annealing at the corresponding temperature. After the volume adjustment at 1000K was done, the systems were quenched to 300K with a quench rate of  $10^{14} \text{ K/s}$ . When the systems were quenched to the room temperature, structural optimization calculations were performed to release the internal stress. Finally, after a 30ps of annealing at 1800K and structural optimization calculations, the three amorphous SiOC samples of each concentration were obtained. All the MD process were performed in canonical ensemble (NVT ensemble), and the flow chart is shown in Figure 3.6.

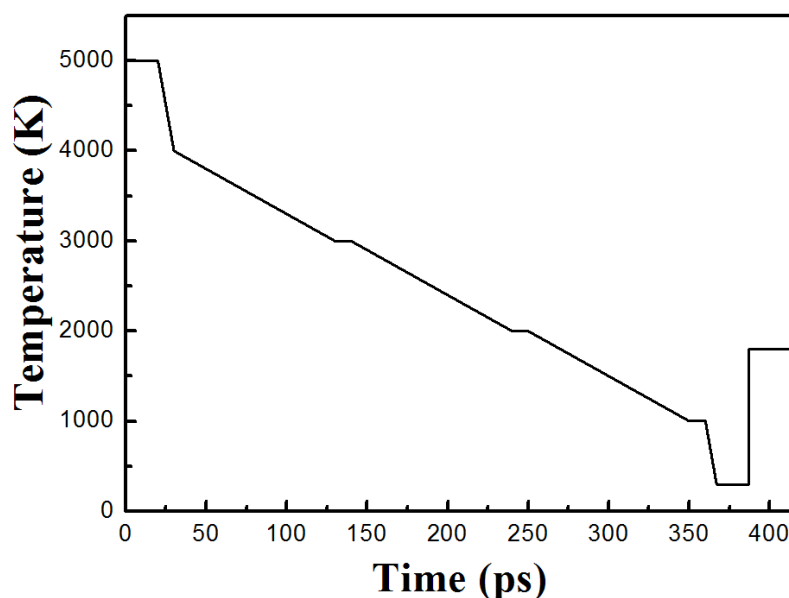


Figure 3.5 Melt-and-quench procedure of amorphous SiOC construction

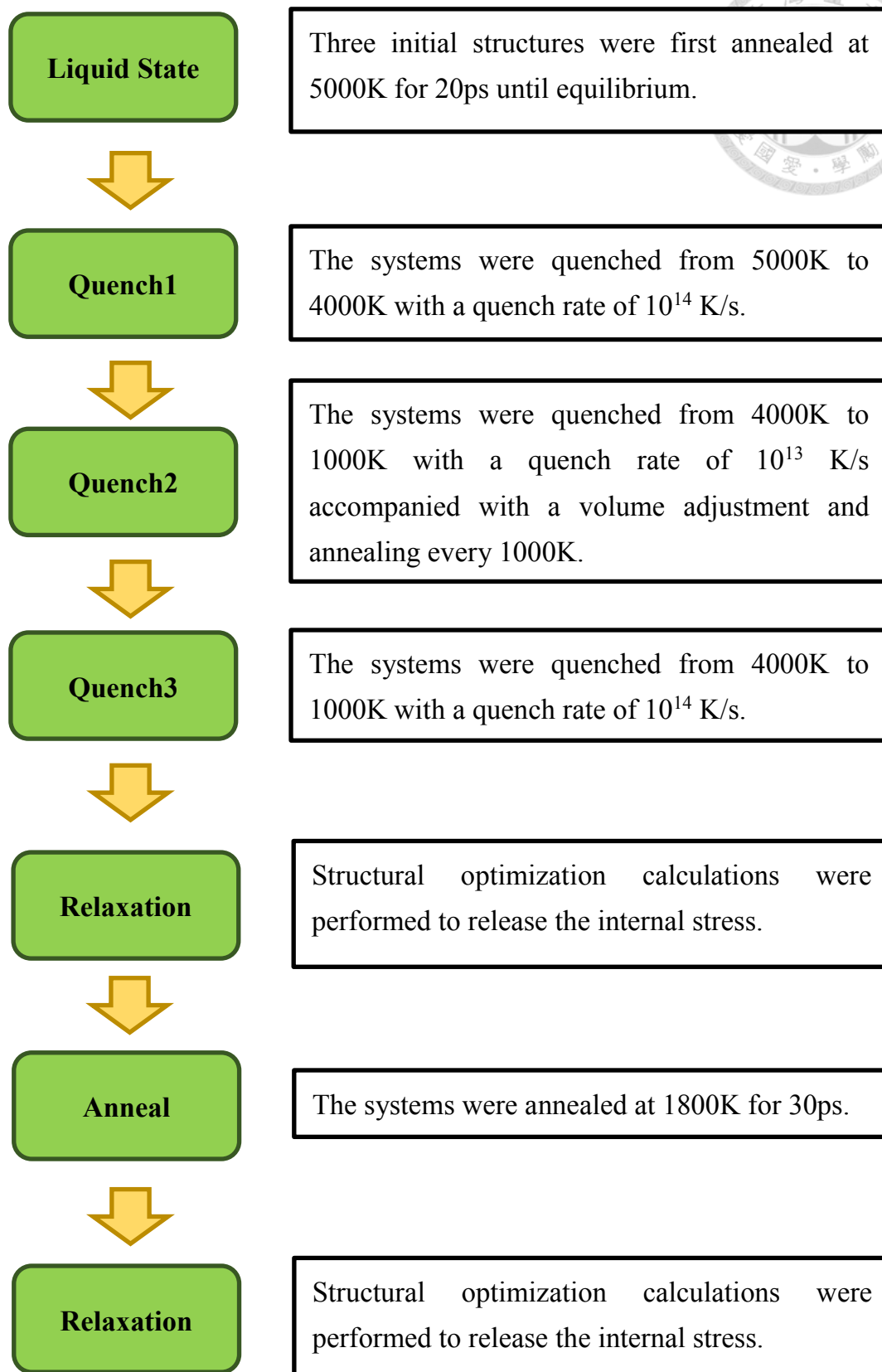


Figure 3.6 Flow chart of amorphous SiOC construction

Table 3.1 Atomistic compositions of SiOC samples

	Si	O	C	Total
SiC <sub>2.2</sub> O <sub>1.6</sub>	40	64	88	192
SiC <sub>1.65</sub> O <sub>1.6</sub>	46	74	76	196
SiC <sub>0.8</sub> O <sub>1.6</sub>	58	93	46	197
SiC <sub>1.65</sub> O <sub>0.6</sub>	60	36	99	195

### 3.2.4 Computational details

DFT calculations implemented by VASP are taken as part of our validation data. The GGA-PBE are used for the electron exchange-correlation functional. The valence electron wave functions are expanded by plane-wave basis sets and the core-electron interactions are described by the projector augmented wave (PAW) method. The plane-wave cut-off energy is set to be 500 eV. The Brillouin zone samplings are performed with Monkhorst-Pack scheme, in which  $2 \times 2 \times 2$  k-point grid sampling is used. In the mechanical properties calculations, all atoms are relaxed until the residual forces on the constituent atoms are smaller than  $0.001 \text{ eV/\AA}$ , while in other calculations,  $0.05 \text{ eV/\AA}$  are set as the stopping criteria.



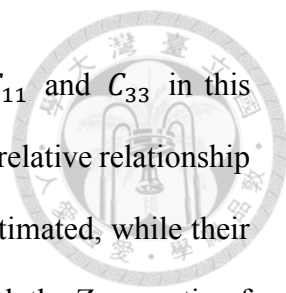
### 3.3 Results and discussion

#### 3.3.1 Validation of ReaxFF parameters

In amorphous SiOC systems, the main characteristic structures of free carbon, SiOC glasses and micropores are widely published. To construct reasonable and reliable structures of SiOCs, it is vital for a potential model to describe the interactions among Si, O and C atoms precisely, especially for the interactions between C-C, Si-C and Si-O, which are the major interactions observed in amorphous SiOCs. Thus in this section, we focus on the validation of unary and binary systems, which are diamond, graphite and SiO<sub>2</sub> ( $\alpha$ -quartz), SiC ( $\beta$ -SiC) respectively.

The “parameter file”, which is the ReaxFF potential file read by LAMMPS, of this model is attached in **Appendix**. First, validations of structural properties and energetics of diamond and graphite are listed in Table 3.2, including lattice constant and cohesive energy. The results of structural properties show that after the modification, the modified ReaxFF model has good agreement with the DFT calculations. As we can see in Table 3.2, the properties calculated by our ReaxFF model have better agreements to DFT calculations than UTA1 model, including lattice constant and, particularly, cohesive energy.

The comparison of mechanical properties of diamond and graphite between this work and UTA1 parameters is listed in Table 3.3. In diamond system, for UTA1 parameters,  $C_{12}$  is over four times greater than the value of DFT, while  $C_{44}$  is only around half of the value of DFT. After modifications,  $C_{12}$  and  $C_{44}$  of this work are much closer to the values from DFT calculations, with a little sacrifice on the accuracy in  $C_{11}$ . In graphite system, for UTA1 parameters,  $C_{11}$ ,  $C_{12}$  and  $C_{33}$  are overestimated when comparing to DFT calculations, while  $C_{66}$  is, on the contrary, underestimated. In terms of the results of this work, though there are still some deviations,  $C_{12}$  and  $C_{66}$  are



in better agreement with DFT calculations. However, the bias of  $C_{11}$  and  $C_{33}$  in this work become slightly larger than that in UTA1 model. In terms of the relative relationship among elastic constants, the Zener ratio of UTA1 is slightly underestimated, while their  $(C_{11} - C_{12})/2$  are severely underestimated. On the other hand, though the Zener ratio of this work is slightly overestimated, the prediction of  $(C_{11} - C_{12})/2$  are better than that calculated by UTA1 parameters.

The energy volume curves of diamond and graphite are shown in Figure 3.7 and Figure 3.8 respectively. Thanks to the improvements above, the adjustments of cohesive energy and elastic constants make not only the energies, but also the curvatures of the energy volume curves of both diamond and graphite in this work closer to those in DFT calculations.

For binary systems, validations of structural properties and energetics of  $\text{SiO}_2$  and  $\text{SiC}$  are listed in Table 3.4. The results show that our ReaxFF model has better agreement to DFT calculations in cohesive energy than UTA1. Nonetheless, the performances on lattice constants are not as good as cohesive energies.

The results of mechanical properties are presented in Table 3.5. For  $\text{SiO}_2$ , the slightly overestimated elastic constants in UTA1 were improved in this work. For  $\text{SiC}$ , the elastic constants calculated by UTA1 are seriously deviated.  $C_{11}$  and  $C_{12}$  are both extremely overestimated, while  $C_{44}$  is even negative in UTA1 model. After the modifications,  $C_{11}$ ,  $C_{12}$  and  $C_{44}$  are substantially corrected and get much closer to DFT calculations. Besides, the Zener ratio and  $(C_{11} - C_{12})/2$  calculated by the parameters fitted in this work are improved as well.



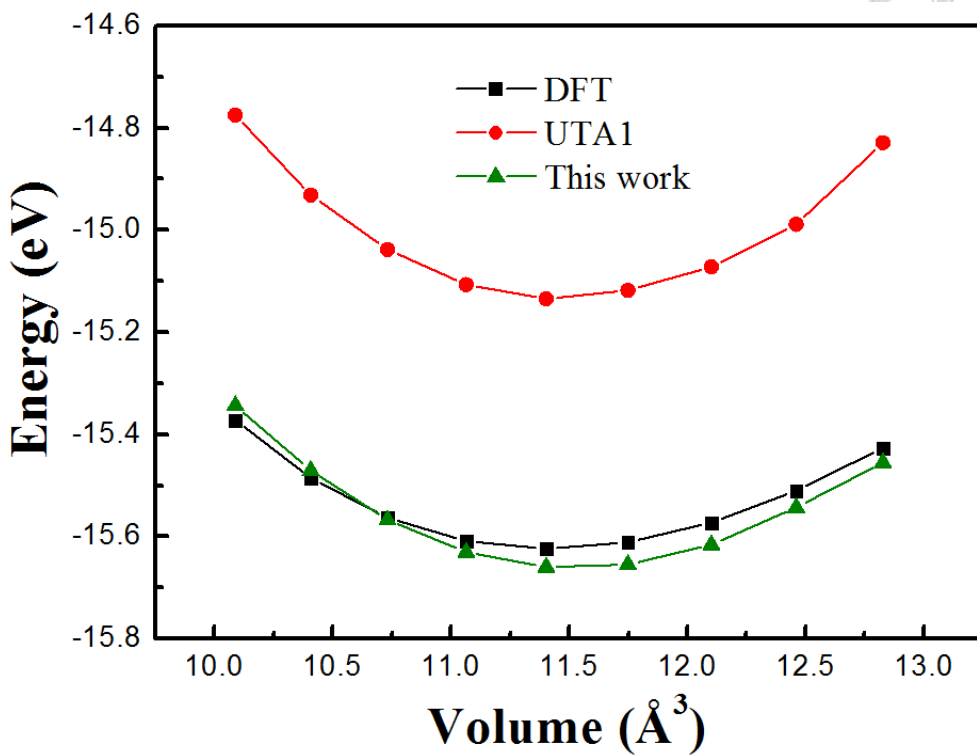


Figure 3.7 The energy volume curve of diamond

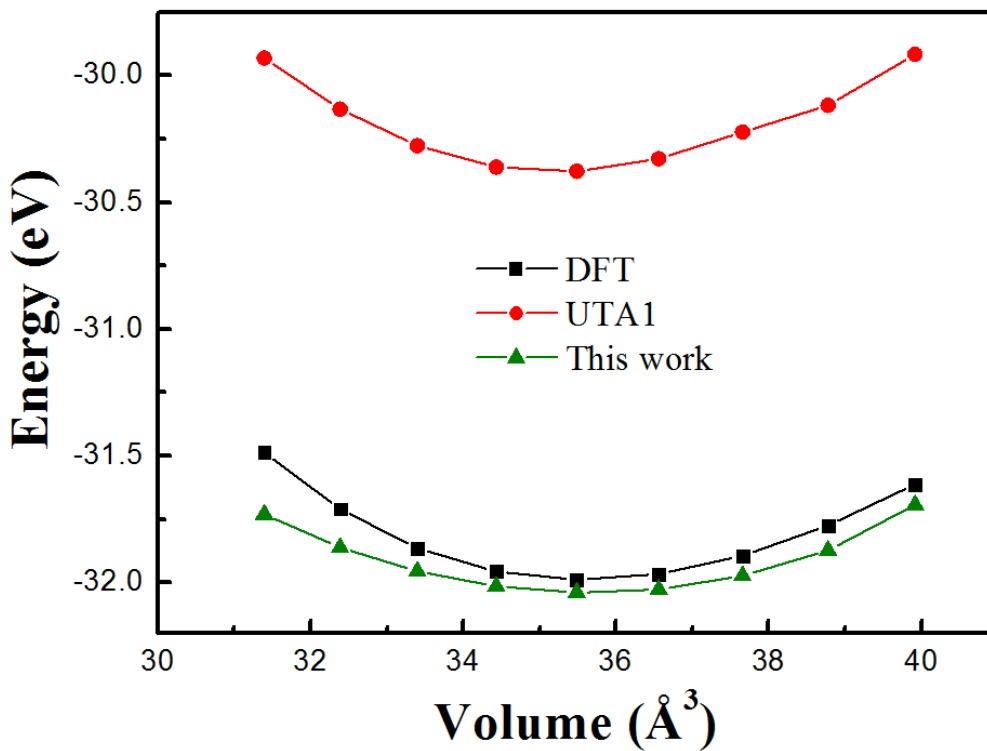


Figure 3.8 The energy volume curve of graphite

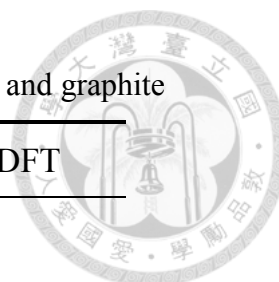


Table 3.2 Validation of structural properties at 0 K of diamond and graphite

	This work	UTA1	DFT
<b>Diamond</b>			
$E_{\text{cohesive}}$ (eV/atom)	-7.81	-7.57	-7.81
lattice constant (Å)	3.58	3.58	3.57
<b>Graphite</b>			
$E_{\text{cohesive}}$ (eV/atom)	-7.97	-7.59	-8.02
a (Å)	2.47	2.45	2.47
d-spacing (Å)	3.44	3.26	3.37

Table 3.3 Validation of mechanical properties of diamond and graphite

	This work	UTA1	DFT
<b>Diamond</b>			
$C_{11}$ (GPa)	881	989	1047
$C_{12}$ (GPa)	207	539	124
$C_{44}$ (GPa)	421	260	559
$(C_{11} - C_{12})/2$	337	225	462
$\frac{2C_{44}}{(C_{11} - C_{12})}$	1.25	1.16	1.21
<b>Graphite</b>			
$C_{11}$ (GPa)	851	1114	1048
$C_{12}$ (GPa)	60	590	188
$C_{33}$ (GPa)	16	38	29
$C_{66}$ (GPa)	396	262	430
$(C_{11} - C_{12})/2$	396	262	430

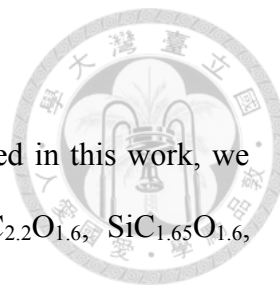


Table 3.4 Validation of structural properties at 0 K of SiO<sub>2</sub> and SiC

	This work	UTA1	DFT
<b>SiO<sub>2</sub> (<math>\alpha</math>-quartz)</b>			
E <sub>cohesive</sub> (eV/atom)	-19.74	-18.82	-19.74
a (Å)	4.98	5.08	5.02
c (Å)	5.42	5.58	5.51
<b>SiC (<math>\beta</math>-SiC)</b>			
E <sub>cohesive</sub> (eV/atom)	-12.93	-12.87	-12.93
lattice constant (Å)	4.43	4.36	4.38

Table 3.5 Validation of mechanical properties of SiO<sub>2</sub> and SiC

	This work	UTA1	DFT
<b>SiO<sub>2</sub> (<math>\alpha</math>-quartz)</b>			
C <sub>11</sub> (GPa)	87	126	79
C <sub>13</sub> (GPa)	8	46	7
C <sub>33</sub> (GPa)	74	109	88
C <sub>44</sub> (GPa)	56	50	52
C <sub>66</sub> (GPa)	43	46	42
<b>SiC (<math>\beta</math>-SiC)</b>			
C <sub>11</sub> (GPa)	401	1139	383
C <sub>12</sub> (GPa)	120	1119	126
C <sub>44</sub> (GPa)	209	-17.81	241
(C <sub>11</sub> - C <sub>12</sub> )/2	141	10	129
$\frac{2C_{44}}{(C_{11} - C_{12})}$	1.48	-1.78	1.87

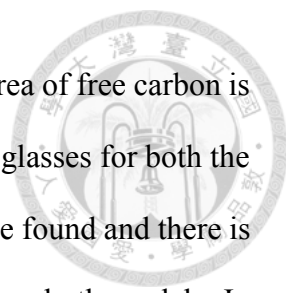


### 3.3.2 Structures of amorphous SiOC

Using both the parameter set of UTA1 and the parameters fitted in this work, we designed four different concentrations of SiOCs, which are  $\text{SiC}_{2.2}\text{O}_{1.6}$ ,  $\text{SiC}_{1.65}\text{O}_{1.6}$ ,  $\text{SiC}_{0.8}\text{O}_{1.6}$  and  $\text{SiC}_{1.65}\text{O}_{0.6}$ . For each concentration, three distinct structures were constructed by the two parameters respectively. The structures built via the parameters fitted in this work and UTA1 in different concentrations are shown in Figure 3.9 to Figure 3.16. Note that only the structures with the most stable configuration, or to say the lowest formation energy, are shown. Yet the coordination numbers of the atoms in SiOCs in certain concentration is calculated by the average of all three structures of each concentration.

First, for  $\text{SiC}_{2.2}\text{O}_{1.6}$  shown in Figure 3.9 and Figure 3.10, both the structures constructed by our model and UTA1 parameters showed a clear phase separation between free carbon and SiOC glass phase. However, in the structure from UTA1 parameters, there is no carbon atom in the SiOC glass region. Instead, almost all the carbon atoms compose a piece of curly graphene-like free carbon. Moreover, a two-coordinated carbon chain, which seems not to be a reasonable structure, can be discovered between the SiOC glass and free carbon. On the other hand, in the structure constructed from our parameter set, the free carbon looked flatter than that in UTA1 structure. Besides, a piece of graphene-like carbon was found in the SiOC glass region.

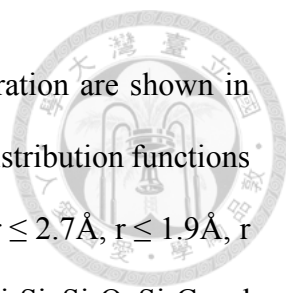
Second, for  $\text{SiC}_{1.65}\text{O}_{1.6}$  shown in Figure 3.11 and Figure 3.12, through the slightly decrease of carbon concentration, the free carbon in both structures became flatter though the free carbon in structure from UTA1 parameters still seemed curlier than that from our parameters. In terms of SiOC glass phase, a few carbon atoms can be discovered in SiOC glass region, while the SiOC glass in the structure from UTA1 parameters consisted of only Si and O atoms.



Then, for  $\text{SiC}_{0.8}\text{O}_{1.6}$  shown in Figure 3.13 and Figure 3.14, the area of free carbon is decreased obviously and thus the free carbon is surrounded by SiOC glasses for both the structures. At the edge of free carbon phase, several Si-C bonds can be found and there is no carbon atom appearing in SiOC glass region of the structures from both models. In this concentration, there are little differences between the structure built from UTA1 parameters and the one built from our parameter set.

Finally, for  $\text{SiC}_{1.65}\text{O}_{0.6}$  shown in Figure 3.15 and Figure 3.16, the phase separation between free carbon and SiOC glass is clear as well. In both of the structures, different from the former concentrations, there are several carbon atoms in the SiOC glass region. However, the amount of carbon atoms in SiOC glass for our model is greater than that for UTA1. For free carbon phase, like the previous concentrations, the free carbon layer in the structure from our parameters were flatter than that from UTA1 parameters.

Overall, the carbon atoms in the structures constructed via the parameters fitted in this work are more likely to have the tendency to be discovered in SiOC glass phase than that in the structures constructed via UTA1 parameters. The reason for this phenomenon is attributed to the adjustment of elastic constants of SiC. The overestimated elastic constants of SiC by UTA1 parameters cause the extremely low tolerance of deformation in Si-C bond, which means the energy of the systems would rise rapidly with the distortion, compression or stretching of Si-C bonds. However, it is inevitable for SiOC glass phase to have deformed Si-C bonds because of the differences in local packing environment between  $\text{SiO}_2$  (Si-O bonds) and SiC (Si-C bonds). Therefore, after the modification of parameters, the improved elastic constants make carbon atoms in our model are prone to be located in SiOC glass phase. In structures from UTA1 parameters, the carbon atoms that cannot be stabilized in SiOC glass region tend to join the free carbon phase, leading to the curlier free carbon layers.

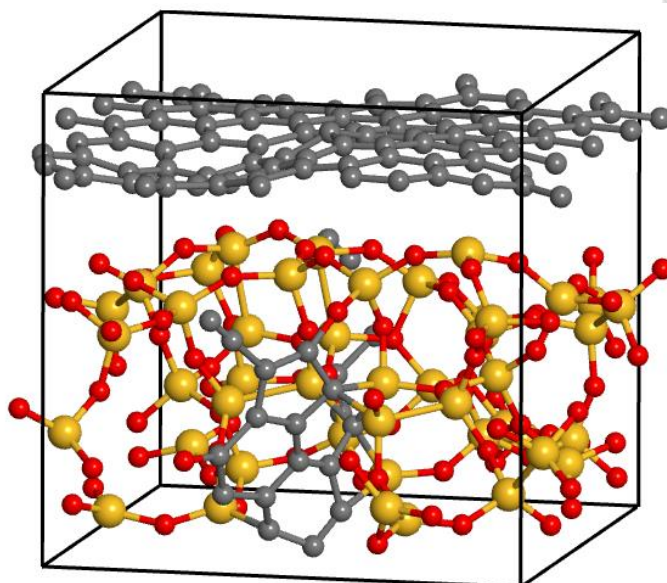


Next, the coordination number (CN) analyses of each concentration are shown in Figure 3.17 to Figure 3.20. Considering the first valley of the radial distribution functions of a-Si, a-SiO<sub>2</sub>, a-SiC and a-C of 2.7, 1.9, 2.2 and 2.0, respectively,  $r \leq 2.7\text{\AA}$ ,  $r \leq 1.9\text{\AA}$ ,  $r \leq 2.2\text{\AA}$  and  $r \leq 2.0\text{\AA}$  are chosen as the representative cutoff radii for Si-Si, Si-O, Si-C and C-C bonds. First of all, for SiC<sub>2.2</sub>O<sub>1.6</sub>, the results shown in Figure 3.17 illustrates that the numbers of three- and five-coordinated silicon atoms and three-coordinated oxygen atoms in the structure constructed by our parameters decrease compared to the structure constructed by UTA1 parameters. Secondly, for SiC<sub>1.65</sub>O<sub>1.6</sub>, the results are shown in Figure 3.18. As we can see, the five-coordinated silicon atoms were vanished after the modification of parameters. On the other hand, there are several two- and four-coordinated carbon atoms found in the structures built via our parameters on account of the carbon atoms in SiOC glass phase. Third, for SiC<sub>0.8</sub>O<sub>1.6</sub>, the results are shown in Figure 3.19. The numbers of five-coordinated silicon atoms and two-coordinated carbon atoms in the structures are reduced while the coordination distribution of oxygen atoms were quite the same after the modification of parameters. Besides, there are no four-coordinated carbon atom in structure from UTA1 parameters at all, indicating that under the description of UTA1 parameters, C atoms can hardly be the form of sp<sup>3</sup> hybridization. Lastly, for SiC<sub>1.65</sub>O<sub>0.6</sub>, as we can see in Figure 3.20, there are a few two- and even six-coordinated silicon atoms appearing in the structures constructed by UTA1 parameters, while there isn't any in the structures constructed by the parameters fitted in this work. Besides, the number of five-coordinated silicon atoms in our structures are less than that in UTA1's structures.

In summary, the too-high tolerance of UTA1 parameters for under- and over-coordinated silicon atoms and three-coordinated oxygen atoms were improved thanks to the more precise elastic constants and cohesive energies prediction of SiO<sub>2</sub> and SiC after the modifications of parameters.



(a)



(b)

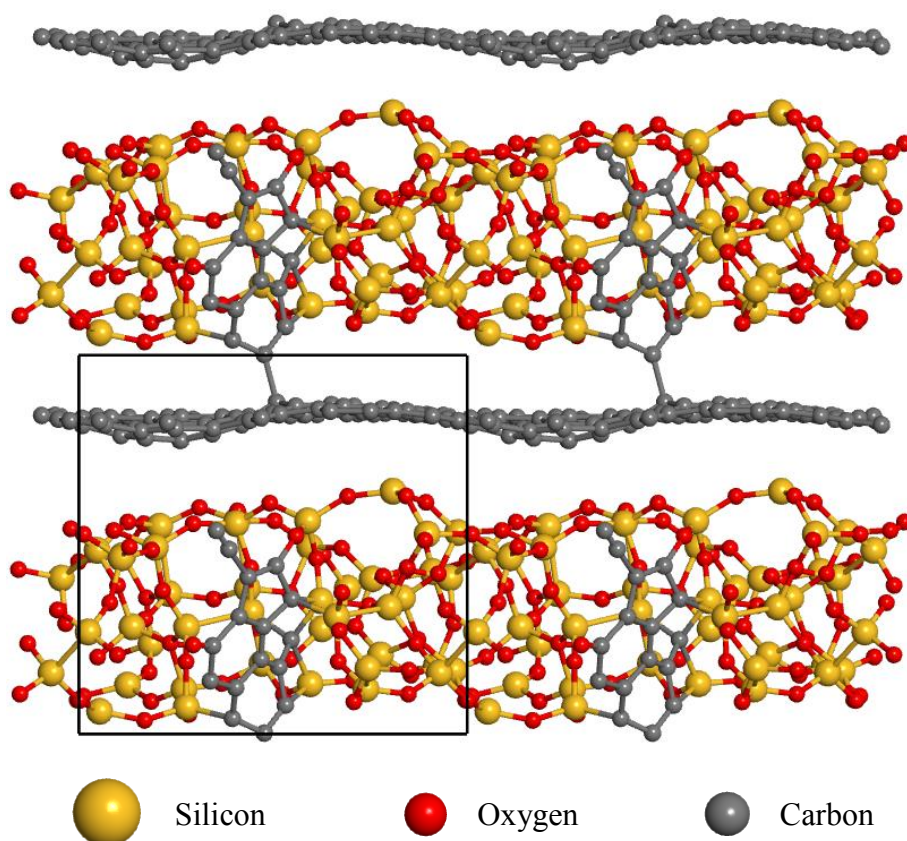
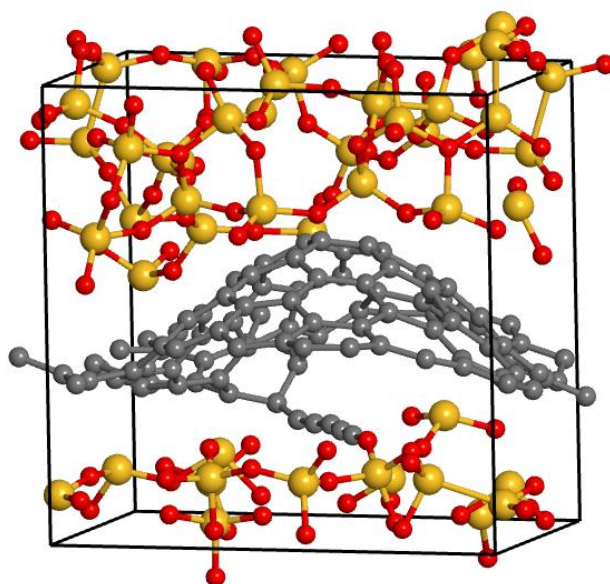


Figure 3.9 The structure of  $\text{SiC}_{2.2}\text{O}_{1.6}$  constructed by the parameters developed in this work: (a) unit cell, (b) overview of the  $2 \times 2$  supercell



(a)



(b)

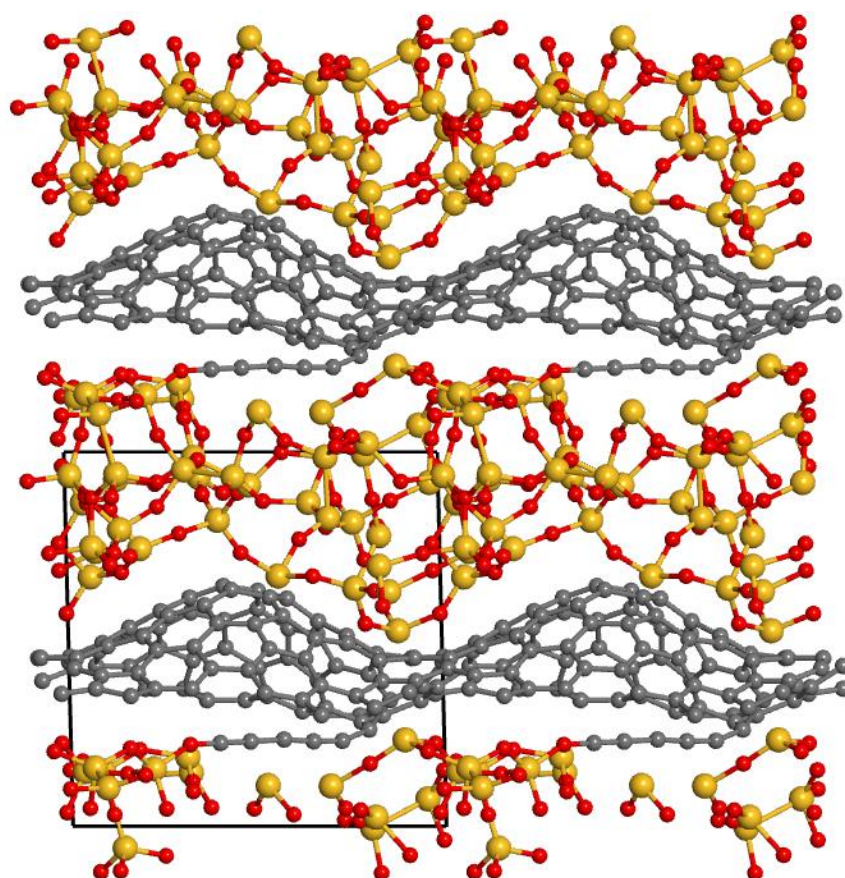
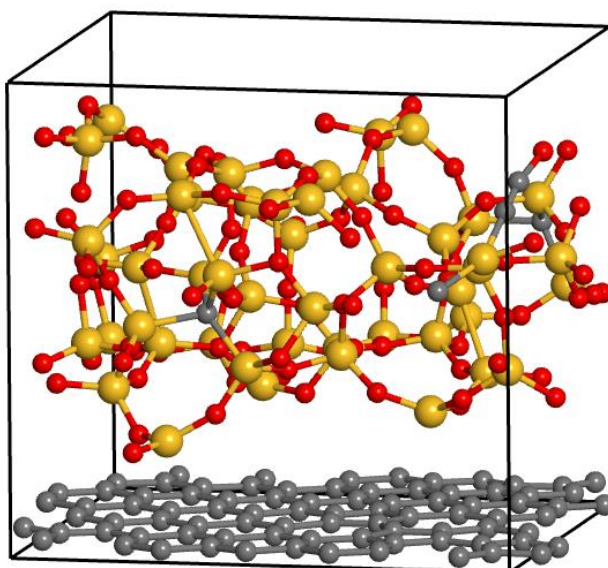


Figure 3.10 The structure of  $\text{SiC}_{2.2}\text{O}_{1.6}$  constructed by UTA1: (a) unit cell, (b) overview of the  $2 \times 2$  supercell





(a)



(b)

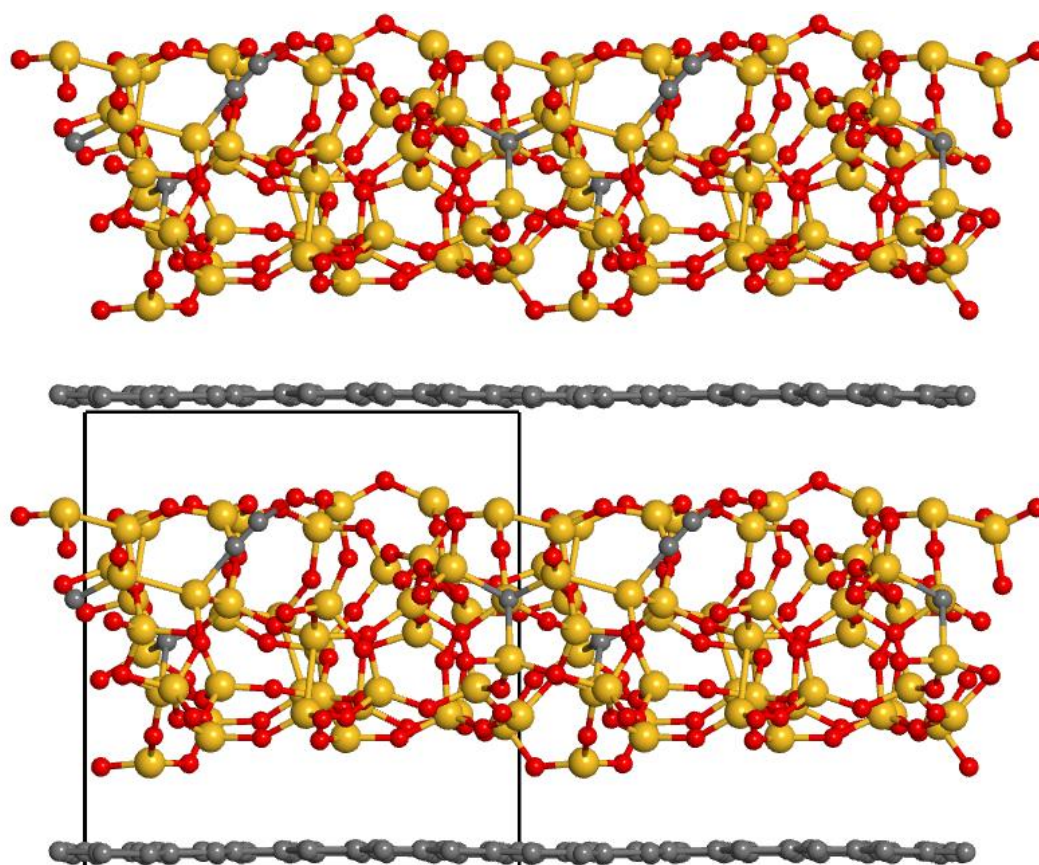
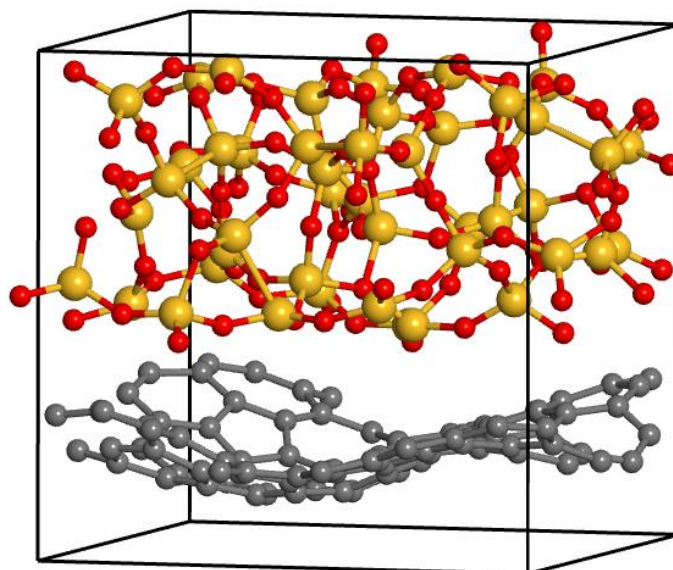


Figure 3.11 The structure of  $\text{SiC}_{1.65}\text{O}_{1.6}$  constructed by the parameters developed in this work: (a) unit cell, (b) overview of the  $2 \times 2$  supercell



(a)



(b)

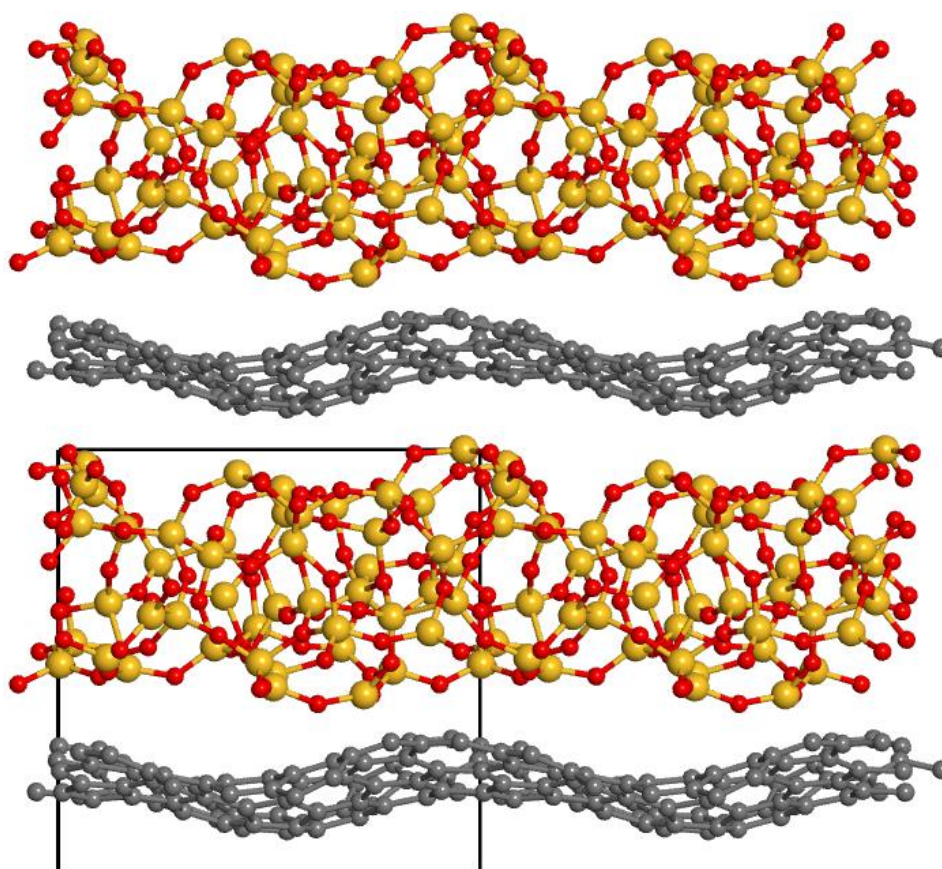
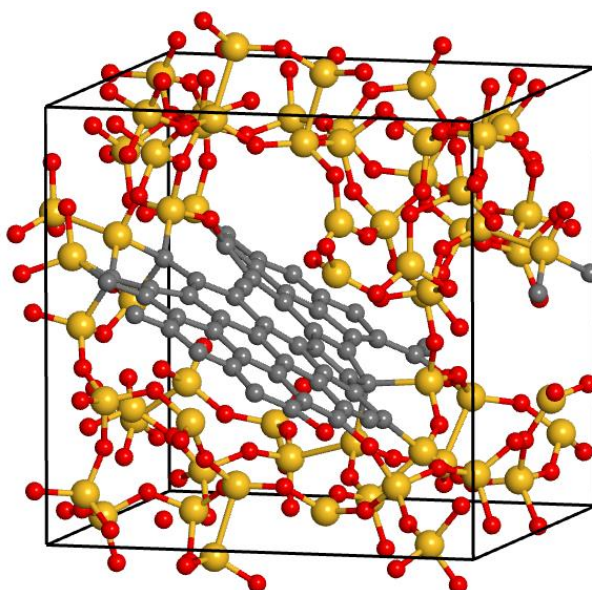


Figure 3.12 The structure of  $\text{SiC}_{1.65}\text{O}_{1.6}$  constructed by UTA1: (a) unit cell, (b) overview of the  $2 \times 2$  supercell



(a)



(b)

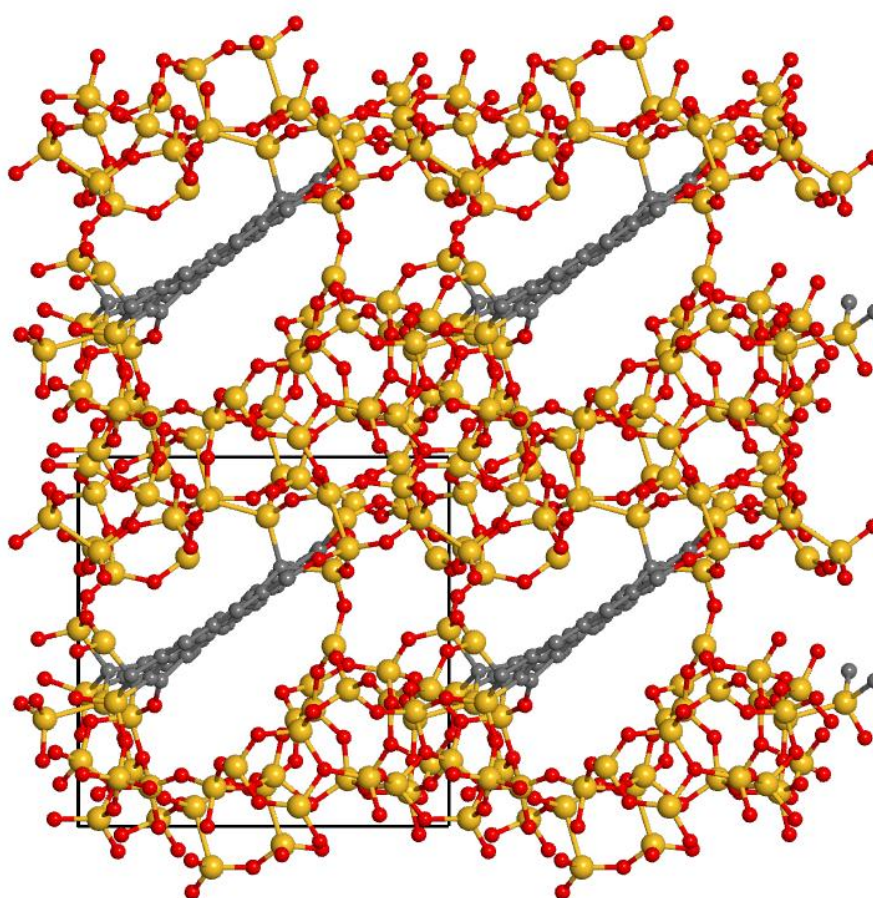
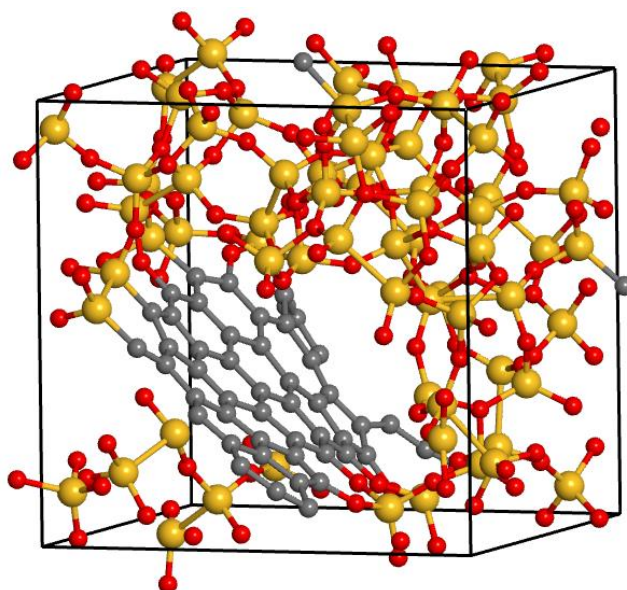


Figure 3.13 The structure of  $\text{SiC}_{0.8}\text{O}_{1.6}$  constructed by the parameters developed in this work: (a) unit cell, (b) overview of the  $2 \times 2$  supercell



(a)



(b)

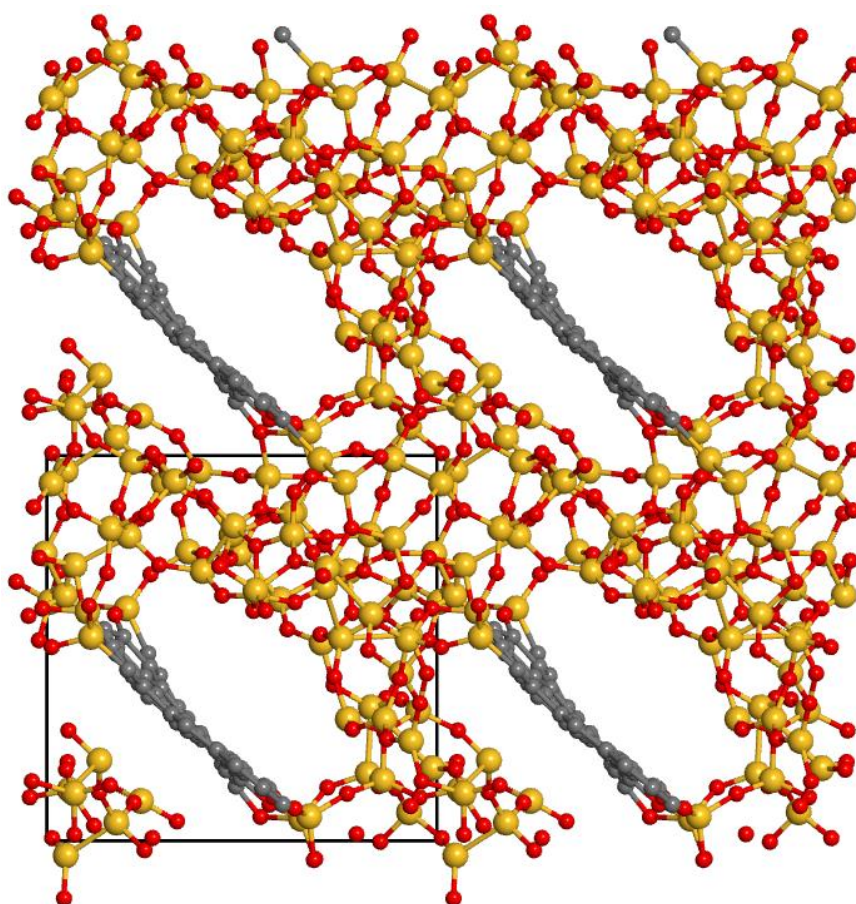
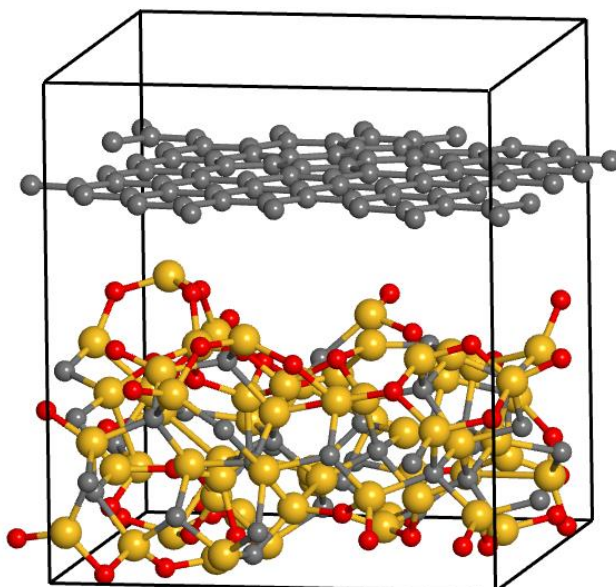


Figure 3.14 The structure of  $\text{SiC}_{0.8}\text{O}_{1.6}$  constructed by UTA1: (a) unit cell, (b) overview of the  $2 \times 2$  supercell



(a)



(b)

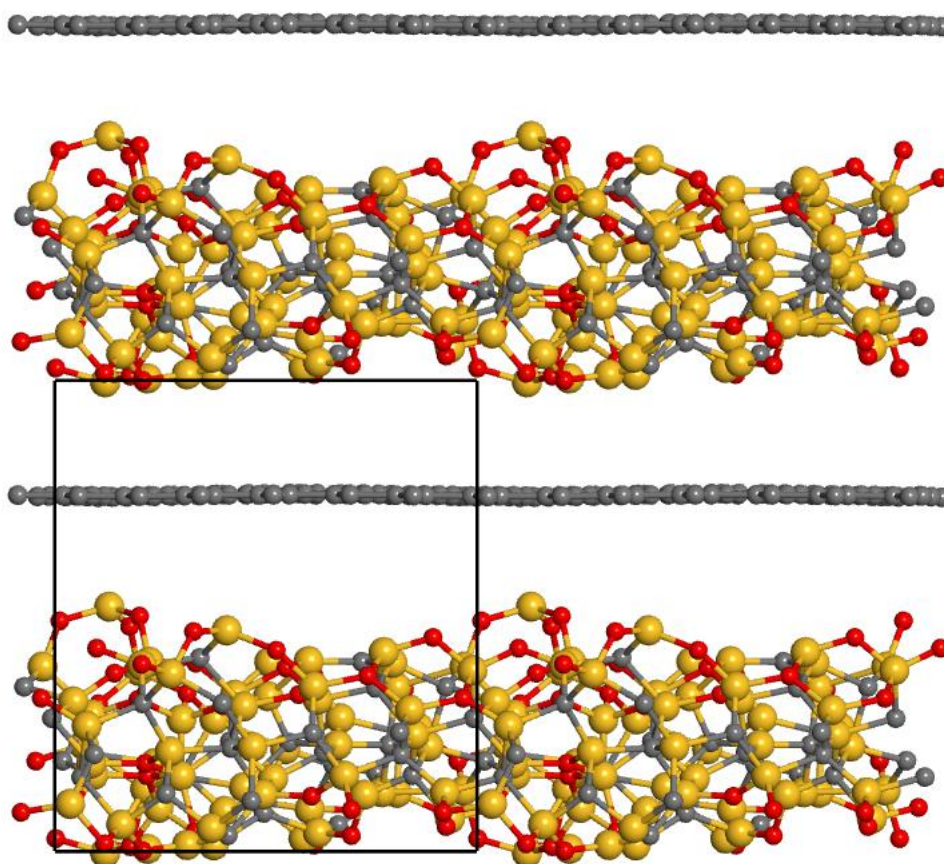
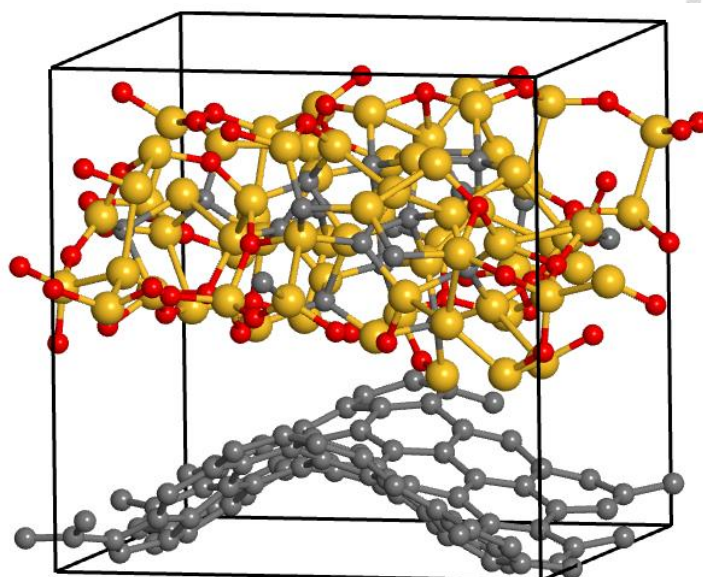


Figure 3.15 The structure of  $\text{SiC}_{1.65}\text{O}_{0.6}$  constructed by the parameters developed in this work: (a) unit cell, (b) overview of the  $2 \times 2$  supercell



(a)



(b)

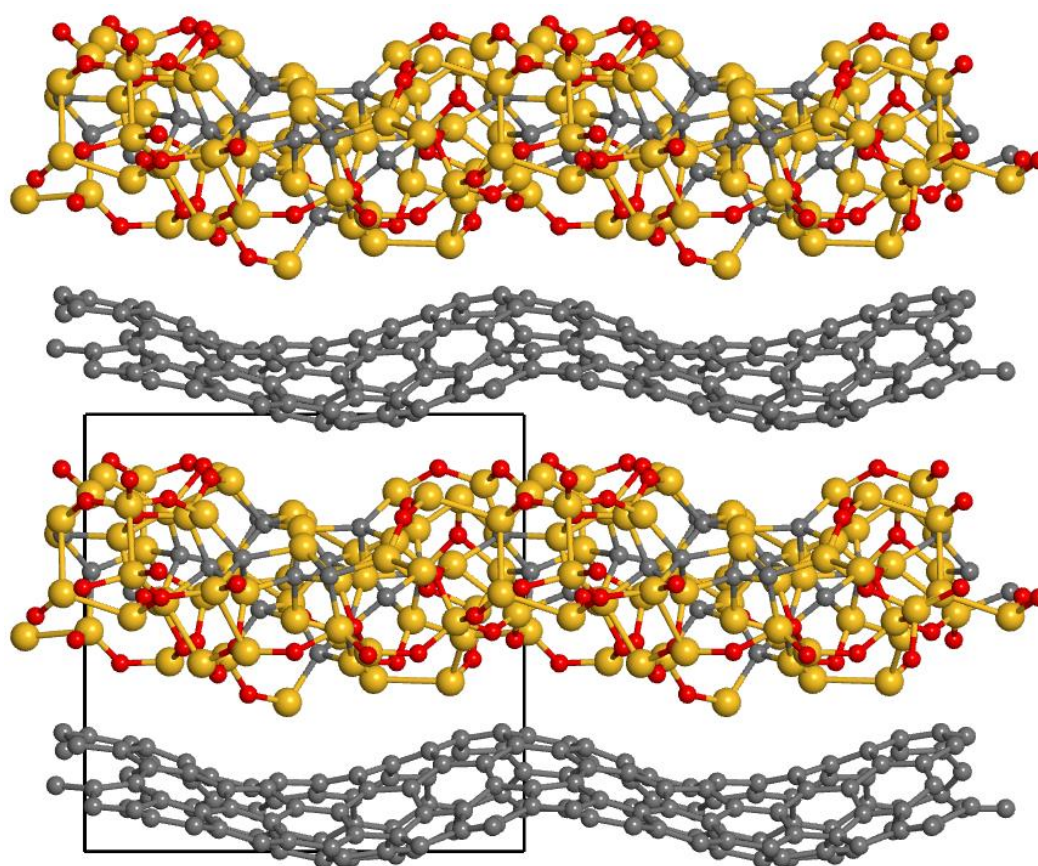


Figure 3.16 The structure of  $\text{SiC}_{1.65}\text{O}_{0.6}$  constructed by UTA1: (a) unit cell, (b) overview of the  $2 \times 2$  supercell

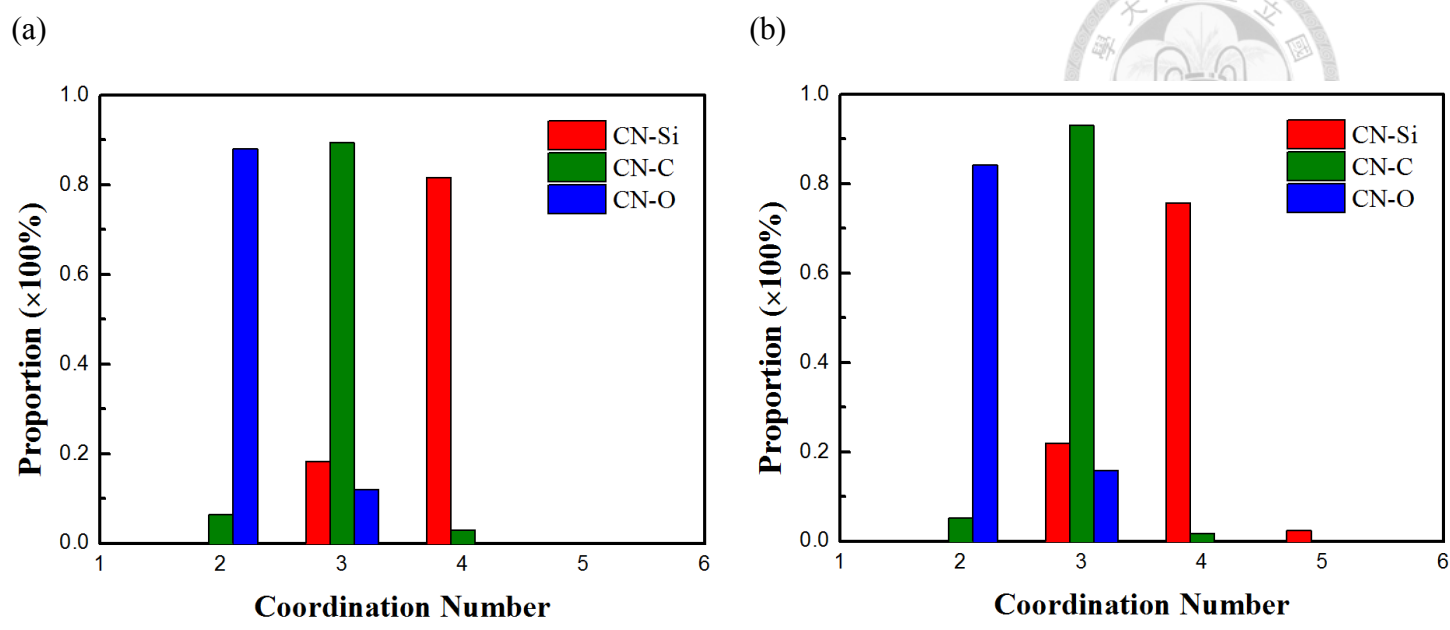


Figure 3.17 Atomistic coordination distribution of  $\text{SiC}_{2.2}\text{O}_{1.6}$ : (a) this work, (b) UTA1

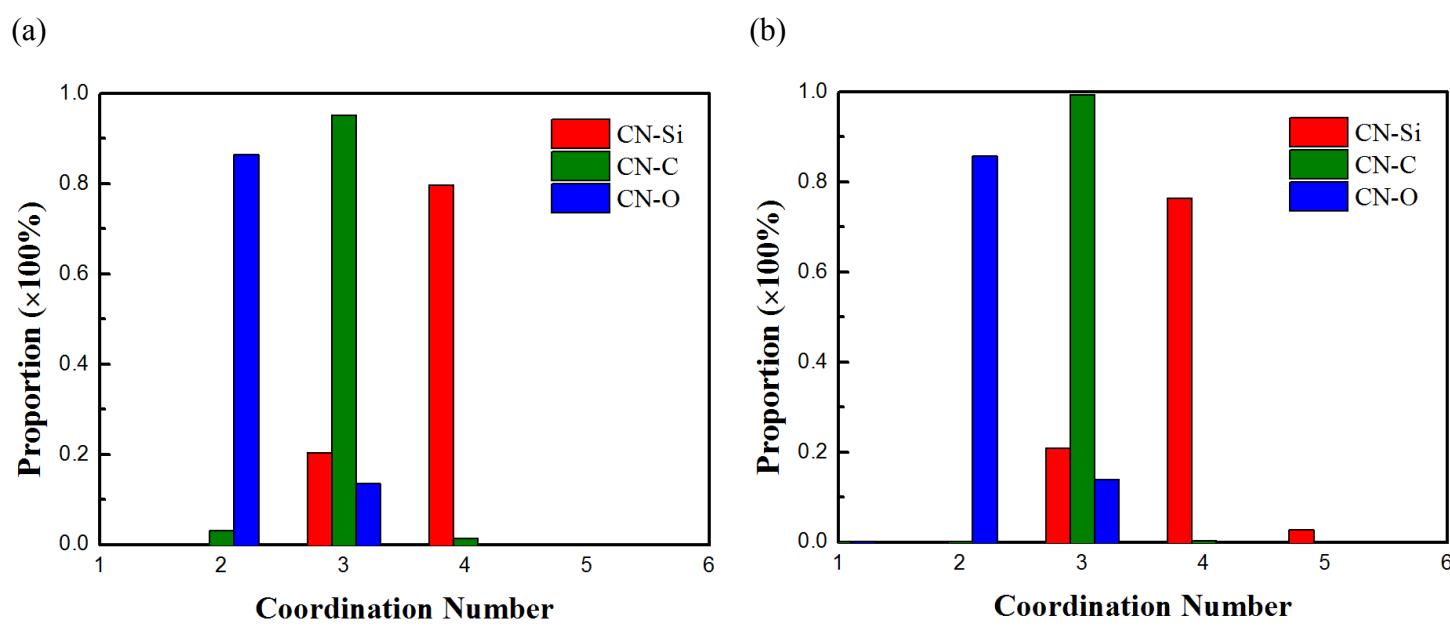


Figure 3.18 Atomistic coordination distribution of  $\text{SiC}_{1.65}\text{O}_{1.6}$ : (a) this work, (b) UTA1

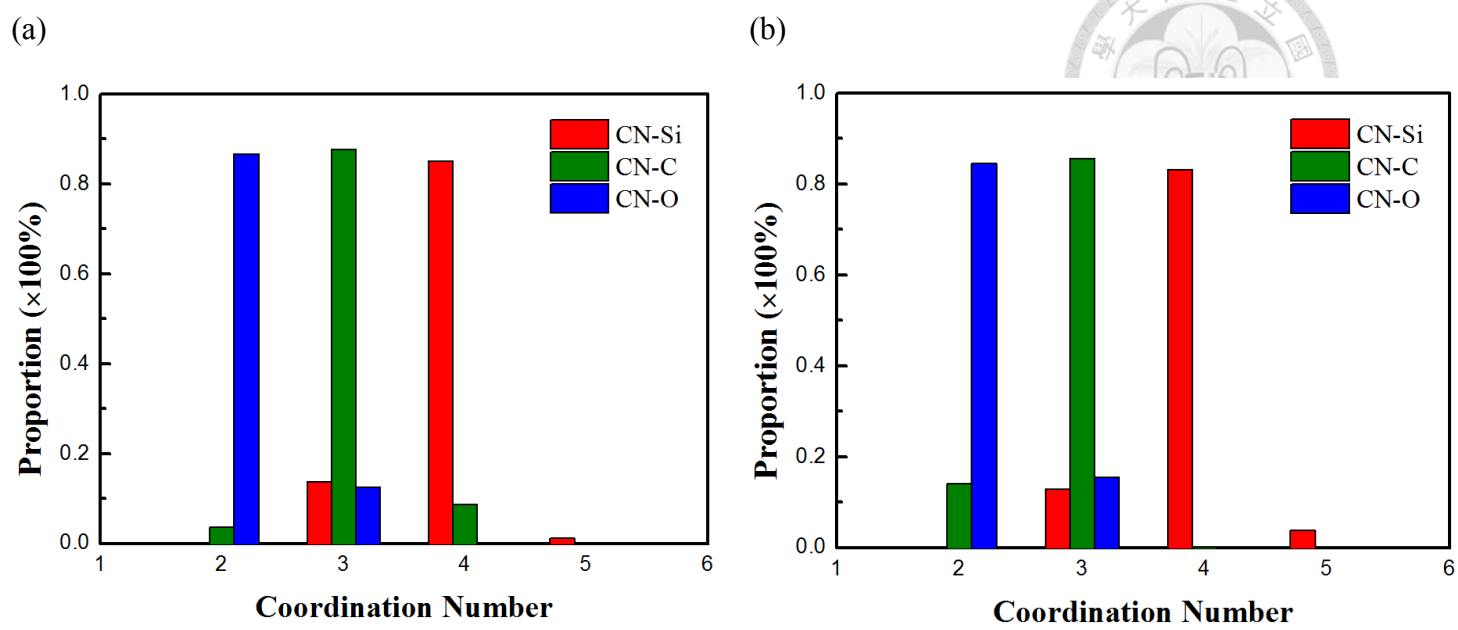


Figure 3.19 Atomistic coordination distribution of  $\text{SiC}_{0.8}\text{O}_{1.6}$ : (a) this work, (b) UTA1

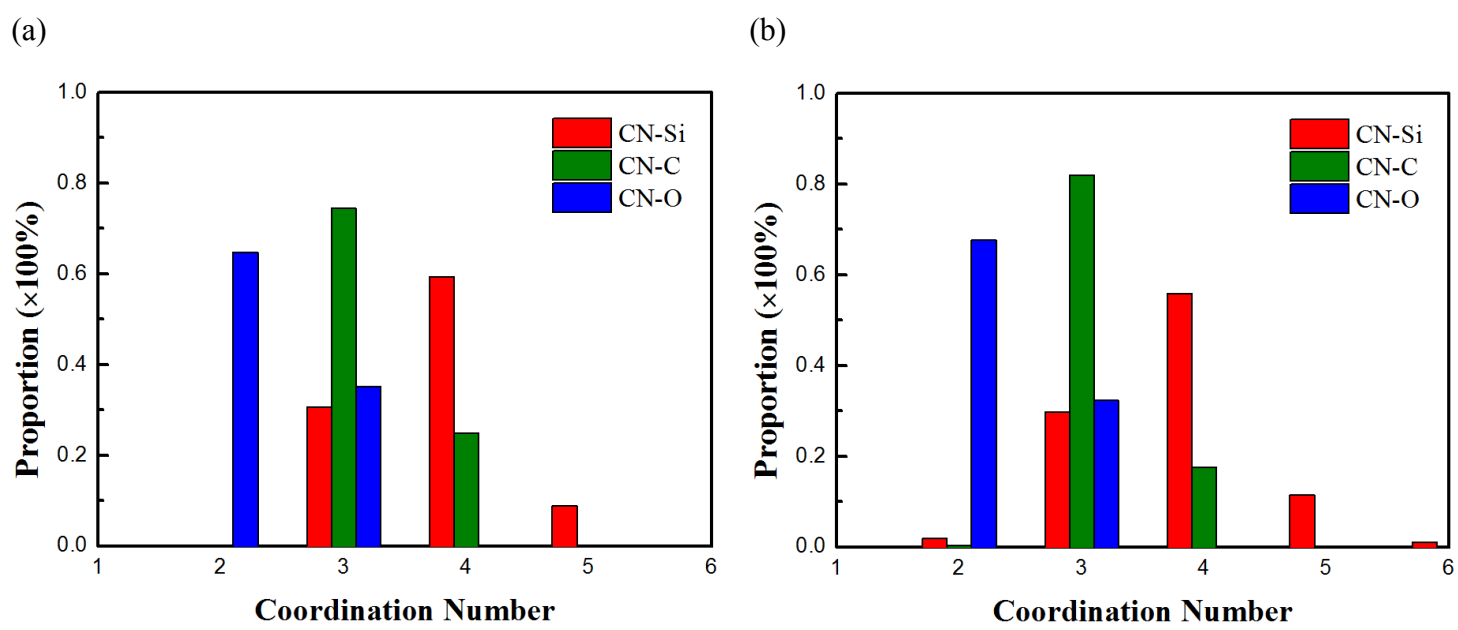


Figure 3.20 Atomistic coordination distribution of  $\text{SiC}_{0.8}\text{O}_{1.6}$ : (a) this work, (b) UTA1





### 3.3.3 Stability of amorphous SiOC

In this section, the stability of amorphous SiOCs is discussed. Here, we applied the concept of formation energy to compare the stability of SiOC structures constructed via our parameters and UTA1 parameters in each concentration. The formation energies per Si atom ( $E_f$ ) of different SiOC structures are given by

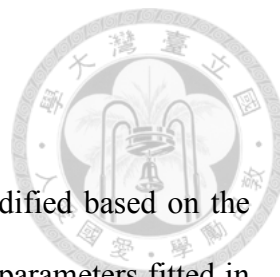
$$E_f = E_{SiO_aC_b} - (E_{Si} + a \cdot E_{O_2} + b \cdot E_{graphite}) \quad (\text{eq. 3-4})$$

$E_{SiO_aC_b}$  is the total energy of SiOC structure divided by the amount of silicon atoms in the structure;  $E_{Si}$ ,  $E_{O_2}$  and  $E_{graphite}$  are the per-atom energies of silicon crystal, oxygen molecule and graphite, respectively.

In order to compare the formation energies of structures constructed in different ReaxFF potential parameters, DFT calculations are applied. The results are shown in Table 3.6. As we can see, in every concentration, the formation energies of structures constructed via the parameters fitted in this work are lower than the formation energies of the structures constructed via UTA1 parameters. It means that the structures built by our parameters are thermodynamically more stable. This is attributed to the flatter free carbon layers, which lower the strain energy in free carbon phase, and the less over- and under-coordinated atoms in the system.

Table 3.6 The formation energy of amorphous SiOC

$E_f$ (eV/atom)	This work	UTA1
$SiC_{2.2}O_{1.6}$	-16.43	-15.95
$SiC_{1.65}O_{1.6}$	-14.02	-13.91
$SiC_{0.8}O_{1.6}$	-9.77	-9.70
$SiC_{1.65}O_{0.6}$	-9.82	-9.56



### 3.4 Summary

In this chapter, a set of Si/O/C ReaxFF potential model is modified based on the parameter set from Ponomarev et al. (UTA1). The validation of the parameters fitted in this work and the construction of amorphous SiOC structures in different concentrations are done.

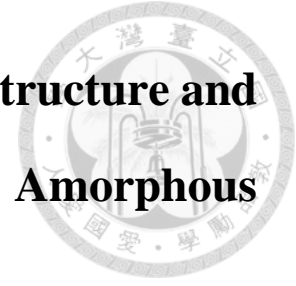
First, the validation of the parameters fitted in this work shows the better performance than UTA1 parameters in lattice constants, elastic constants, cohesive energies as well as the energy volume curves of diamond and graphite. In terms of binary systems, the elastic constants and cohesive energies are improved with a little sacrifice on lattice constants of SiO<sub>2</sub> ( $\alpha$ -quartz) and SiC ( $\beta$ -SiC).

Second, the construction of amorphous SiOC structures in four different concentrations, SiC<sub>2.2</sub>O<sub>1.6</sub>, SiC<sub>1.65</sub>O<sub>1.6</sub>, SiC<sub>0.8</sub>O<sub>1.6</sub> and SiC<sub>1.65</sub>O<sub>0.6</sub>, shows that due to the above improvements, especially for the elastic constants of SiC, the carbon atoms are more likely to have the tendency to be discovered in SiOC glass phase. Simultaneously, the decrease of carbon atoms in free carbon phase make the free carbon layers in our model flatter compared to those in UTA1's model.

Third, the calibrations of elastic constants and cohesive energies of SiO<sub>2</sub> and SiC indirectly improve the original high tolerance in over- and under-coordinated silicon atoms and three-coordinated oxygen atoms of UTA1 potential. Therefore, the coordination defects are reduced in amorphous SiOC structures built via our potential parameters.

Finally, thanks to the above improvements, the formation energies of structures constructed by the parameters fitted in this work are all lower than the formation energies of the structures constructed via UTA1 parameters. In other words, the structures built by our parameters are thermodynamically more stable.

# Chapter 4 First-principles Study of the Structure and Electronic Properties of Amorphous Silicon Oxycarbide



## 4.1 Introduction

As we mentioned in Chapter 1, Liao et al. [38], [39] constructed the amorphous SiOC structures through a mixed process. The melt-and-quench simulations via classical MD were conducted based on the Tersoff potential and the parameters for SiO<sub>2</sub> and SiC, following by annealing and geometry optimization in DFT calculations. The results are shown in Figure 4.1. The segregation of carbon atoms in the structures is observed. However, the free carbon phase look much denser than graphite-like amorphous carbon. It can be attributed to the poor description of graphitic carbon by Tersoff potential [40].

On the other hand, Sun et al. [11] used evolutionary algorithm implemented in the USPEX program to construct the initial SiOC structure instead of carrying out melt-and-quench MD. The structure was then subject to annealing by *ab initio* MD at 1200K. The final structure is shown in Figure 4.2. The generated structure contained the major feature of amorphous SiOC including segregated carbon network, SiO<sub>x</sub>C<sub>4-x</sub> tetrahedra and micropores (voids). Nevertheless, the feature of graphite-like amorphous carbon in free carbon phase was not clear probably since the simulation cell was not large enough (138 atoms).

In this chapter, we construct the amorphous SiOC structures in six different concentrations, which are SiC<sub>3.3</sub>O<sub>1.6</sub>, SiC<sub>2.2</sub>O<sub>1.6</sub>, SiC<sub>1.65</sub>O<sub>1.6</sub>, SiC<sub>0.8</sub>O<sub>1.6</sub>, SiC<sub>1.65</sub>O<sub>1.1</sub> and SiC<sub>1.65</sub>O<sub>0.6</sub>, via *ab initio* melt-and-quench MD simulations. By comparing the free carbon proportion, SiO<sub>x</sub>C<sub>4-x</sub> tetrahedra distributions, pore volume, specific surface area and local

density of states of the SiOC structures in different concentrations, we aim to clarify the effect of carbon and oxygen contents on structural properties and electronic structures of amorphous SiOCs.

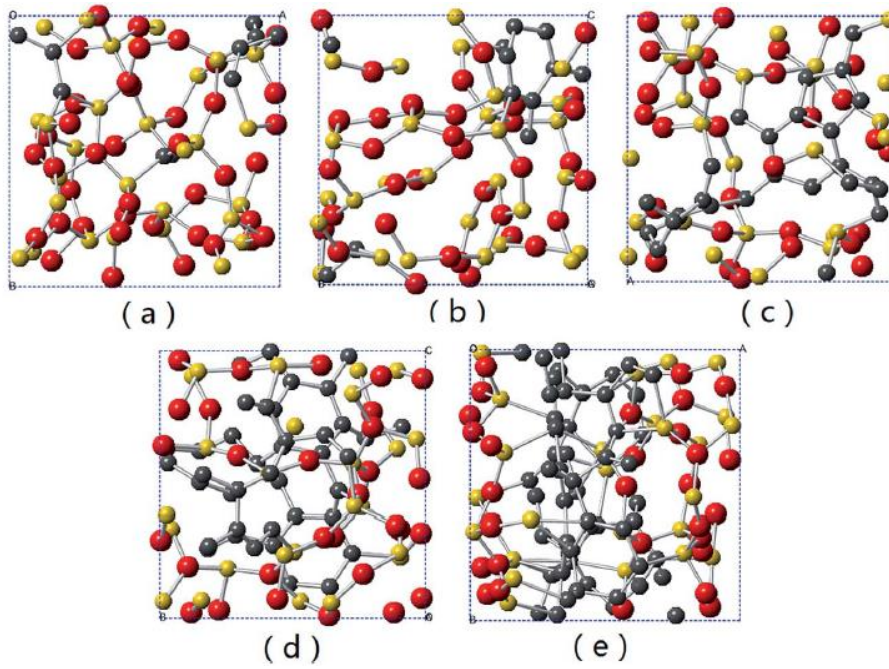
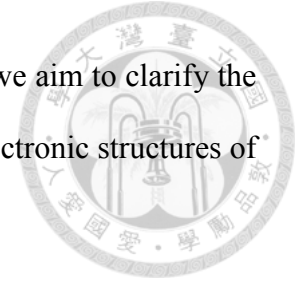


Figure 4.1 Amorphous SiOC structures: (a)  $\text{SiC}_{1/3}\text{O}_{4/3}$ , (b)  $\text{SiC}_{2/5}\text{O}_{6/5}$ , (c)  $\text{SiCO}_{6/5}$ , (d)  $\text{SiC}_{8/5}\text{O}_{6/5}$ , (e)  $\text{SiC}_{11/5}\text{O}_{6/5}$  [38]

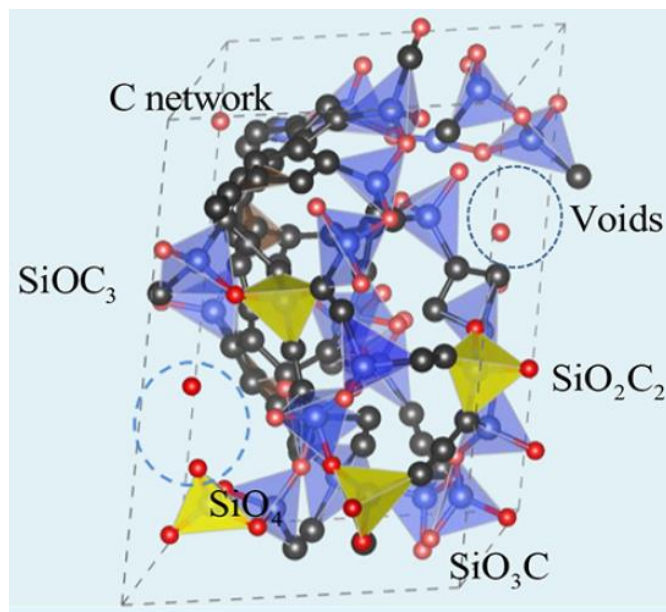
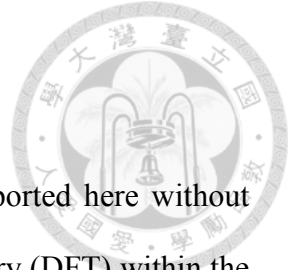


Figure 4.2 The structure of  $\text{SiC}_{2.43}\text{O}_{1.5}$  [11]



## 4.2 Computational details

All atomic structures, energetics, and electronic properties reported here without farther mention were calculated based on the density functional theory (DFT) within the generalized gradient approximation (GGA) with the parametrization of Perdew–Burke–Ernzerhof (PBE) <sup>[63]</sup> for the exchange-correlation functional as implemented in the well-established Vienna ab initio simulation package (VASP) <sup>[64]-[66]</sup>. The valence electron wave functions were expanded in plane-wave basis sets and the projector augmented wave (PAW) method <sup>[67]</sup> was used to describe the core-electron interactions. The plane-wave cut-off energy was set to be 500 eV for both the geometric optimization and the electronic property calculations. The Brillouin zone samplings were performed with a  $2 \times 2 \times 2$  k-point grid in the Monkhorst-Pack scheme for the geometry optimization and with an increased k-point mesh up to  $5 \times 5 \times 5$  for the electronic properties calculation. During the geometry optimization, all atoms in the supercell were fully relaxed with the conjugated gradient method until the residual forces acting on the constituent atoms become less than  $0.05 \text{ eV/\AA}$ .

### 4.2.1 Melt-and-quench procedures to construct amorphous silicon oxycarbide

The structures of SiOC were constructed by melt-and-quench method simulated via *ab initio* MD simulations. In this MD simulation, the cut-off energy was set to 350eV, and the k-points were sampled only at the Gamma point. The time step between each iteration was 1 fs. We considered six SiOC concentrations:  $\text{SiC}_{3.3}\text{O}_{1.6}$ ,  $\text{SiC}_{2.2}\text{O}_{1.6}$ ,  $\text{SiC}_{1.65}\text{O}_{1.6}$ ,  $\text{SiC}_{0.8}\text{O}_{1.6}$ ,  $\text{SiC}_{1.65}\text{O}_{1.1}$  and  $\text{SiC}_{1.65}\text{O}_{0.6}$ . For each concentration, we set the total number of atoms up to around 200 in the systems to ensure the structural characteristics can be

observed. The exact atomistic compositions of the systems is shown in Table 4.1.

The melt-and-quench procedure was the same as that mentioned in section 3.2.3. For each concentration, three structures were sampled.

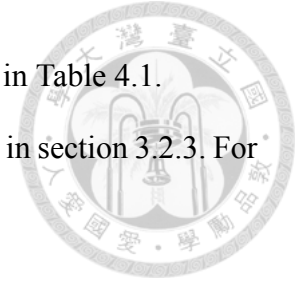
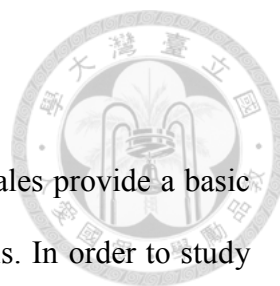


Table 4.1 Atomistic compositions of SiOC samples

	Si	O	C	Total
SiC <sub>3.3</sub> O <sub>1.6</sub>	33	53	110	196
SiC <sub>2.2</sub> O <sub>1.6</sub>	40	64	88	192
SiC <sub>1.65</sub> O <sub>1.6</sub>	46	74	76	196
SiC <sub>0.8</sub> O <sub>1.6</sub>	58	93	46	197
SiC <sub>1.65</sub> O <sub>1.1</sub>	50	55	83	188
SiC <sub>1.65</sub> O <sub>0.6</sub>	60	36	99	195



## 4.2.2 Connolly Surface

Studies of the microscopic free-volume properties at atomic scales provide a basic understanding of the mechanical and physical properties of materials. In order to study the pore volume distribution in bulk simulated molecular models, the hard probe method was applied [69]. The schematic illustration of Connolly surface is shown in Figure 4.3. When the probe with its radius  $r_{probe}$  moved along the van der Waals surface of the system, the Connolly surface can be calculated [70].

In this study,  $r_{probe}$  was set to be  $1.09\text{\AA}$ , which is the ionic radii of Li ion. The pore volume (PV) in the systems is calculated by subtracting the volume covered by the Connolly surface from system volume, while the specific surface area (SSA) of the systems is the surface area of the Connolly surface.

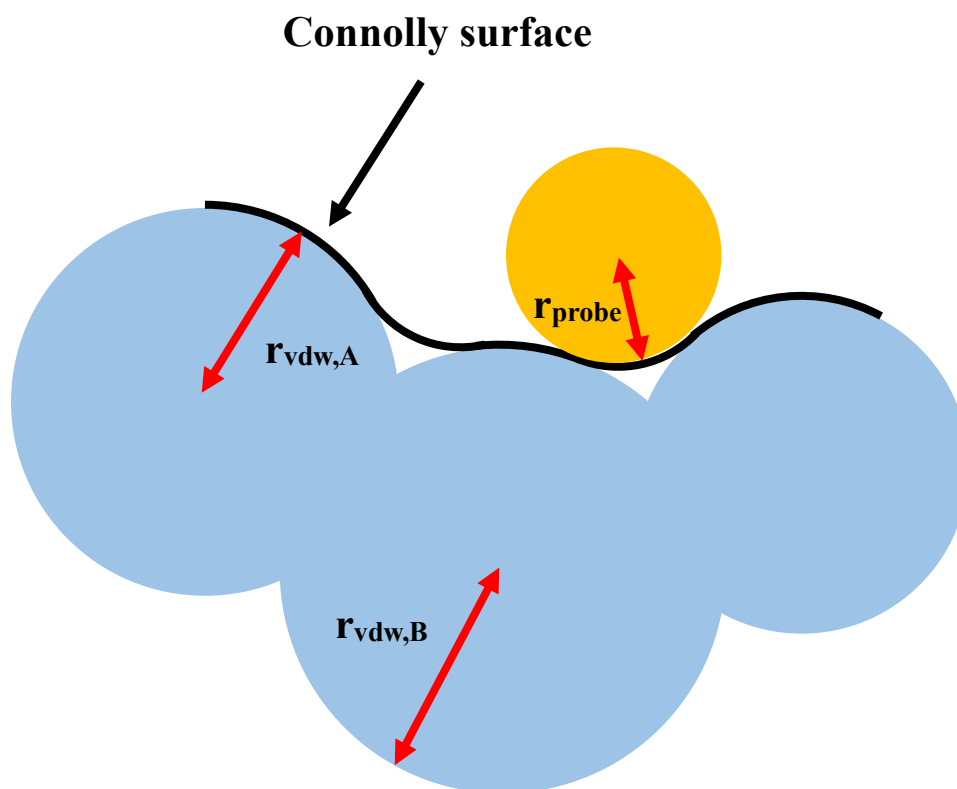
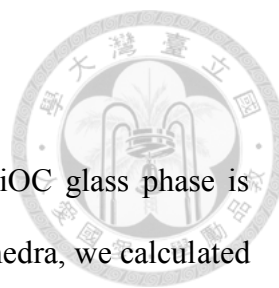


Figure 4.3 Schematic illustration of Connolly surface



### 4.2.3 $\text{SiO}_x\text{C}_{4-x}$ tetrahedra and free carbon calculation

In amorphous SiOC systems, it is commonly accepted that SiOC glass phase is composed of  $\text{SiO}_x\text{C}_{4-x}$  tetrahedra. To quantitatively analyze the tetrahedra, we calculated the number of C and O atoms binding with each Si atom in the system and categorized them into  $\text{SiC}_4$ ,  $\text{SiC}_3\text{O}$ ,  $\text{SiC}_2\text{O}_2$ ,  $\text{SiCO}_3$  and  $\text{SiO}_4$  as shown in Figure 4.4. Considering the first valley of the radial distribution functions of a- $\text{SiO}_2$  and a-SiC of 1.9 and 2.2, respectively,  $r \leq 1.9\text{\AA}$  and  $r \leq 2.2\text{\AA}$  are chosen as the representative cutoff radii for Si-O and Si-C bonds. In terms of free carbon phase, we define the carbon atoms that do not belong to any of  $\text{SiO}_x\text{C}_{4-x}$  tetrahedron as free carbon atoms. Likewise,  $r \leq 2.0\text{\AA}$  is selected as the representative cutoff radii for C-C bond based on the first valley of the radial distribution functions of a-C.

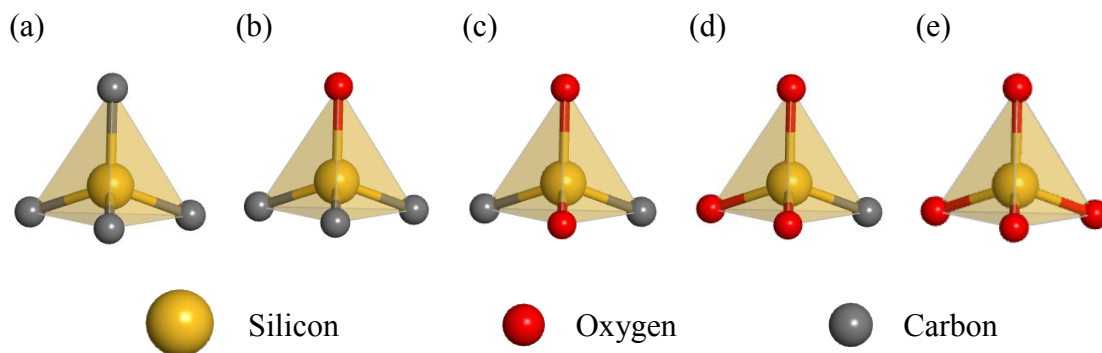


Figure 4.4  $\text{SiO}_x\text{C}_{4-x}$  tetrahedra: (a)  $\text{SiC}_4$ , (b)  $\text{SiC}_3\text{O}$ , (c)  $\text{SiC}_2\text{O}_2$ , (d)  $\text{SiCO}_3$ , (e)  $\text{SiO}_4$





## 4.3 Results and discussion

### 4.3.1 Structures of amorphous SiOC

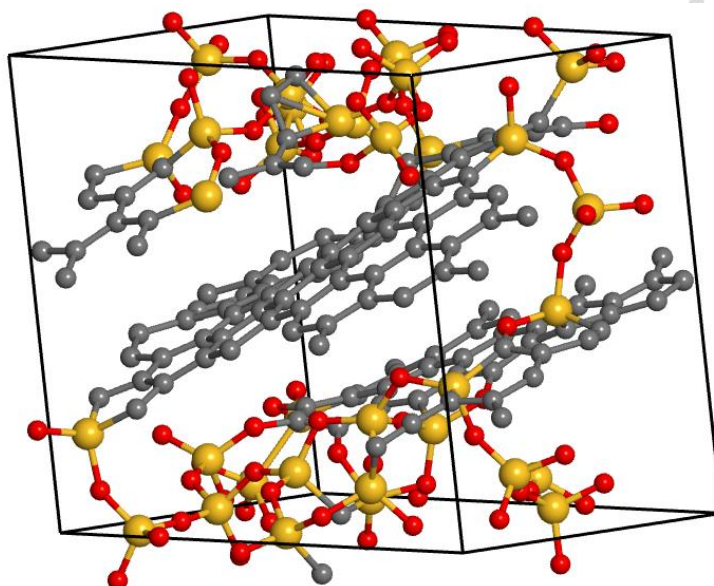
Different from the previous chapter, here, we constructed the amorphous SiOC structures in six different concentrations, which are  $\text{SiC}_{3.3}\text{O}_{1.6}$ ,  $\text{SiC}_{2.2}\text{O}_{1.6}$ ,  $\text{SiC}_{1.65}\text{O}_{1.6}$ ,  $\text{SiC}_{0.8}\text{O}_{1.6}$ ,  $\text{SiC}_{1.65}\text{O}_{1.1}$  and  $\text{SiC}_{1.65}\text{O}_{0.6}$ , by *ab initio* melt-and-quench MD simulations. The optimized structures are shown in Figure 4.5 to Figure 4.10. Note that only the most stable structure among the three in each concentration would be shown.

First, the structure of  $\text{SiC}_{3.3}\text{O}_{1.6}$ , which has the highest carbon concentration, is shown in Figure 4.5. In the structure, we observe that the free carbon phase consists of a bilayer graphite-like amorphous carbon with a d-spacing of around 3.6 Å, which is close to the d-spacing of amorphous graphite. On the other hand, several carbon atoms were found in the SiOC glass region. The structures of  $\text{SiC}_{2.2}\text{O}_{1.6}$  is shown in Figure 4.6. With the decrease of carbon concentration, the free carbon phase turned from bilayer amorphous carbon into an amorphous graphene. Then, as the carbon concentration further decreased to  $\text{SiC}_{1.65}\text{O}_{1.6}$  and  $\text{SiC}_{0.8}\text{O}_{1.6}$ , whose structures are shown in Figure 4.7 and Figure 4.8 respectively, the area of free carbon got smaller and smaller, turning into cracked amorphous graphene dispersed in the structure. On the other hand, as the oxygen concentration decreased to  $\text{SiC}_{1.65}\text{O}_{1.1}$  and  $\text{SiC}_{1.65}\text{O}_{0.6}$ , whose structures are shown in Figure 4.9 and Figure 4.10 respectively, the free carbon phase gradually transformed from monolayer to bilayer amorphous graphene, while there were more and more carbon atoms and Si-Si bonds in the SiOC glass region.

For all concentrations above, free carbon phase as well as SiOC glass phase are observed. Moreover, compared to the carbon atoms in the structures constructed by ReaxFF potential model, the carbon atoms in the structures built by DFT calculations are much more likely to be discovered in SiOC glass region.



(a)



(b)

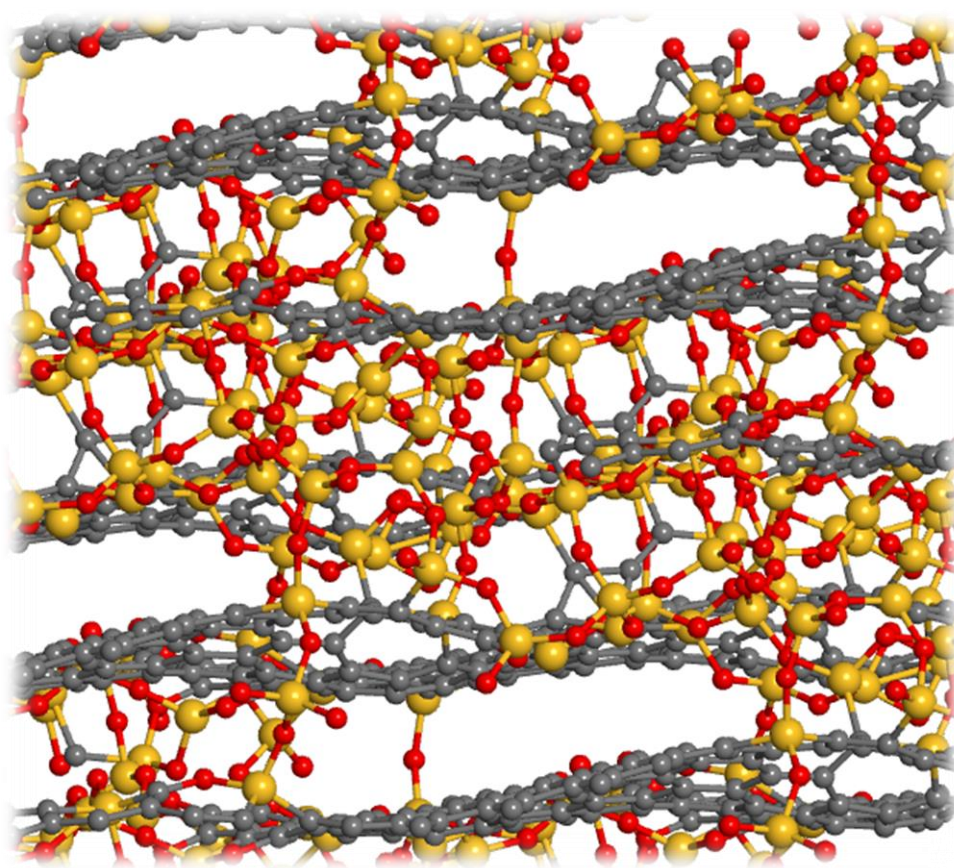
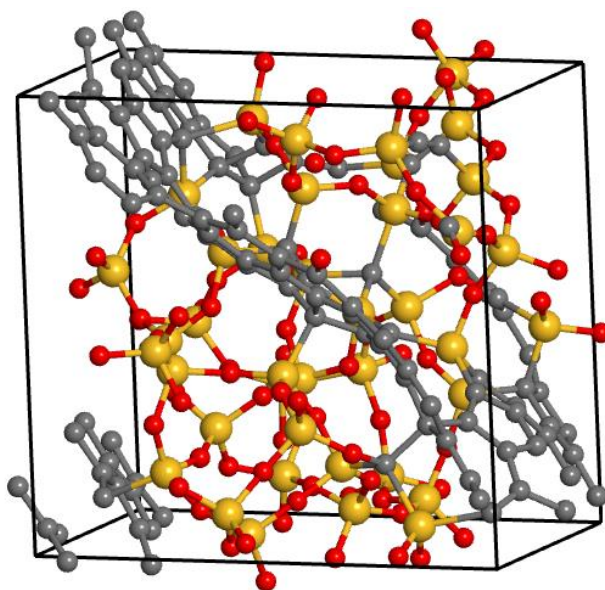


Figure 4.5 The structure of  $\text{SiC}_{3.3}\text{O}_{1.6}$ : (a) unit cell, (b) overview of the  $2 \times 2$  supercell



(a)



(b)

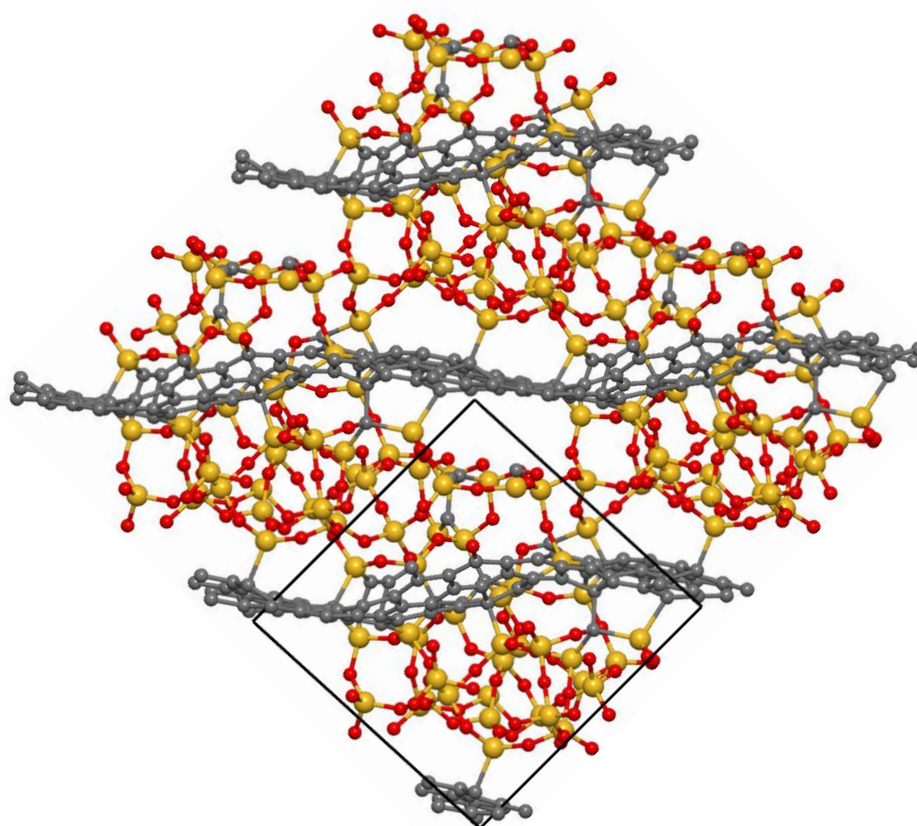
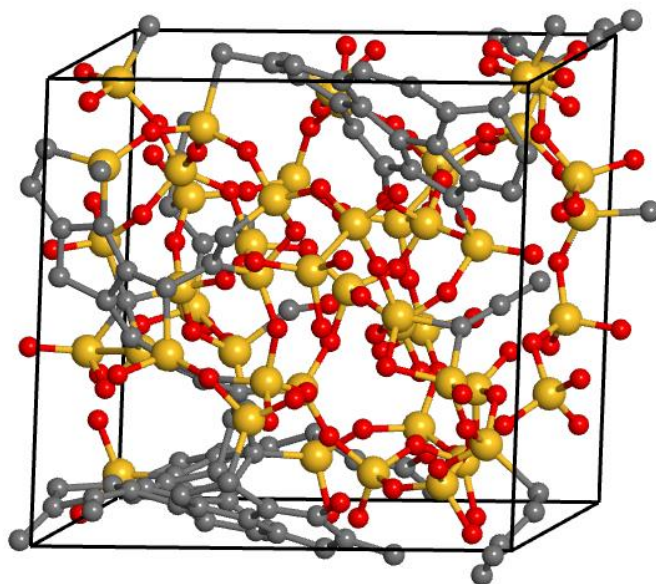


Figure 4.6 The structure of SiC<sub>2.2</sub>O<sub>1.6</sub>: (a) unit cell, (b) overview of the 2×2 supercell



(a)



(b)

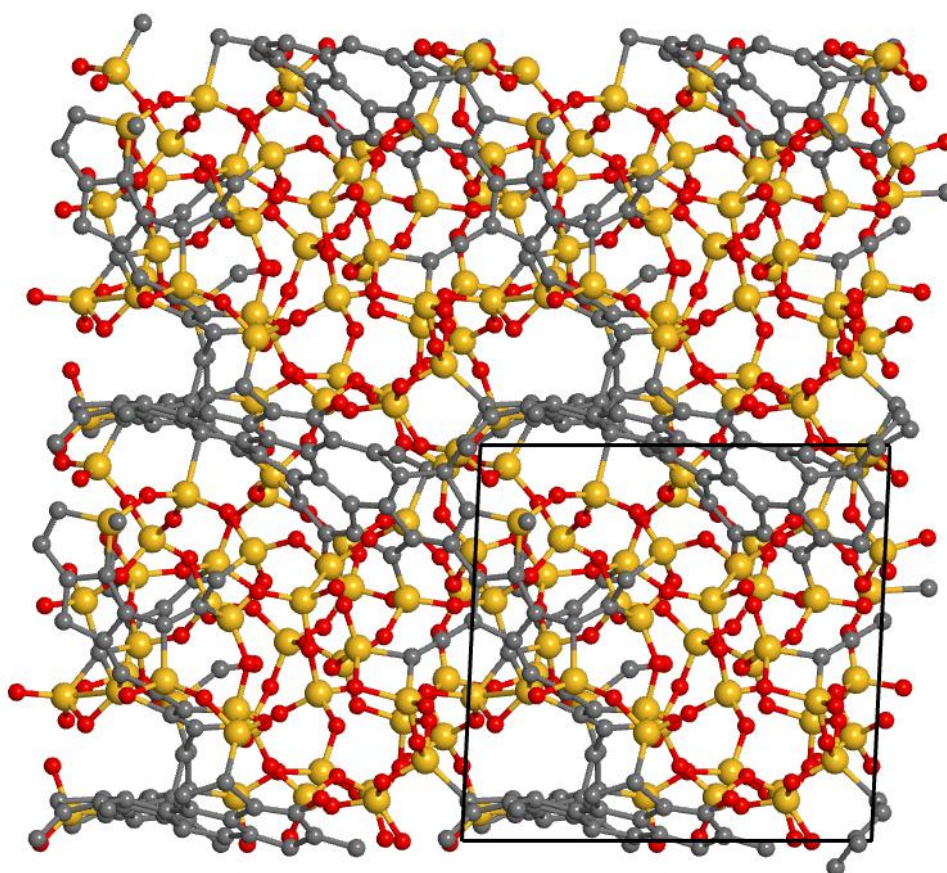
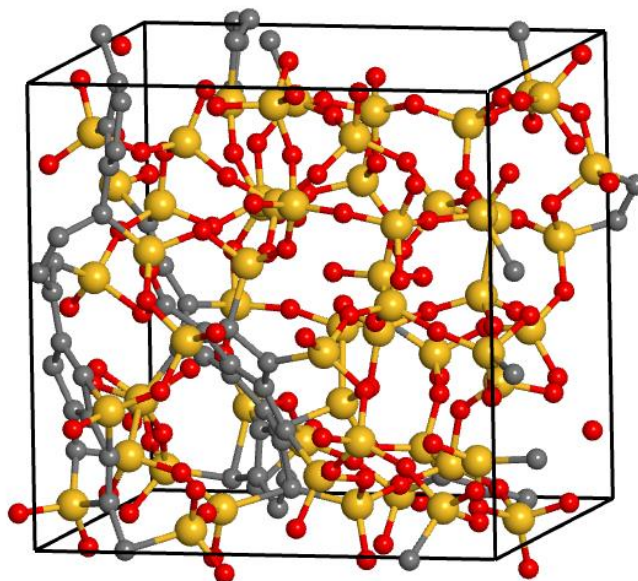


Figure 4.7 The structure of  $\text{SiC}_{1.65}\text{O}_{1.6}$ : (a) unit cell, (b) overview of the  $2 \times 2$  supercell



(a)



(b)

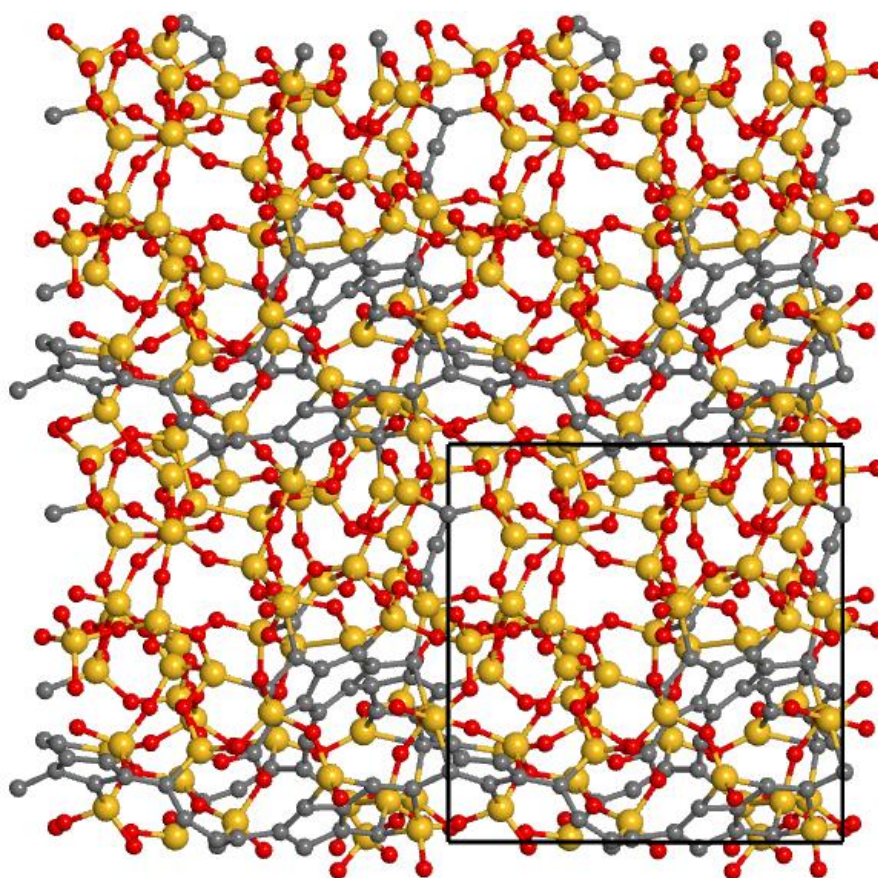
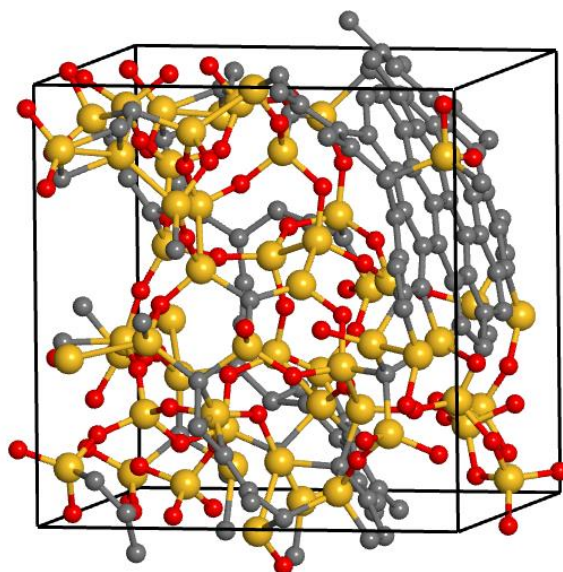


Figure 4.8 The structure of  $\text{SiC}_{0.8}\text{O}_{1.6}$ : (a) unit cell, (b) overview of the  $2 \times 2$  supercell



(a)



(b)

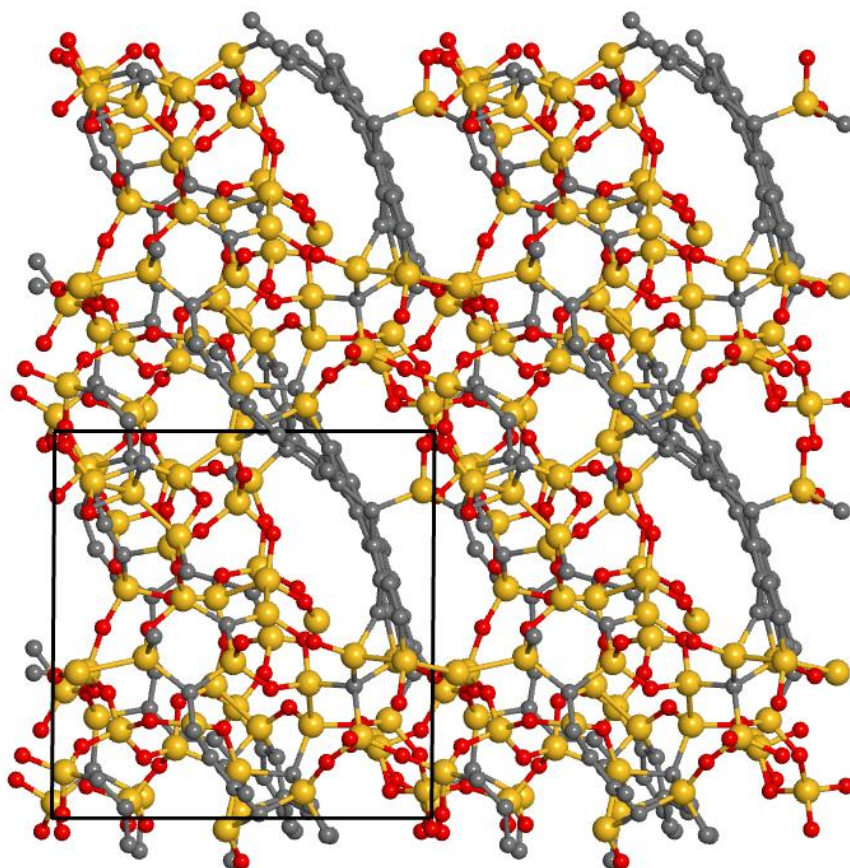
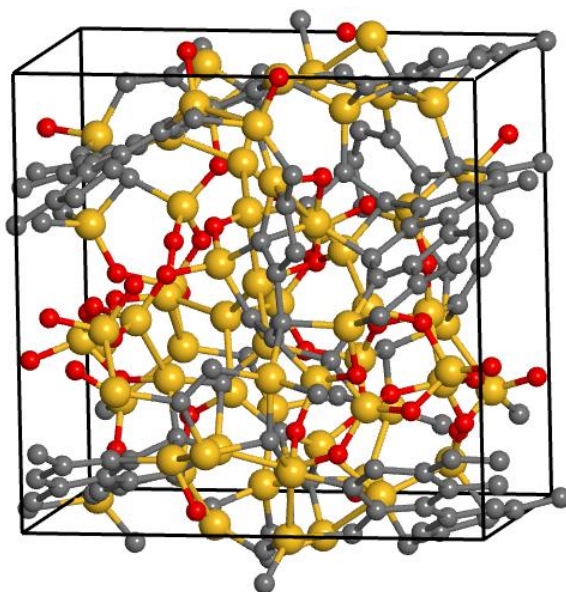


Figure 4.9 The structure of  $\text{SiC}_{1.65}\text{O}_{1.1}$ : (a) unit cell, (b) overview of the  $2 \times 2$  supercell



(a)



(b)

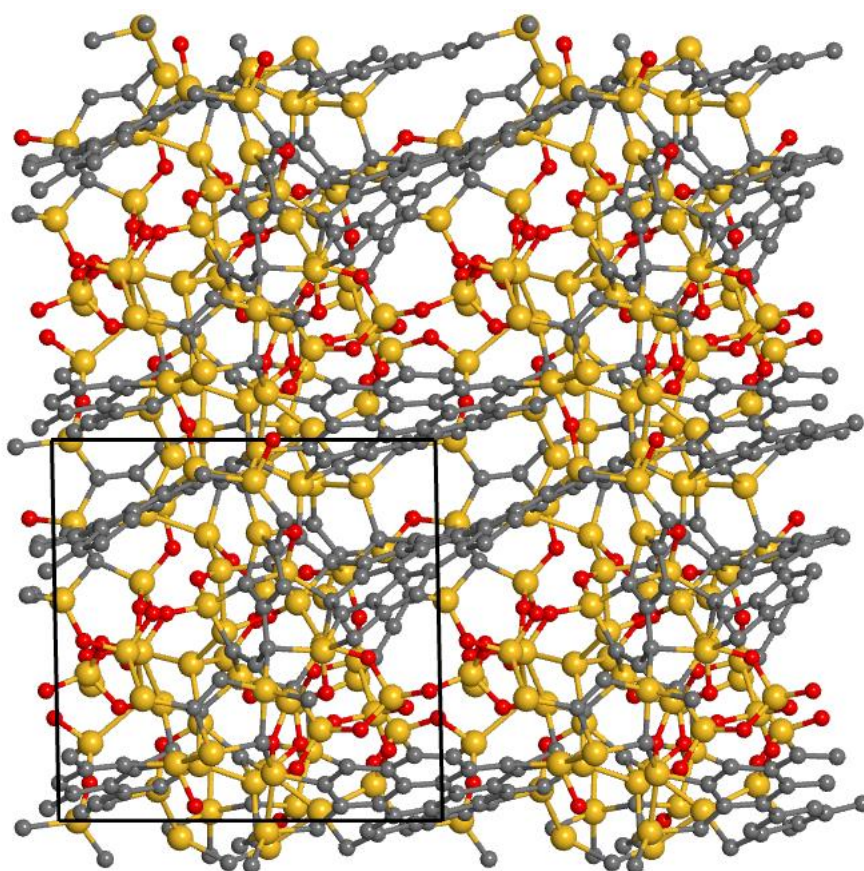
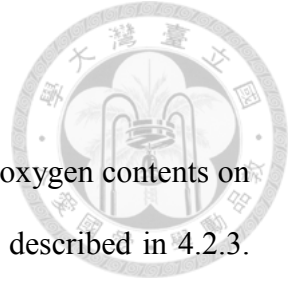


Figure 4.10 The structure of  $\text{SiC}_{1.65}\text{O}_{0.6}$ : (a) unit cell, (b) overview of the  $2 \times 2$  supercell



### 4.3.2 Free carbon distribution in amorphous SiOC

In this section, we are going to discuss the effect of carbon and oxygen contents on the free carbon phase. The definition of free carbon in this work is described in 4.2.3. Theoretically, the SiOC glasses are a stoichiometric mixture of  $\text{SiO}_2$  and  $\text{SiC}$ , comprising a random network of Si-O and Si-C bonds, which forms mixed  $\text{SiO}_x\text{C}_{4-x}$  tetrahedra. Thus, amorphous SiOC ceramics are often expressed as

$$\text{SiC}_{x+y}\text{O}_{2(1-x)} = \{x \cdot \text{SiC} + (1-x) \cdot \text{SiO}_2\} + y \cdot C_{free} \quad (\text{eq. 4-1})$$

The formula-predicted free carbon proportions are calculated as

$$X_{free \text{ carbon}} = \frac{y}{x+y} \quad (\text{eq. 4-2})$$

The free carbon proportions of  $\text{SiC}_{3.3}\text{O}_{1.6}$ ,  $\text{SiC}_{2.2}\text{O}_{1.6}$ ,  $\text{SiC}_{1.65}\text{O}_{1.6}$  and  $\text{SiC}_{0.8}\text{O}_{1.6}$  are shown in Figure 4.11. As the decrease of carbon concentration, both the formula-predicted free carbon proportions and actual free carbon proportions in the structures dropped. However, there were deviations between the free carbon proportions calculated by (eq. 4-2) and actual proportions in the structures constructed.

The free carbon proportions of  $\text{SiC}_{1.65}\text{O}_{1.6}$ ,  $\text{SiC}_{1.65}\text{O}_{1.1}$  and  $\text{SiC}_{1.65}\text{O}_{0.6}$  are shown in Figure 4.12. The results showed that the formula-predicted free carbon proportions and actual free carbon proportions of the structures shared the same trend. While the oxygen concentration decreased, the free carbon proportions would drop as well. Nevertheless, there were also deviations between the formula-predicted value and the actual value of the structures.

The existence of the deviations between the formula-predicted free carbon proportions and the actual free carbon proportions in the structures can be attributed to two reasons. First, the formula-predicted model is under the assumption that there isn't



any connection between SiOC glass phase and free carbon phase. Therefore, the carbon atoms in amorphous graphene/graphite of free carbon phase will not be bound with any atom in SiOC glass phase. However, there were several Si-C bonds at the edge of free carbon phase and between the free carbon phase and SiOC glass phase in the constructed structures, which therefore caused the deviations between the formula-predicted value and the calculated value. The other reason is that, due to the limitation of the simulation cell size in *ab initio* calculations, the effect above would be magnified compared to the actual SiOC samples synthesized by experiment through pyrolysis process.

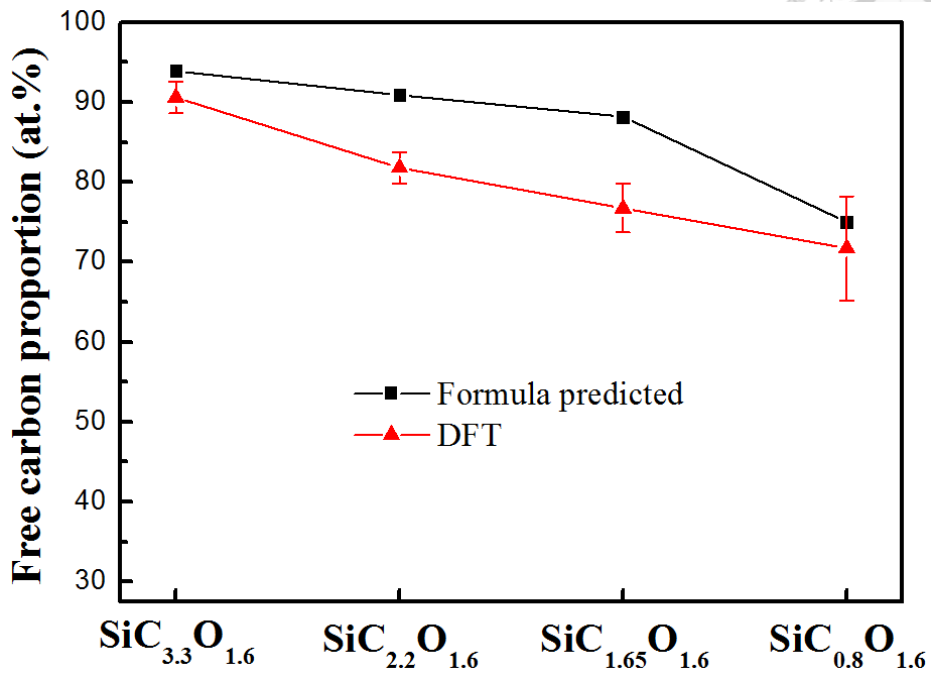


Figure 4.11 Free carbon proportions of SiC<sub>3.3</sub>O<sub>1.6</sub>, SiC<sub>2.2</sub>O<sub>1.6</sub>, SiC<sub>1.65</sub>O<sub>1.6</sub> and SiC<sub>0.8</sub>O<sub>1.6</sub>

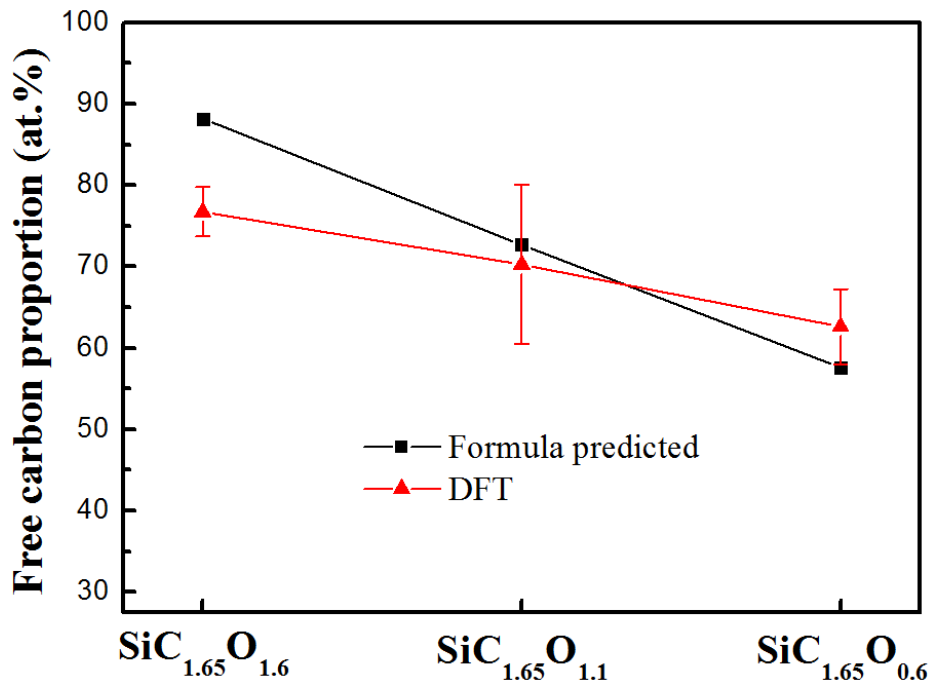
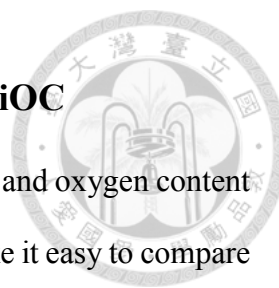


Figure 4.12 Free carbon proportions of SiC<sub>1.65</sub>O<sub>1.6</sub>, SiC<sub>1.65</sub>O<sub>1.1</sub> and SiC<sub>1.65</sub>O<sub>0.6</sub>



### 4.3.3 $\text{SiO}_x\text{C}_{4-x}$ tetrahedra distribution in amorphous SiOC

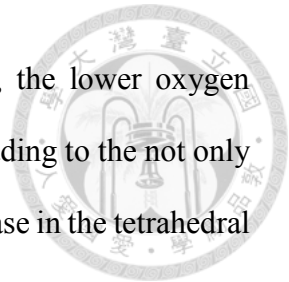
In this section, we are going to discuss about the effect of carbon and oxygen content on the distribution of  $\text{SiO}_x\text{C}_{4-x}$  tetrahedra in amorphous SiOC. To make it easy to compare the results among different concentrations, the number of each kind of tetrahedron were normalized by the total numbers of  $\text{SiO}_x\text{C}_{4-x}$  tetrahedra in structures of each concentration.

The distributions of  $\text{SiO}_x\text{C}_{4-x}$  tetrahedra in  $\text{SiC}_{3.3}\text{O}_{1.6}$ ,  $\text{SiC}_{2.2}\text{O}_{1.6}$ ,  $\text{SiC}_{1.65}\text{O}_{1.6}$  and  $\text{SiC}_{0.8}\text{O}_{1.6}$  are shown in Figure 4.13. The results show that as the carbon concentration rises, the fraction of  $\text{SiCO}_3$  tetrahedra decreases, while the fraction of  $\text{SiC}_3\text{O}$  tetrahedra increases. In terms of  $\text{SiO}_2\text{C}_2$ , its fractions are almost the same as those in  $\text{SiC}_{3.3}\text{O}_{1.6}$ ,  $\text{SiC}_{2.2}\text{O}_{1.6}$  and  $\text{SiC}_{1.65}\text{O}_{1.6}$ , yet the fraction in  $\text{SiC}_{0.8}\text{O}_{1.6}$  slightly decreases. Since the high concentration of oxygen in the structures, there are over 40% of  $\text{SiO}_4$  tetrahedra, which correspond to amorphous  $\text{SiO}_2$ , in all of the four concentrations. Furthermore,  $\text{SiC}_4$  tetrahedral unit is not seen in any of the structures in these concentrations, which is also attributed to the high oxygen content.

The distributions in  $\text{SiC}_{1.65}\text{O}_{1.6}$ ,  $\text{SiC}_{1.65}\text{O}_{1.1}$  and  $\text{SiC}_{1.65}\text{O}_{0.6}$  are shown in Figure 4.14. The fractions of tetrahedral units with higher carbon content, which are  $\text{SiC}_4$  and  $\text{SiC}_3\text{O}$ , increase with the lowering oxygen concentration. In contrast, the fractions of tetrahedral units with lower carbon content, which are  $\text{SiCO}_3$  and  $\text{SiO}_4$ , decrease with the lowering oxygen concentration. The exception occurs on the fraction of  $\text{SiCO}_3$  in  $\text{SiC}_{1.65}\text{O}_{1.1}$ , which is a bit higher than that in  $\text{SiC}_{1.65}\text{O}_{1.6}$ . However, if we put the fraction of tetrahedral units with lower carbon content, which are  $\text{SiCO}_3$  and  $\text{SiO}_4$  together, we can find it decreasing with the lowering oxygen concentration. In addition, for  $\text{SiO}_2\text{C}_2$ , its fractions are quite the same in  $\text{SiC}_{1.65}\text{O}_{1.6}$ ,  $\text{SiC}_{1.65}\text{O}_{1.1}$  and  $\text{SiC}_{1.65}\text{O}_{0.6}$ .

To summarize, the higher carbon concentration in amorphous SiOC causes the increase of the tetrahedral units with higher carbon content and the decrease of the

tetrahedral units with lower carbon content. Another point is that, the lower oxygen concentration causes the same effect as the rise of carbon content, leading to the not only increase in the tetrahedral units with more carbon atoms but the decrease in the tetrahedral units with less carbon atoms. To stress it again, the fractions of  $\text{SiO}_2\text{C}_2$  in all the concentrations are similar to each other, which is accounted for around 20%.



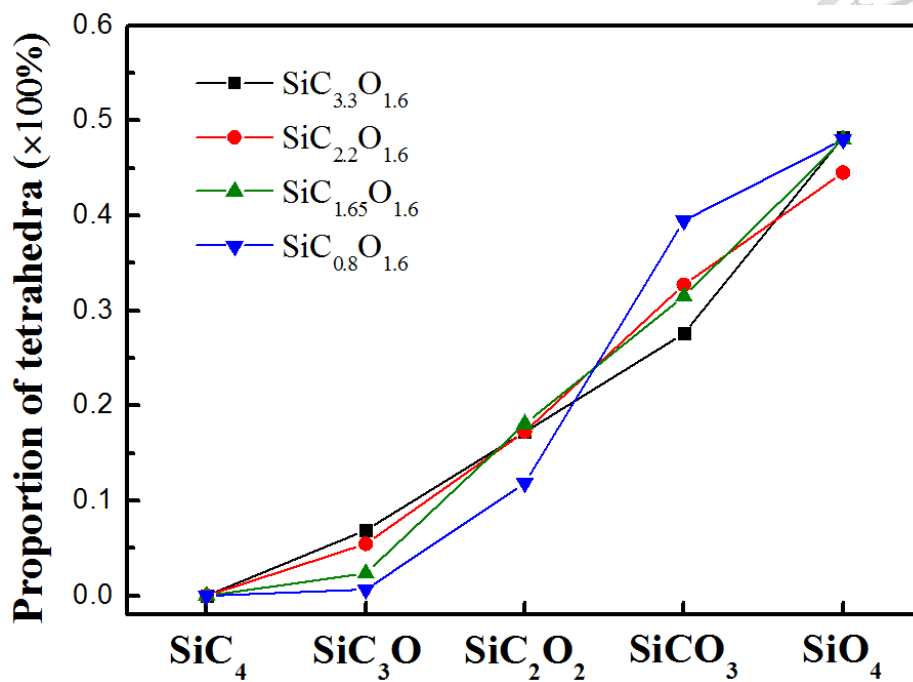


Figure 4.13 Distributions of SiO<sub>x</sub>C<sub>4-x</sub> tetrahedra in SiC<sub>3.3</sub>O<sub>1.6</sub>, SiC<sub>2.2</sub>O<sub>1.6</sub>, SiC<sub>1.65</sub>O<sub>1.6</sub> and SiC<sub>0.8</sub>O<sub>1.6</sub>

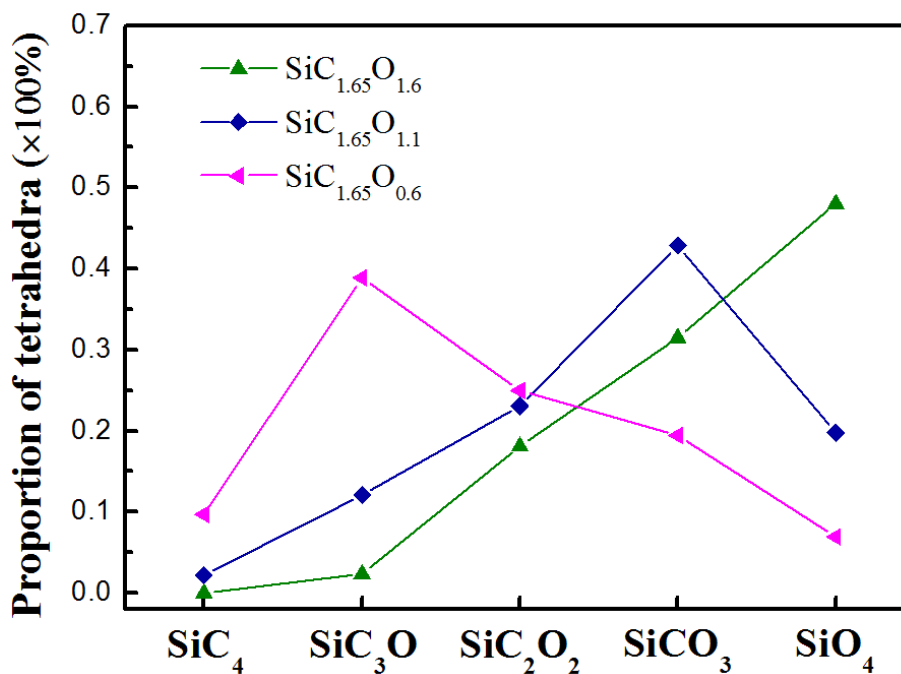


Figure 4.14 Distributions of SiO<sub>x</sub>C<sub>4-x</sub> tetrahedra in SiC<sub>1.65</sub>O<sub>1.6</sub>, SiC<sub>1.65</sub>O<sub>1.1</sub> and SiC<sub>1.65</sub>O<sub>0.6</sub>



#### 4.3.4 Pore volume and specific surface area of SiOC

In this section, we are going to discuss the effect of carbon and oxygen content on pore volume (PV) and specific surface area (SSA) of amorphous SiOC. The microporous spaces, which are defined as the spaces not covered by Connolly surface of the system, in each concentration are shown in Figure 4.15. The spaces covered by grey surfaces are the pores in the structures.

First, PV and SSA of  $\text{SiC}_{3.3}\text{O}_{1.6}$ ,  $\text{SiC}_{2.2}\text{O}_{1.6}$ ,  $\text{SiC}_{1.65}\text{O}_{1.6}$  and  $\text{SiC}_{0.8}\text{O}_{1.6}$  are shown in Figure 4.16. The results show that both PV and SSA show a downward trend with the increasing C/Si ratio from 0.8 to 2.2, since the increasing number of tetrahedral units with high C content, such as  $\text{SiC}_3\text{O}$  and  $\text{SiC}_4$ , can greatly densify the SiOC glass phase. However, when C/Si ratio further increase to 3.3, the formation of bilayer graphite-like amorphous carbon in free carbon phase (shown in Figure 4.15 (a)) induces an interlayer space, leading to the increase of PV and SSA instead.

Secondly, PV and SSA of  $\text{SiC}_{1.65}\text{O}_{1.6}$ ,  $\text{SiC}_{1.65}\text{O}_{1.1}$  and  $\text{SiC}_{1.65}\text{O}_{0.6}$  are shown in Figure 4.17. As the decreasing of oxygen concentration, both PV and SSA showed a downward trend, which is attributed to the increase of  $\text{SiC}_4$  and  $\text{SiC}_3\text{O}$  as well as the decrease of  $\text{SiCO}_3$  and  $\text{SiO}_4$  mentioned in previous section.

In summary, before the appearance of bilayer amorphous carbon in free carbon phase, the rising carbon concentration and the decreasing oxygen concentration will result in the drop of both PV and SSA in amorphous SiOC. On the other hand, the presence of bilayer amorphous carbon in free carbon phase will lead to the increase of PV and SSA.

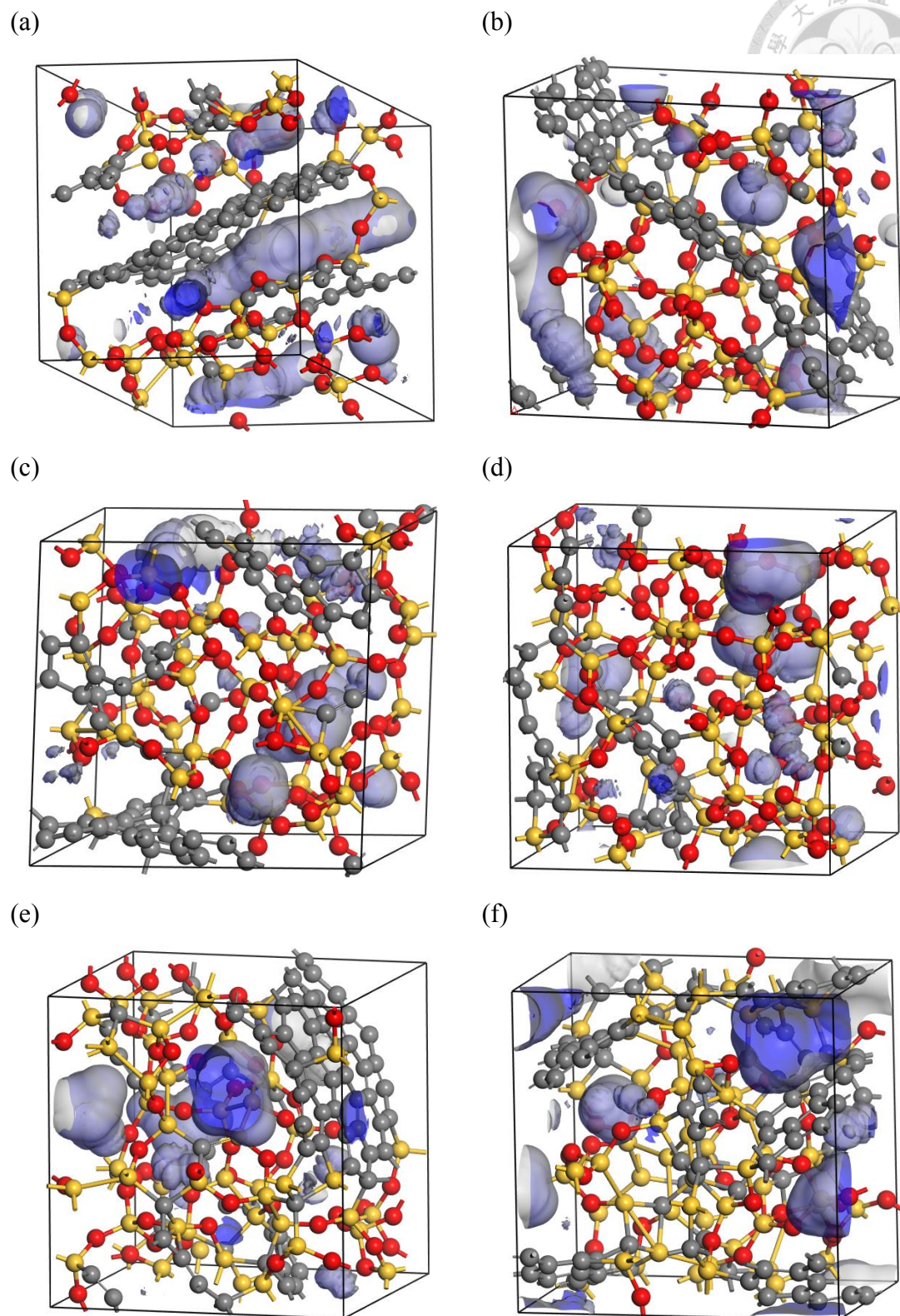


Figure 4.15 The microporous space in: (a)  $\text{SiC}_{3.3}\text{O}_{1.6}$ , (b)  $\text{SiC}_{2.2}\text{O}_{1.6}$ , (c)  $\text{SiC}_{1.65}\text{O}_{1.6}$ , (d)  $\text{SiC}_{0.8}\text{O}_{1.6}$ , (e)  $\text{SiC}_{1.65}\text{O}_{1.1}$ , (f)  $\text{SiC}_{1.65}\text{O}_{0.6}$ ,

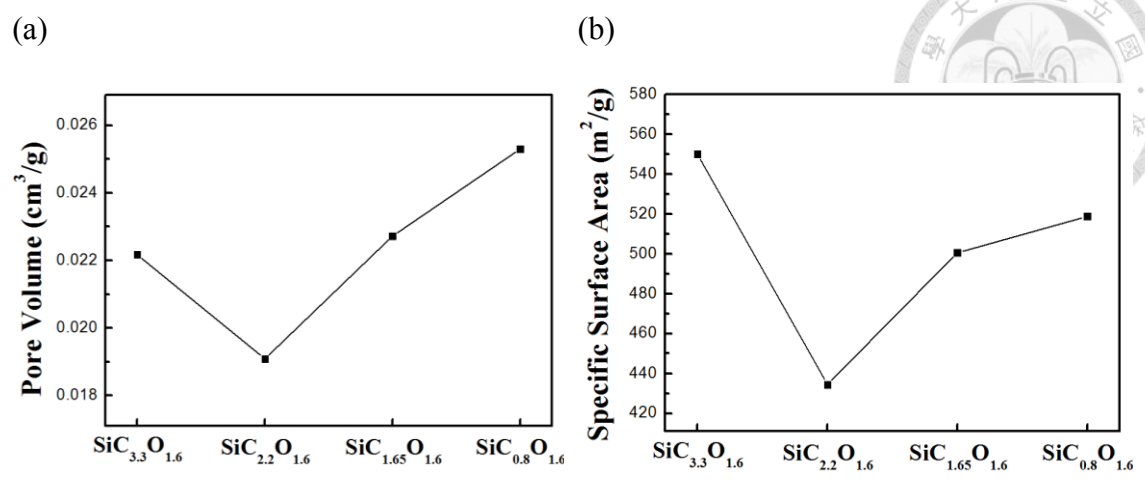


Figure 4.16 (a) pore volume and, (b) specific surface area of  $\text{SiC}_{3.3}\text{O}_{1.6}$ ,  $\text{SiC}_{2.2}\text{O}_{1.6}$ ,  $\text{SiC}_{1.65}\text{O}_{1.6}$  and  $\text{SiC}_{0.8}\text{O}_{1.6}$

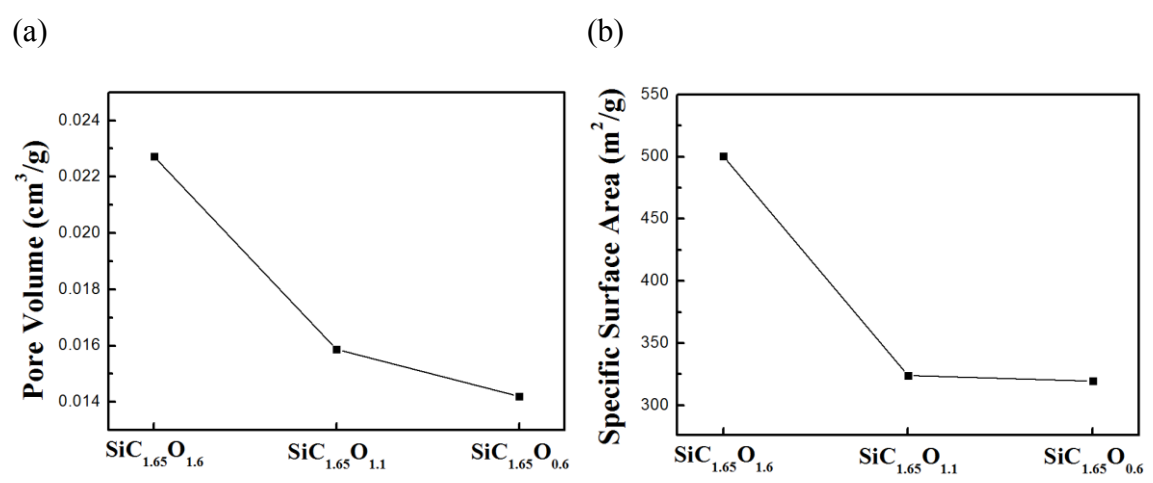


Figure 4.17 (a) pore volume and, (b) specific surface area of  $\text{SiC}_{1.65}\text{O}_{1.6}$ ,  $\text{SiC}_{1.65}\text{O}_{1.1}$  and  $\text{SiC}_{1.65}\text{O}_{0.6}$





### 4.3.5 Electronic structures of SiOC

In this section, we present the electronic structures of amorphous SiOC to discuss how the carbon and oxygen contents affect the band gap of SiOC glass phase in amorphous SiOC structures. The local density of state of  $\text{SiC}_{3.3}\text{O}_{1.6}$ ,  $\text{SiC}_{2.2}\text{O}_{1.6}$ ,  $\text{SiC}_{1.65}\text{O}_{1.6}$ ,  $\text{SiC}_{0.8}\text{O}_{1.6}$ ,  $\text{SiC}_{1.65}\text{O}_{1.1}$  and  $\text{SiC}_{1.65}\text{O}_{0.6}$  are shown in Figure 4.18 to Figure 4.23. The dashed lines refer to the edge of extended states in SiOC glass region, while the states between the dashed lines are localized states in SiOC glass phase and extended states in free carbon layer. To further verify the states between the gaps, we observe the charge distributions in the gap region via decomposed charge density calculations. The charge distributions between the gaps of  $\text{SiC}_{3.3}\text{O}_{1.6}$ ,  $\text{SiC}_{2.2}\text{O}_{1.6}$ ,  $\text{SiC}_{1.65}\text{O}_{1.6}$ ,  $\text{SiC}_{0.8}\text{O}_{1.6}$ ,  $\text{SiC}_{1.65}\text{O}_{1.1}$  and  $\text{SiC}_{1.65}\text{O}_{0.6}$  are shown in Figure 4.24 to Figure 4.29. It is confirmed that the states between the gaps of SiOC glass phase are either localized states in SiOC glass phase or extended states in free carbon phase.

The fraction of Si-C bond, fraction of Si-Si bond and the band gaps of  $\text{SiC}_{3.3}\text{O}_{1.6}$ ,  $\text{SiC}_{2.2}\text{O}_{1.6}$ ,  $\text{SiC}_{1.65}\text{O}_{1.6}$ ,  $\text{SiC}_{0.8}\text{O}_{1.6}$ ,  $\text{SiC}_{1.65}\text{O}_{1.1}$  and  $\text{SiC}_{1.65}\text{O}_{0.6}$  are listed in Table 4.2. As we can see in the table, the band gaps of all the SiOC glass phase in amorphous SiOCs are under 3.5 eV, which are much lower than the band gap of amorphous  $\text{SiO}_2$  (around 6 eV in DFT calculations). It indicates that adding carbon atoms into the SiOC glass phase effectively reduces the gaps by forming the Si-C states, whose band gap is around 1.4 eV. Furthermore, the band gaps of  $\text{SiC}_{3.3}\text{O}_{1.6}$ ,  $\text{SiC}_{2.2}\text{O}_{1.6}$ ,  $\text{SiC}_{1.65}\text{O}_{1.6}$  and  $\text{SiC}_{0.8}\text{O}_{1.6}$  are all close to 3.0 eV since there are few differences among the fraction of Si-C bond and Si-Si bond in the four concentrations. On the other hand, the decrease of oxygen concentration induces the rising fractions of Si-C bond and Si-Si bond in  $\text{SiC}_{1.65}\text{O}_{1.1}$  and  $\text{SiC}_{1.65}\text{O}_{0.6}$ , making the band gaps of the SiOC glass phase lower to 1.2 and 0.6 eV respectively.

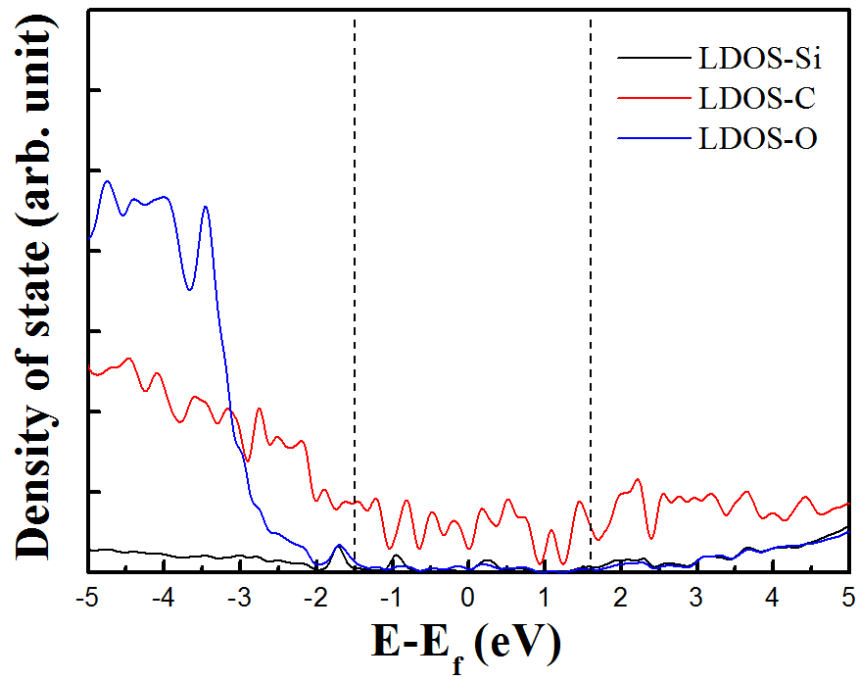


Figure 4.18 Local density of state of  $\text{SiC}_{3.3}\text{O}_{1.6}$

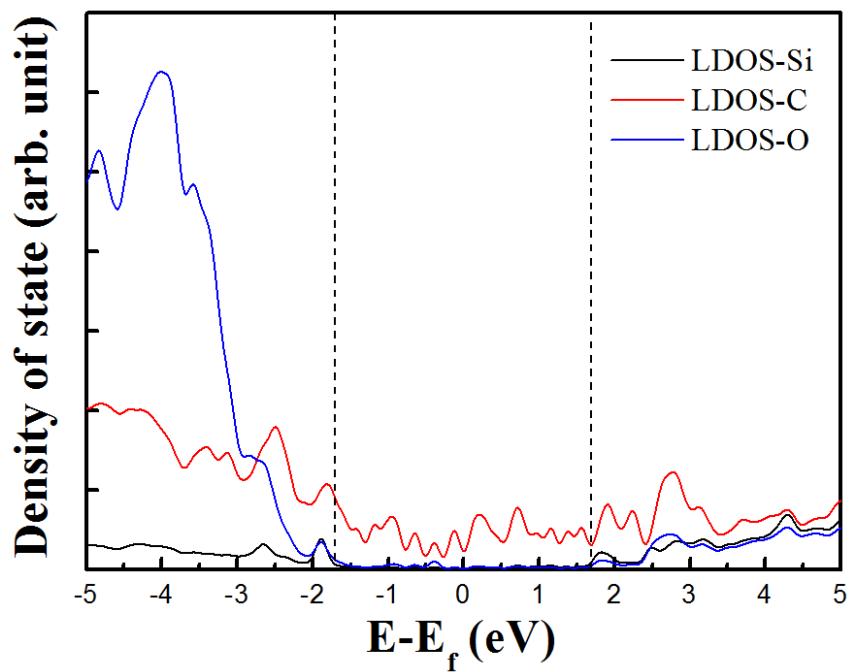


Figure 4.19 Local density of state of  $\text{SiC}_{2.2}\text{O}_{1.6}$

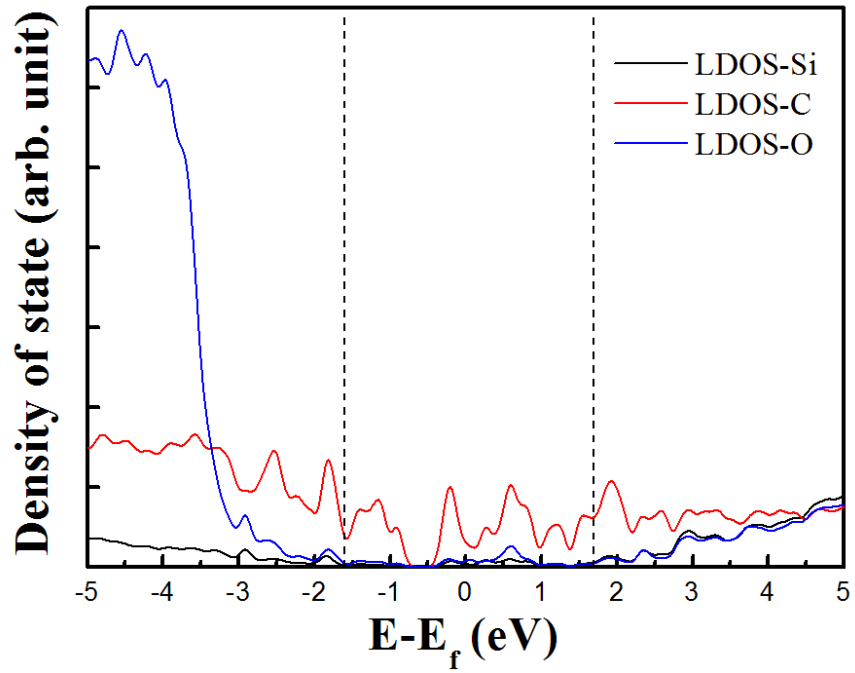
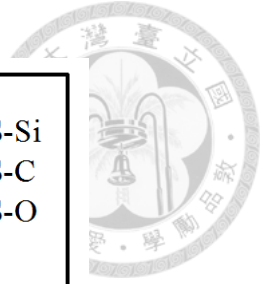


Figure 4.20 Local density of state of SiC<sub>1.65</sub>O<sub>1.6</sub>

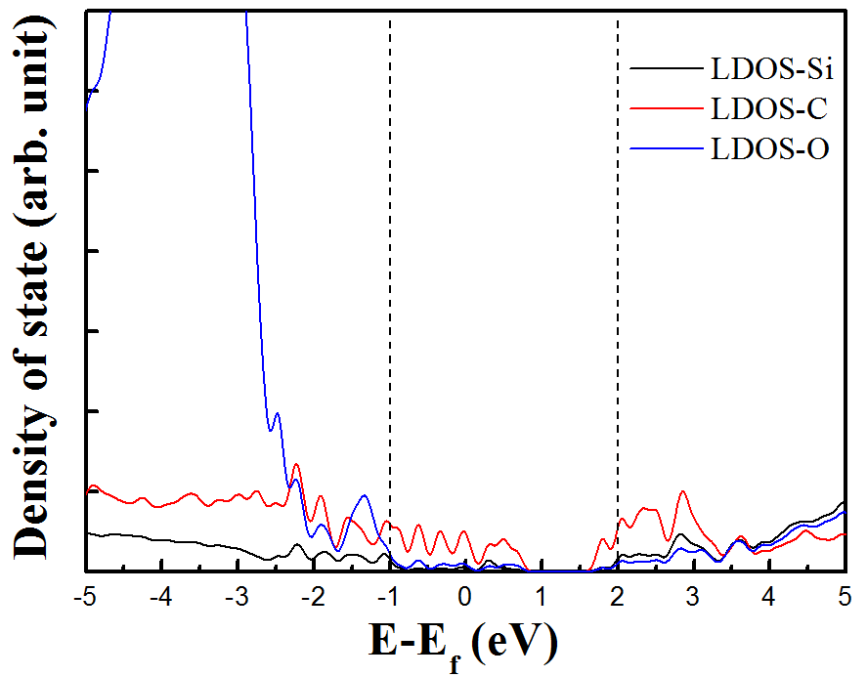


Figure 4.21 Local density of state of SiC<sub>0.8</sub>O<sub>1.6</sub>

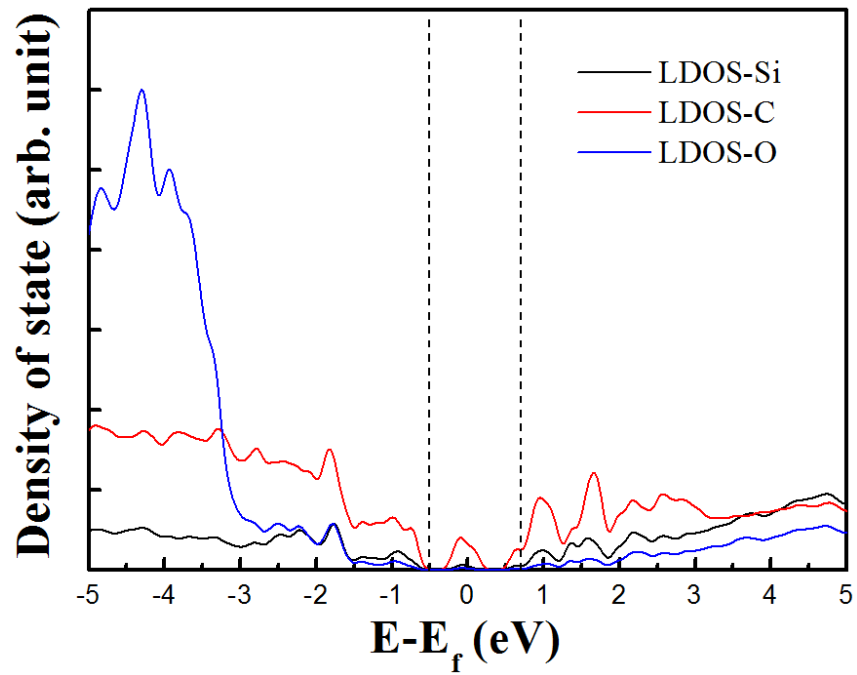


Figure 4.22 Local density of state of SiC<sub>1.65</sub>O<sub>1.1</sub>

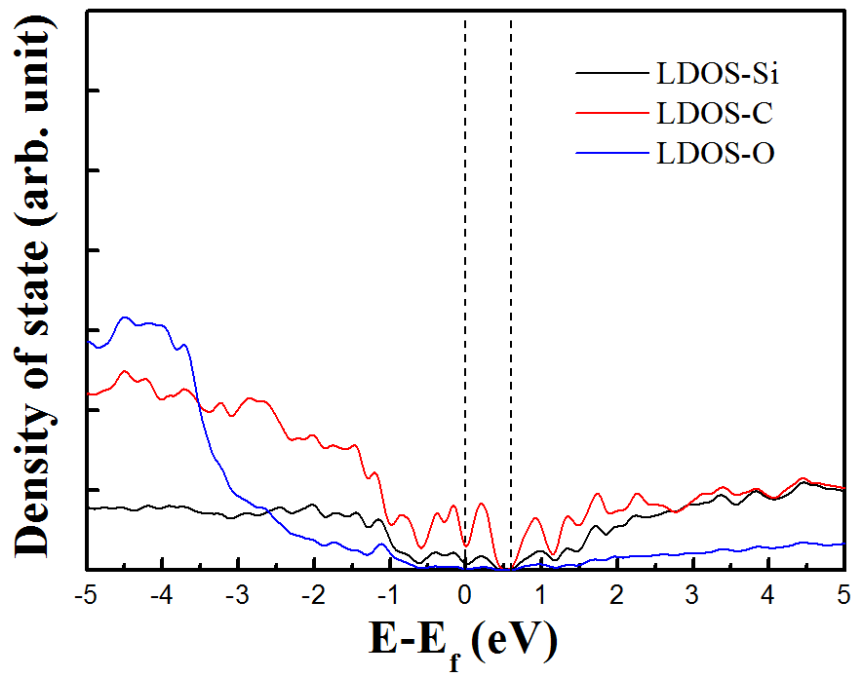
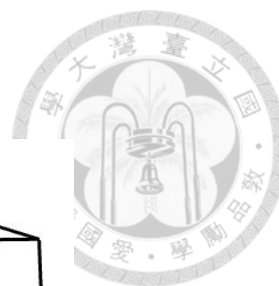
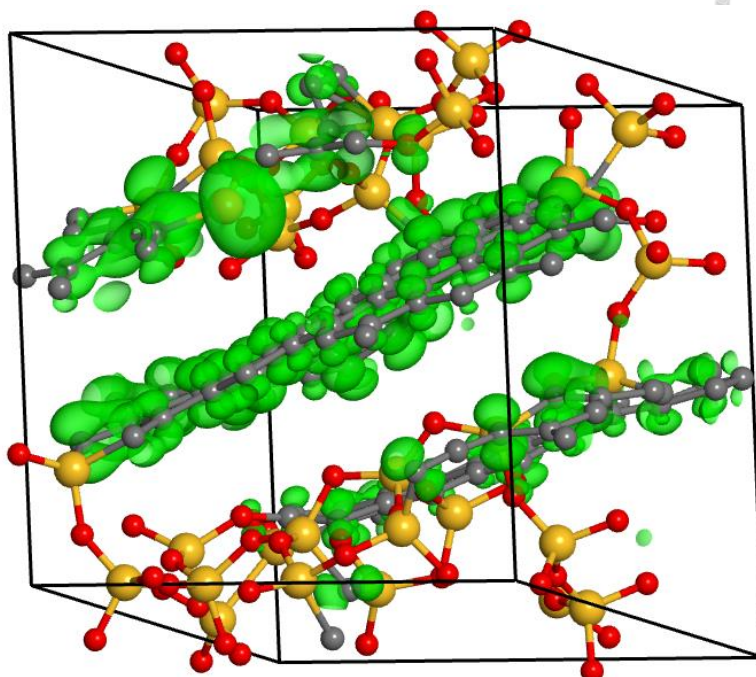


Figure 4.23 Local density of state of SiC<sub>1.65</sub>O<sub>0.6</sub>



(a)



(b)

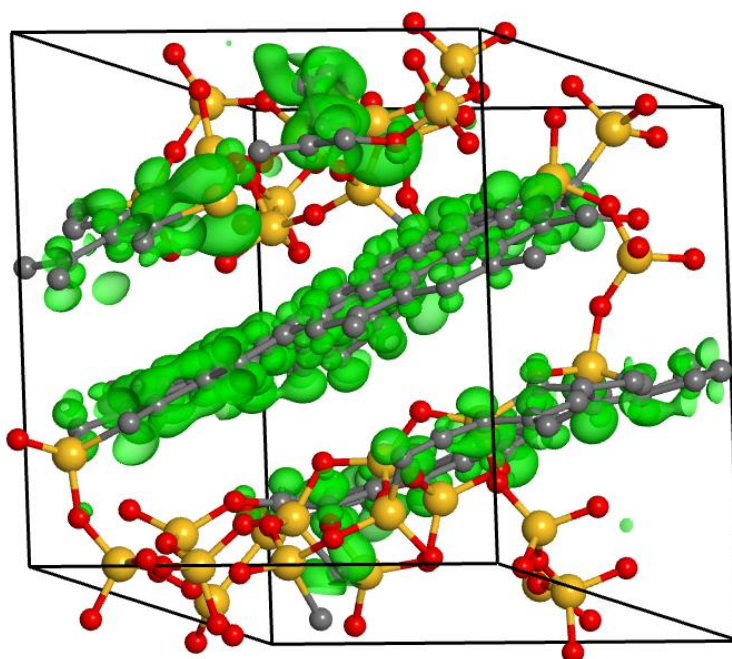
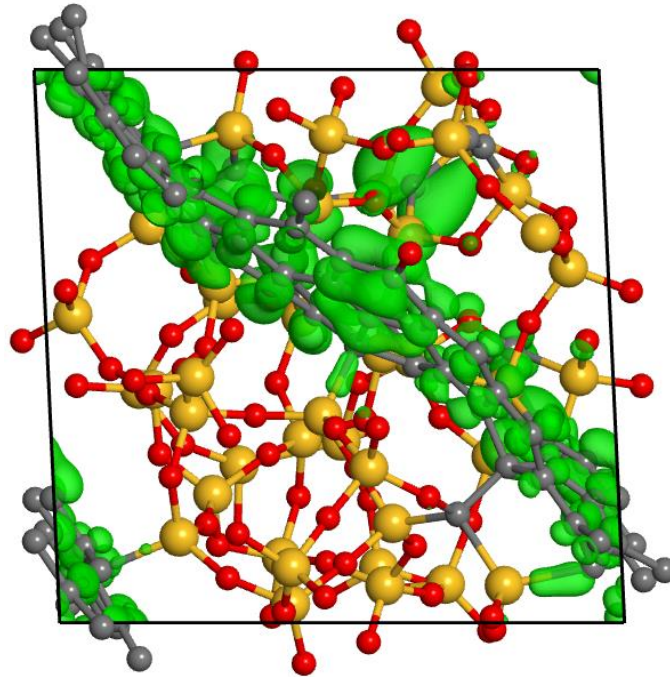


Figure 4.24 The charge distribution of  $\text{SiC}_{3.3}\text{O}_{1.6}$  in the range between: (a)  $E-E_f = -1.5 \sim 0$  eV, (b)  $E-E_f = 0 \sim 1.6$  eV



(a)



(b)

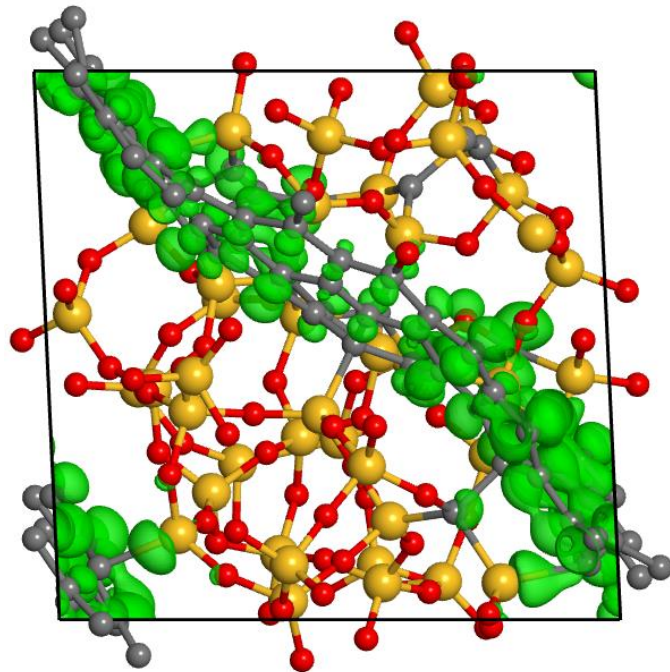
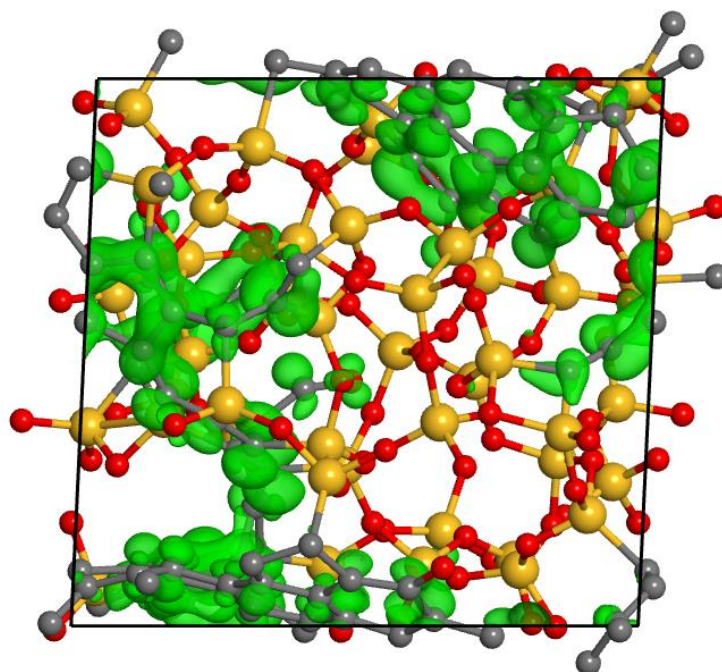


Figure 4.25 The charge distribution of SiC<sub>2.2</sub>O<sub>1.6</sub> in the range between: (a)  $E-E_f = -1.7 \sim 0$  eV, (b)  $E-E_f = 0 \sim 1.7$  eV



(a)



(b)

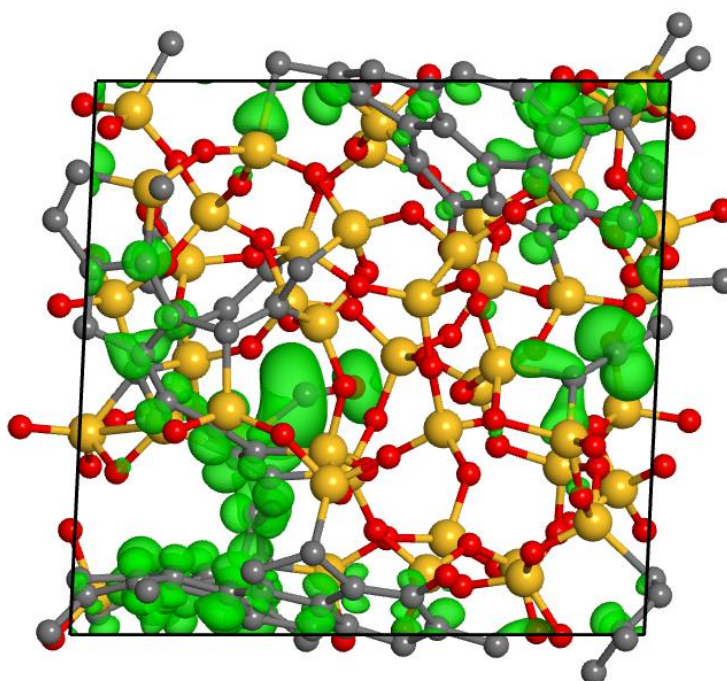
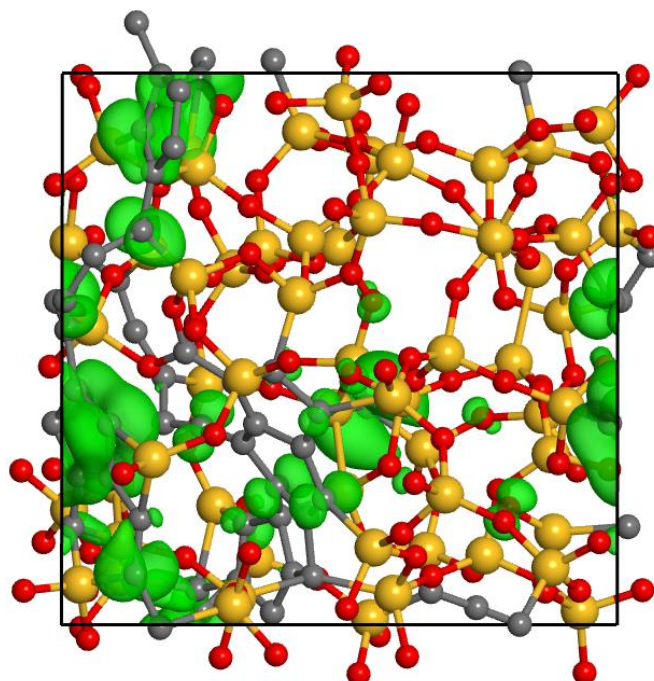


Figure 4.26 The charge distribution of SiC<sub>1.65</sub>O<sub>1.6</sub> in the range between: (a)  $E-E_f = -1.6 \sim 0$  eV, (b)  $E-E_f = 0 \sim 1.7$  eV



(a)



(b)

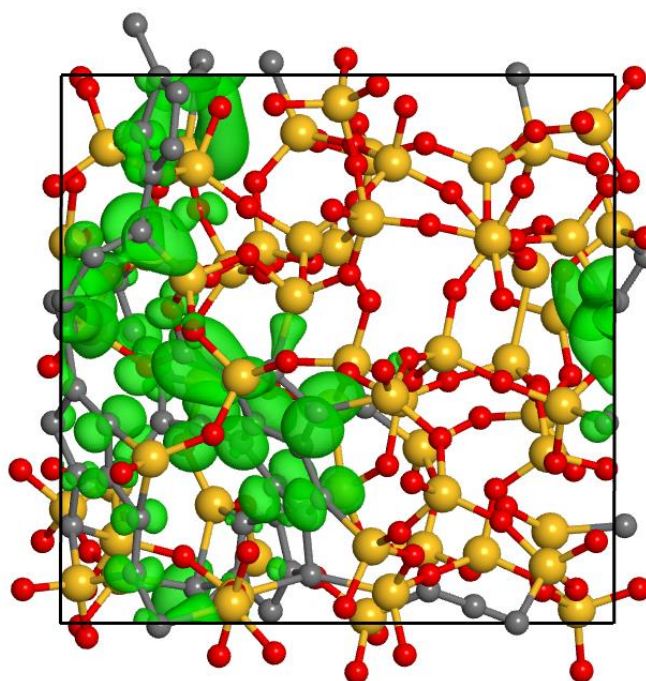
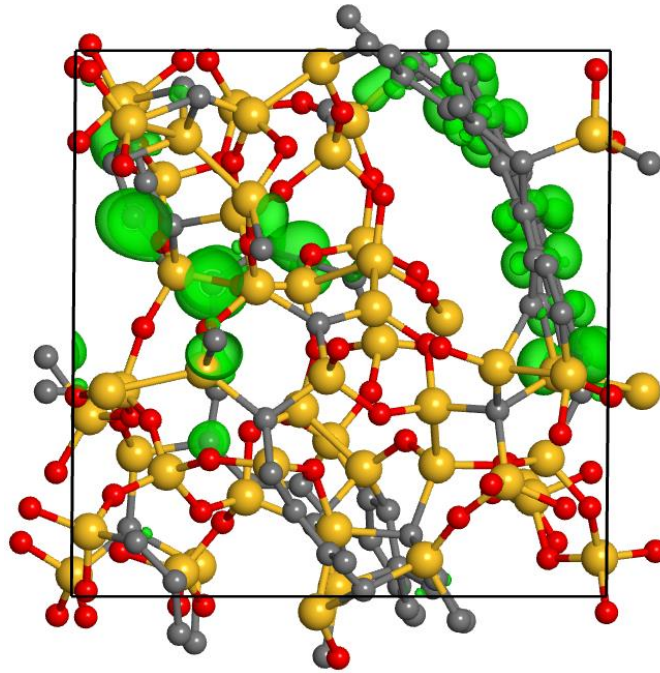


Figure 4.27 The charge distribution of SiC<sub>0.8</sub>O<sub>1.6</sub> in the range between: (a)  $E-E_f = -1.0 \sim 0$  eV, (b)  $E-E_f = 0 \sim 2.0$  eV





(a)



(b)

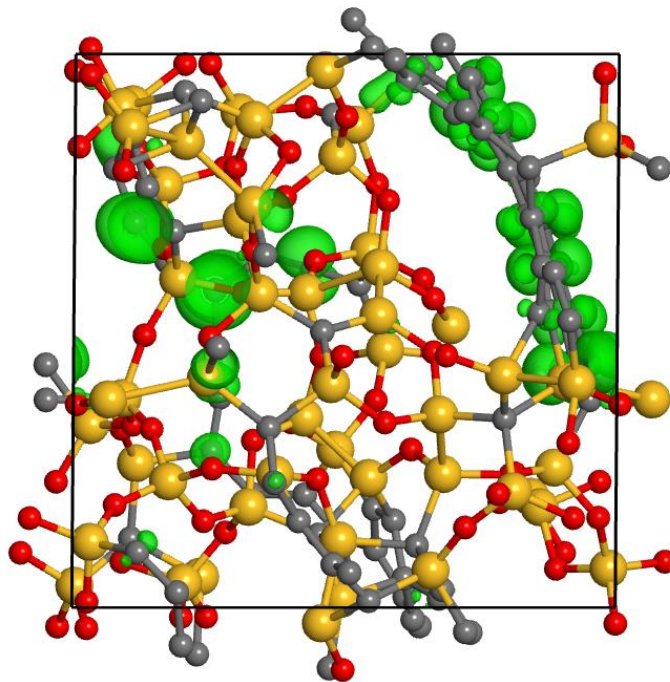


Figure 4.28 The charge distribution of SiC<sub>1.65</sub>O<sub>1.1</sub> in the range between: (a)  $E-E_f = -0.5 \sim 0$  eV, (b)  $E-E_f = 0 \sim 0.7$  eV

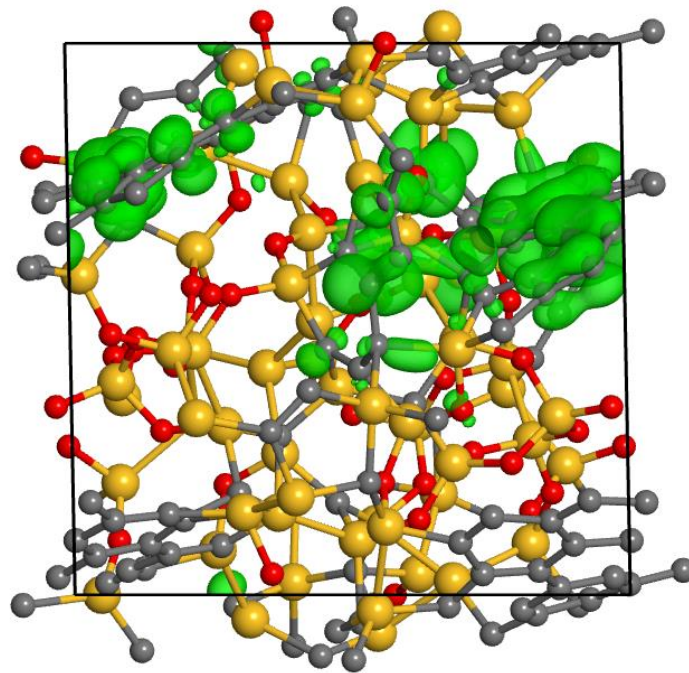


Figure 4.29 The charge distribution of  $\text{SiC}_{1.65}\text{O}_{1.1}$  in the range between  $E-E_f = 0 \sim 0.6$  eV

Table 4.2 Fraction of Si-C bond, fraction of Si-Si bond and band gap of amorphous

SiOCs			
	$\frac{\# \text{ of Si - C}}{\# \text{ of Si}}$	$\frac{\# \text{ of Si - Si}}{\# \text{ of Si}}$	Band gap (eV)
$\text{SiC}_{3.3}\text{O}_{1.6}$	0.79	0.09	3.2
$\text{SiC}_{2.2}\text{O}_{1.6}$	0.80	0.05	3.4
$\text{SiC}_{1.65}\text{O}_{1.6}$	0.78	0.07	3.3
$\text{SiC}_{0.8}\text{O}_{1.6}$	0.67	0.06	3.0
$\text{SiC}_{1.65}\text{O}_{1.1}$	1.27	0.30	1.2
$\text{SiC}_{1.65}\text{O}_{0.6}$	1.78	0.57	0.6



## 4.4 Summary

In this chapter, we construct the amorphous SiOC structures in six different concentrations, which are  $\text{SiC}_{3.3}\text{O}_{1.6}$ ,  $\text{SiC}_{2.2}\text{O}_{1.6}$ ,  $\text{SiC}_{1.65}\text{O}_{1.6}$ ,  $\text{SiC}_{0.8}\text{O}_{1.6}$ ,  $\text{SiC}_{1.65}\text{O}_{1.1}$  and  $\text{SiC}_{1.65}\text{O}_{0.6}$ , via *ab initio* melt-and-quench MD. For all concentrations above, free carbon phase as well as SiOC glass phase are clearly observed.

For free carbon phase, the results suggest that the area of free carbon phase will gradually decrease as the lowering of carbon concentrations. Besides, decreasing the content of carbon and oxygen both result in the lowering of the proportion of carbon atoms in free carbon phase. Furthermore, the increase of carbon concentration as well as the decrease of oxygen concentration will induce the rise of the fraction of  $\text{SiC}_4$  and  $\text{SiC}_3\text{O}$  tetrahedra and the drop in the fraction of  $\text{SiCO}_3$  and  $\text{SiO}_4$  tetrahedra. Because of the dense nature of tetrahedral units with higher carbon content and loose nature of tetrahedral units with lower carbon content, the increase of carbon concentration as well as the decrease of oxygen atom will also induce the drop in PV and SSA in amorphous SiOC.

In terms of the electronic structures of amorphous SiOC, the addition of carbon atoms into the SiOC glass phase effectively reduce the band gap of the SiOC glass region to under 3.5 eV by forming the Si-C states, whose band gap is around 1.4 eV. On the other hand, the decrease of oxygen concentration induces the rising fraction of Si-C bond and Si-Si bond in  $\text{SiC}_{1.65}\text{O}_{1.1}$  and  $\text{SiC}_{1.65}\text{O}_{0.6}$ , lowering the band gap of the SiOC glass phase to 1.2 and 0.6 eV respectively.

# Chapter 5 Lithiation Mechanism of Amorphous Silicon Oxycarbide



## 5.1 Introduction

As a potential candidate for next generation anode in LIBs, amorphous SiOCs deliver reversible capacities of around 600 mAh/g with an irreversible capacity loss during the first charging/discharging cycle. However, the exact lithiation mechanism of SiOCs is still controversial. Fukui et al. [22] synthesized a SiOC sample of  $\text{SiC}_{7.78}\text{O}_{0.51}$ , offering the first lithiation capacity of 867 mAh/g and the first delithiation one of 608 mAh/g as shown in Figure 5.1. They suggested that the major charge capacity of SiOC ceramics came from the free carbon phase, and the lithium storage site could be interstitial spaces or edges of graphene layers. On contrary, Liu et al. [36] considered that SiOC glasses phase served as the major lithiation site.

For theoretical studies, Liao et al. [38] attributed the high specific capacities to the formation of  $\text{Li}_x\text{O}$  and  $\text{Li}_y\text{Si}$  composites in lithiated SiOC, as shown in Figure 5.2, and suggested that the carbon atoms did not attract lithium but form a stable C–C domain to maintain the configuration of the lithiated system. Sun et al. [11] considered the two-step lithiation proceeds by the absorption of Li at the nanovoid sites, followed by the chemical interactions of Li with the  $\text{SiO}_x\text{C}_{4-x}$  tetrahedral units and the C phase.

In this chapter, we conducted the lithiation calculations on four different SiOC concentrations, which are  $\text{SiC}_{2.2}\text{O}_{1.6}$ ,  $\text{SiC}_{1.65}\text{O}_{1.6}$ ,  $\text{SiC}_{0.8}\text{O}_{1.6}$  and  $\text{SiC}_{1.65}\text{O}_{0.6}$ , to clarify the lithiation mechanism of amorphous SiOCs. Furthermore, we also tried to figure out the key factors that affect the total capacity and reversibility of amorphous SiOCs.

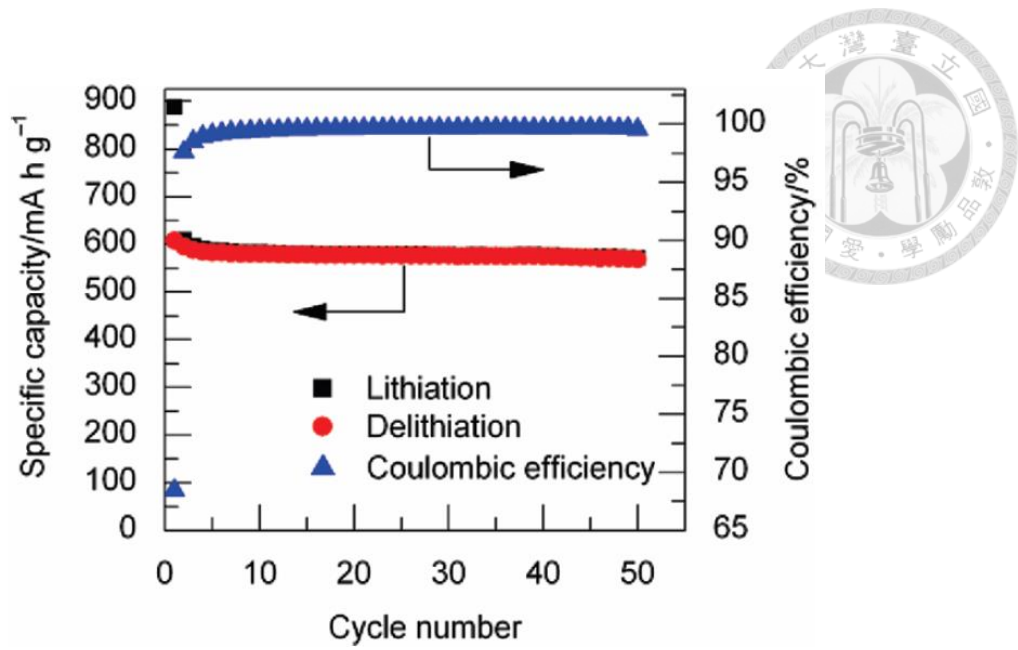


Figure 5.1 Lithiation/delithiation capacity and Coulombic efficiency of SiC<sub>7.78</sub>O<sub>0.51</sub> [22]

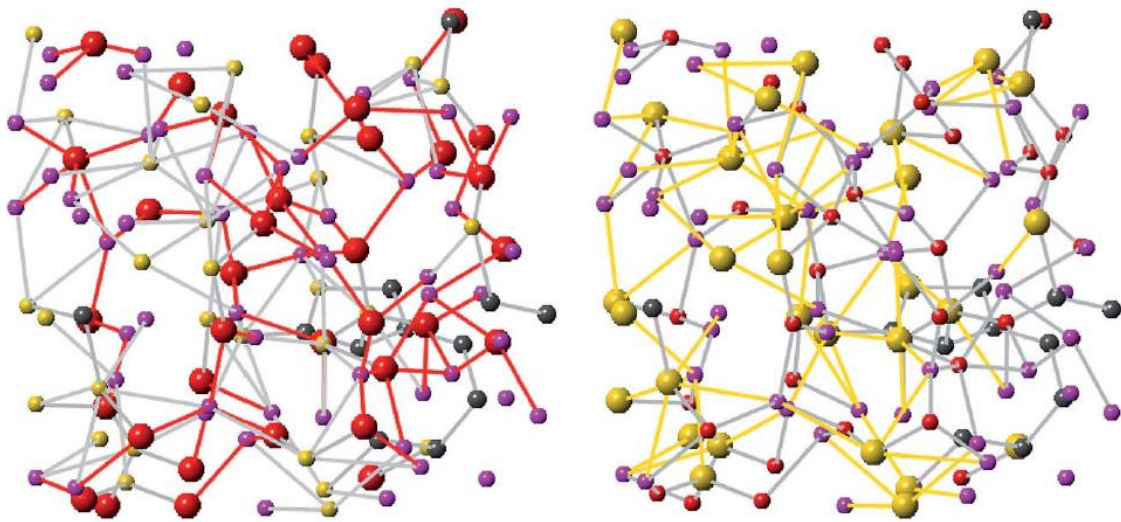


Figure 5.2 Formation of Li<sub>x</sub>O and Li<sub>y</sub>Si in Li<sub>2</sub>SiC<sub>2.5</sub>O<sub>6.5</sub> [38]



## 5.2 Computational details

All atomic structures, energetics, and electronic properties reported here without farther mention were calculated based on the density functional theory (DFT) within the generalized gradient approximation (GGA) with the parametrization of Perdew–Burke–Ernzerhof (PBE) for the exchange-correlation functional as implemented in the well-established Vienna ab initio simulation package (VASP). The valence electron wave functions were expanded in plane-wave basis sets and the projector augmented wave (PAW) method was used to describe the core-electron interactions. The plane-wave cut-off energy was set to be 500 eV for both the geometric optimization and the electronic property calculations. The Brillouin zone samplings were performed with a  $2 \times 2 \times 2$  k-point grid in the Monkhorst-Pack scheme for the geometry optimization and with an increased k-point mesh up to  $5 \times 5 \times 5$  for the electronic properties calculation. During the geometry optimization, all atoms in the supercell were fully relaxed with the conjugated gradient method until the residual forces acting on the constituent atoms become less than 0.05 eV/Å.

To simulate the lithiation process, in each step, five Li atoms were put into the voids in the structures, followed by MD simulations at 1000K for 5ps. The three configurations with the lowest energy were picked during the period. The structures were then fully relaxed and the energies for the systems were obtained to calculate the formation energy. The formation energies per Si atom ( $E_f$ ) is given by

$$E_f = E_{Li_xSiO_aC_b} - (xE_{Li} + E_{SiO_aC_b}) \quad (\text{eq. 5-1})$$

where  $E_{Li_xSiO_aC_b}$  and  $E_{SiO_aC_b}$  are the total energies per Si atom of lithiated SiOC and pristine SiOC systems and  $E_{Li}$  is the per-atom energy of bcc-Li. The configuration with the lowest formation energy in each step was used for further lithium insertion. The

voltage is calculated by

$$V = -\frac{dE_f(x)}{dx}$$



When the structures are fully lithiated, the formation energies will approach a minimum and the voltage will drop to a negative value, suggesting that the further insertion of Li is thermodynamically unfavorable.

## 5.3 Results and discussion

### 5.3.1 First lithiation stage of SiOC

The lithiation process can be briefly divided into two stages. In the first lithiation stage, the Li ions were found to be located near the free carbon phase or at the interface between the free carbon phase and SiOC glass phase. As shown in Figure 5.3 to Figure 5.6, there were 21, 21, 6 and 21 Li in the first stage lithiation of  $\text{SiC}_{2.2}\text{O}_{1.6}$ ,  $\text{SiC}_{1.65}\text{O}_{1.6}$ ,  $\text{SiC}_{0.8}\text{O}_{1.6}$  and  $\text{SiC}_{1.65}\text{O}_{0.6}$  respectively.

The local density of state of the first stage lithiated SiOCs are shown in Figure 5.7. By integrating the total density of state of the first stage lithiated SiOCs from the lowest level to the level which made the integral the same as the numbers of electrons that pristine SiOCs had, we could obtain the relative relationship between the fermi level of pristine structures and of the lithiated structures. As shown in Figure 5.7, during the first lithiation stage, the transfer of electrons from Li let fermi level shift for 1.73, 1.72, 0.48 and 1.30 eV in  $\text{SiC}_{2.2}\text{O}_{1.6}$ ,  $\text{SiC}_{1.65}\text{O}_{1.6}$ ,  $\text{SiC}_{0.8}\text{O}_{1.6}$  and  $\text{SiC}_{1.65}\text{O}_{0.6}$  respectively. In the region between the fermi level of pristine structures and of the lithiated structures, the number of the states of carbon atoms is obviously more than that of silicon and oxygen atoms, indicating that the carbon atoms are the major electron receiver in the first lithiation stage.

On the other hand, the Li ions were absorbed on the oxygen atoms at the surface of SiOC glass phase.

To further verify the states that gained the electrons from Li, we observe the charge distributions between the fermi level of pristine structures and of the lithiated structures via decomposed charge density calculations, which are shown in Figure 5.8 to Figure 5.11. In all the four concentrations, the states fell mainly on the carbon atoms in free carbon phase and secondarily on defect sites, Si-C bonds and Si-Si bonds in SiOC glass phase, again suggesting that the carbon atoms are the major electron receiver in the first lithiation stage.

By integrating the local density of states of Si, O and C atoms in the range between the fermi level of pristine structures and of the lithiated structures, we obtained the charge gain on Si, O and C atoms in each step during the first lithiation stage of  $\text{SiC}_{2.2}\text{O}_{1.6}$ ,  $\text{SiC}_{1.65}\text{O}_{1.6}$ ,  $\text{SiC}_{0.8}\text{O}_{1.6}$  and  $\text{SiC}_{1.65}\text{O}_{0.6}$  as shown in Figure 5.12. It was clear that the charge gain on carbon atoms was far more than the charge gain on silicon and oxygen atoms for all the four concentrations in the first stage lithiation.



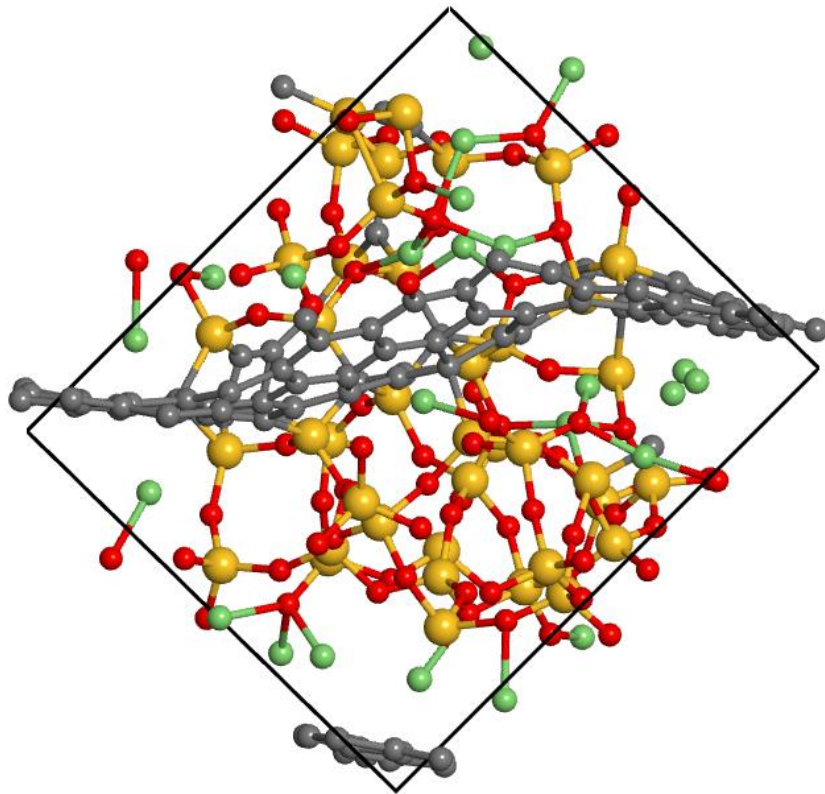


Figure 5.3 Structure of the first stage lithiated  $\text{SiC}_{2.2}\text{O}_{1.6}$  with 21 Li

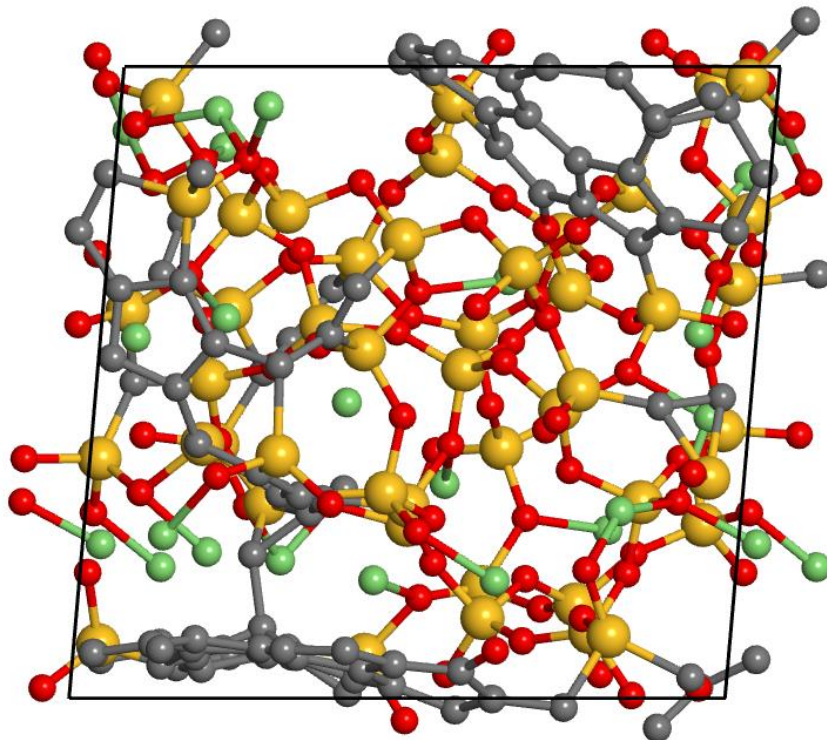


Figure 5.4 Structure of the first stage lithiated  $\text{SiC}_{1.65}\text{O}_{1.6}$  with 21 Li

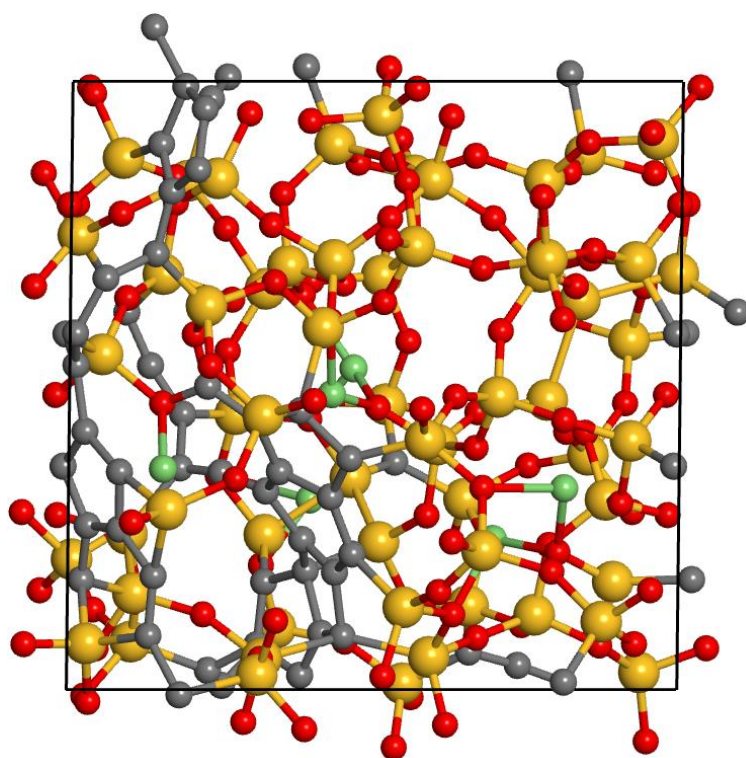


Figure 5.5 Structure of the first stage lithiated SiC<sub>0.8</sub>O<sub>1.6</sub> with 6 Li

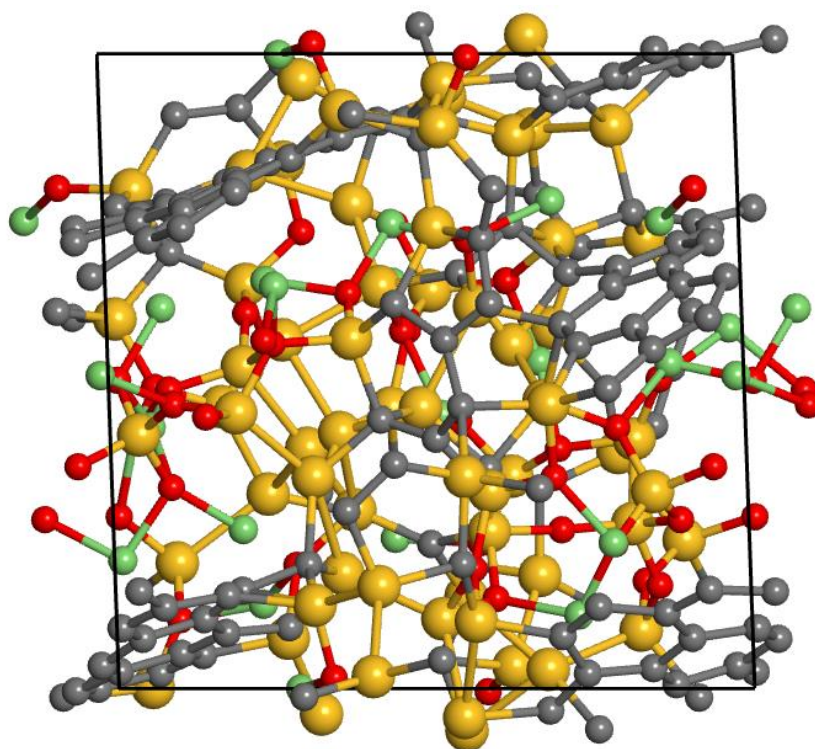


Figure 5.6 Structure of the first stage lithiated SiC<sub>1.65</sub>O<sub>0.6</sub> with 21 Li

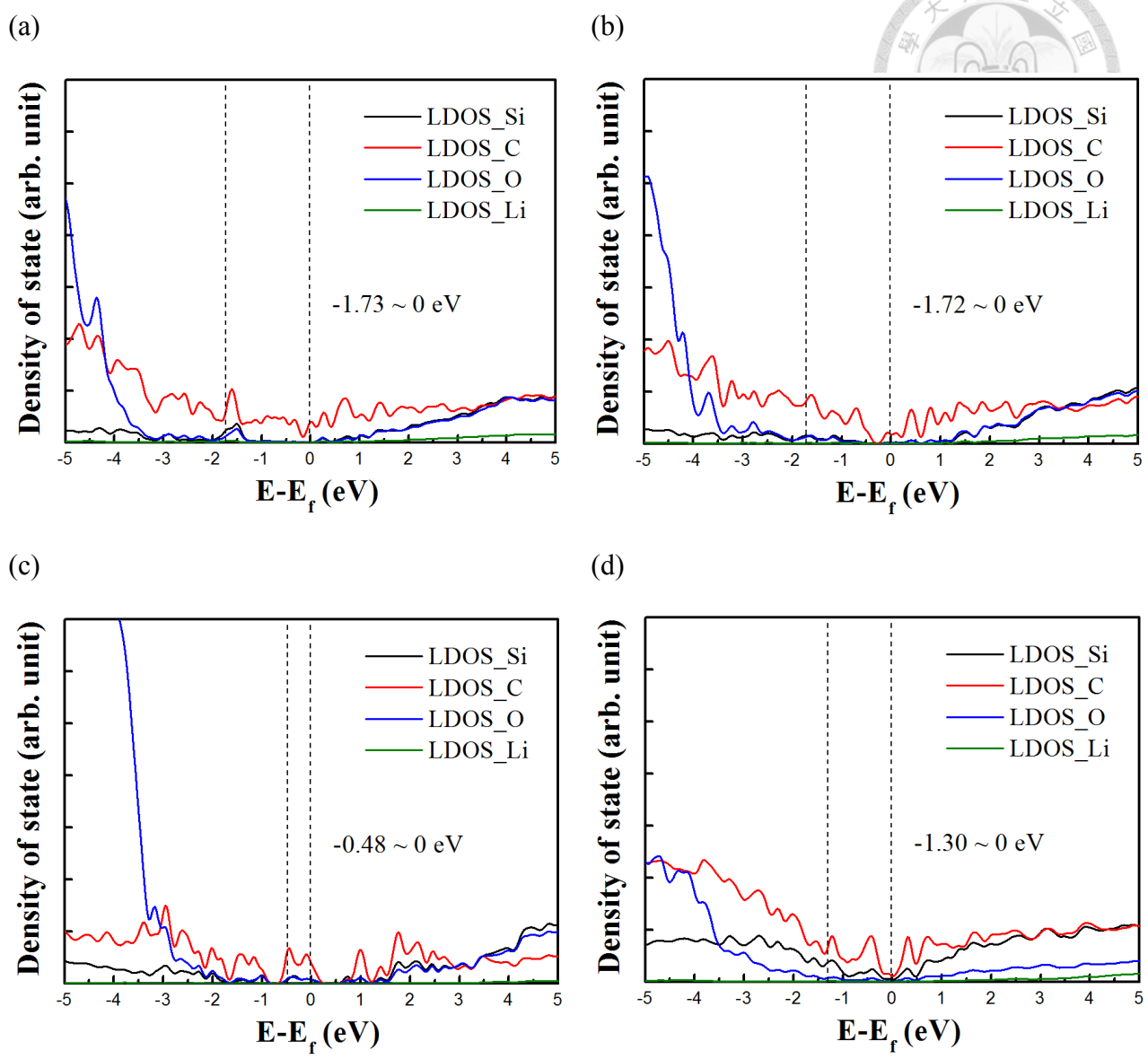


Figure 5.7 Local density of state of the first stage lithiated SiOCs: (a)  $\text{SiC}_{2.2}\text{O}_{1.6} + 21\text{Li}$ ,

(b)  $\text{SiC}_{1.65}\text{O}_{1.6} + 21\text{Li}$ , (c)  $\text{SiC}_{0.8}\text{O}_{1.6} + 6\text{Li}$ , (d)  $\text{SiC}_{1.65}\text{O}_{0.6} + 21\text{Li}$

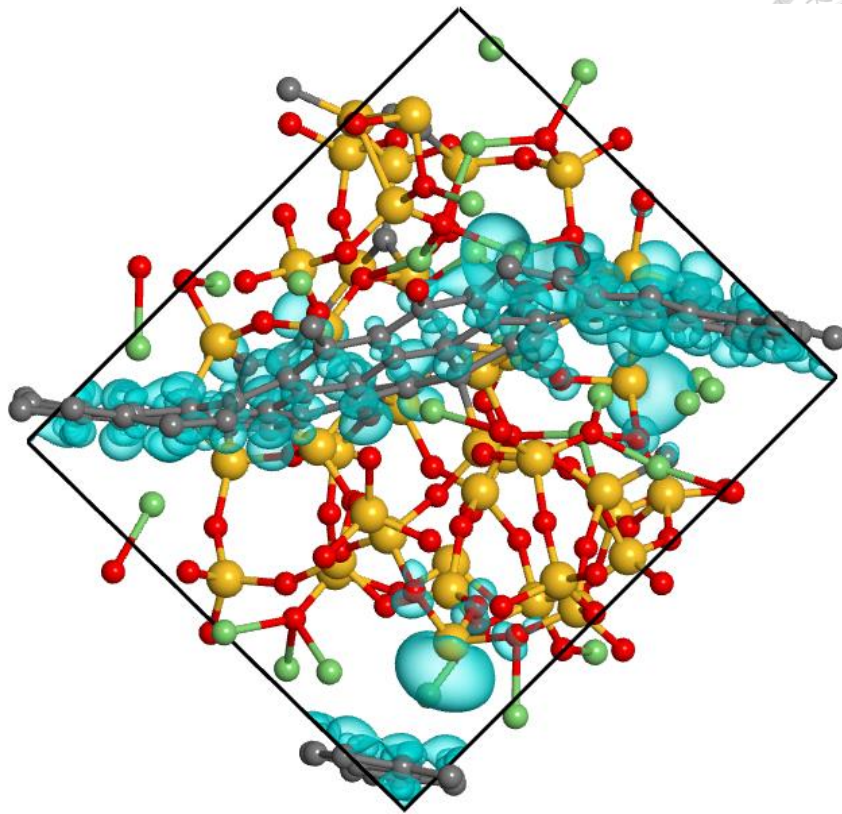


Figure 5.8 Charge gain in the first stage lithiated  $\text{SiC}_{2.2}\text{O}_{1.6}$  with 21 Li

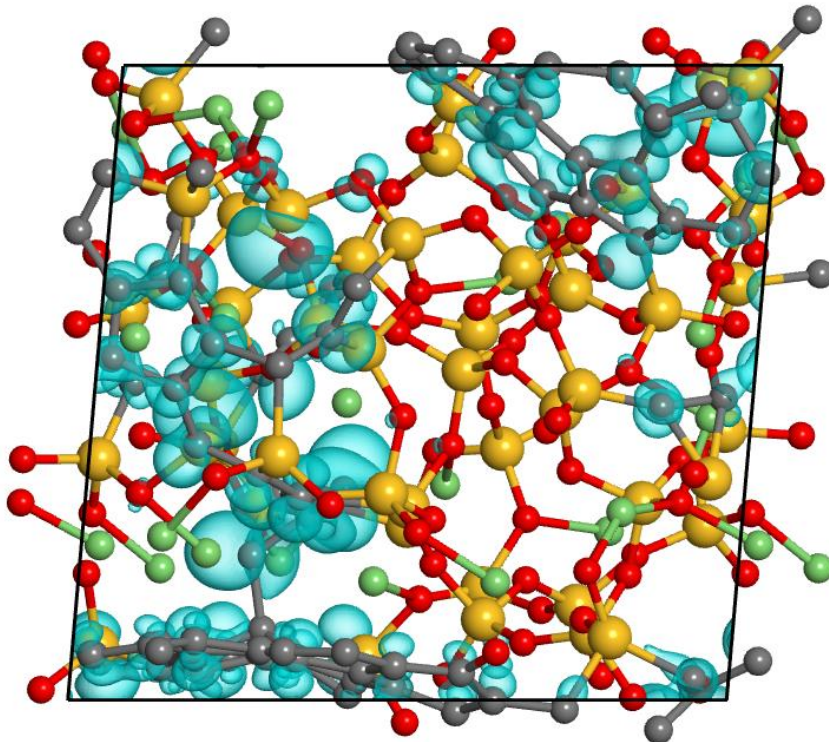


Figure 5.9 Charge gain in the first stage lithiated  $\text{SiC}_{1.65}\text{O}_{1.6}$  with 21 Li

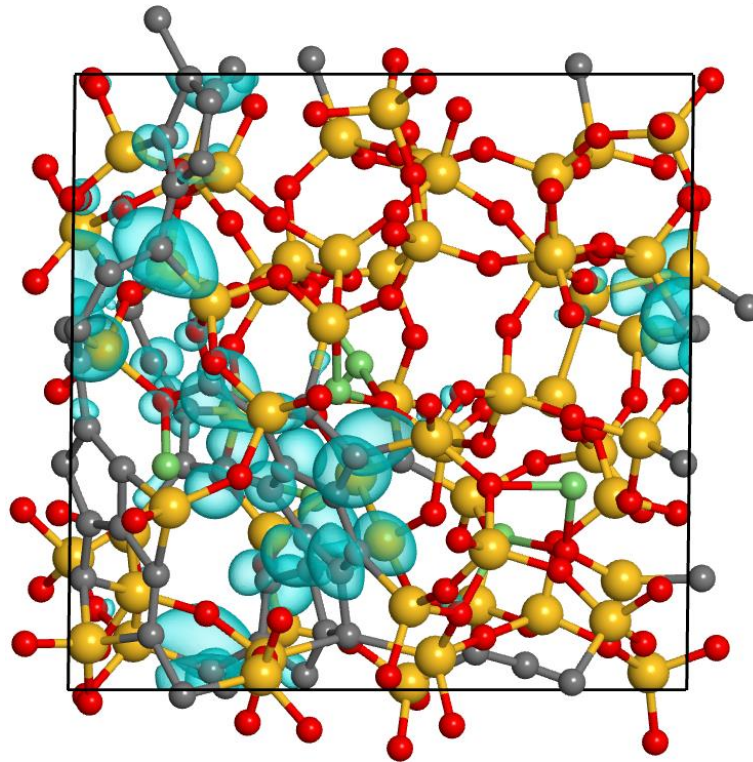


Figure 5.10 Charge gain in the first stage lithiated SiC<sub>0.8</sub>O<sub>1.6</sub> with 6 Li

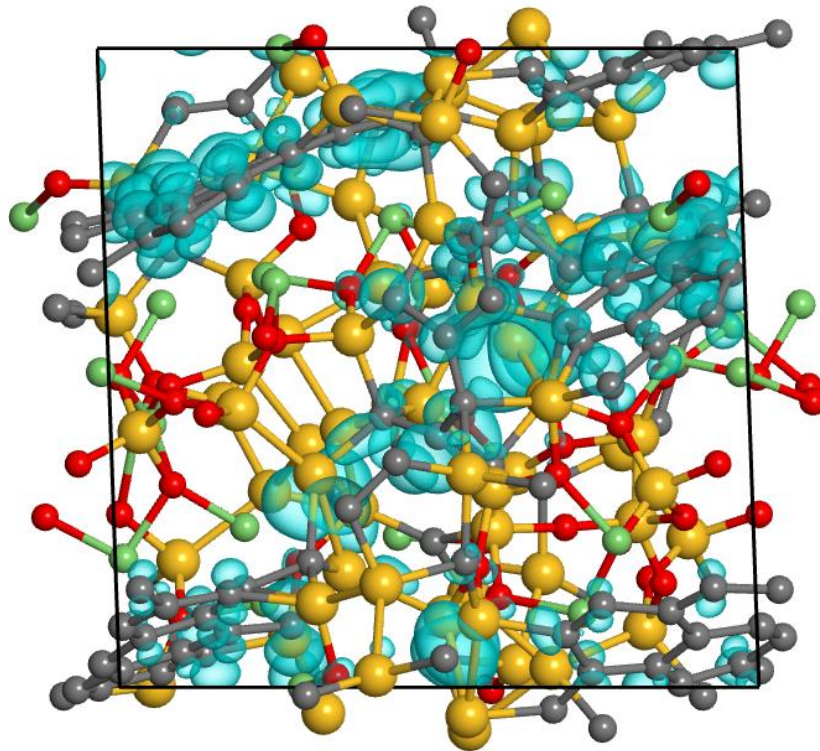


Figure 5.11 Charge gain in the first stage lithiated SiC<sub>1.65</sub>O<sub>0.6</sub> with 21 Li

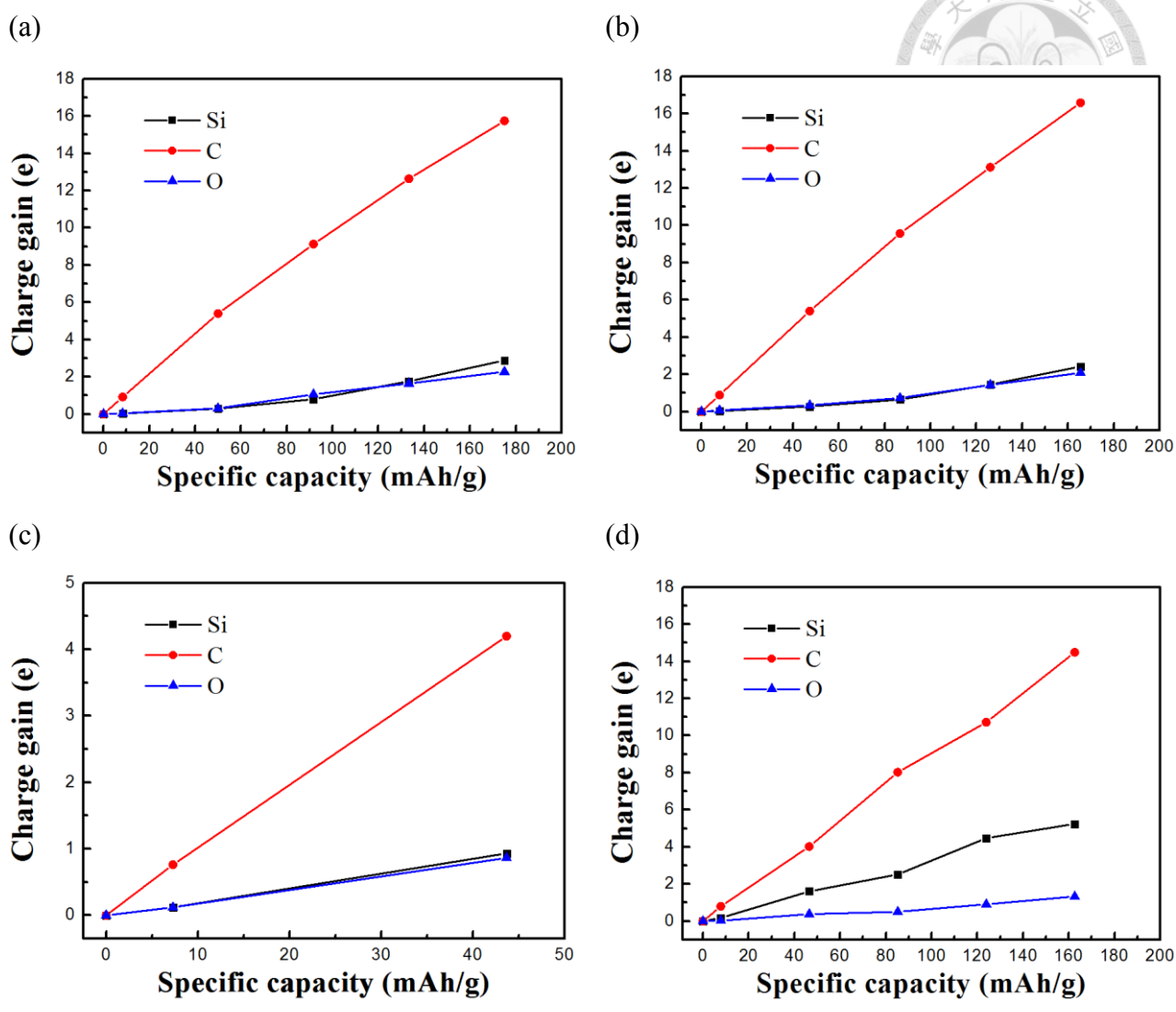
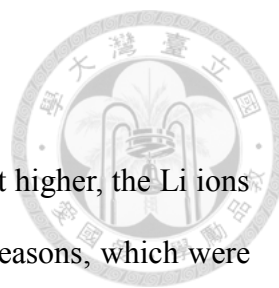


Figure 5.12 Distribution of charge gain of the first stage lithiated SiOCs: (a)  $\text{SiC}_{2.2}\text{O}_{1.6} + 21\text{Li}$ , (b)  $\text{SiC}_{1.65}\text{O}_{1.6} + 21\text{Li}$ , (c)  $\text{SiC}_{0.8}\text{O}_{1.6} + 6\text{Li}$ , (d)  $\text{SiC}_{1.65}\text{O}_{0.6} + 21\text{Li}$



### 5.3.2 Second lithiation stage of SiOC

In the second lithiation stage, as the lithium concentrations went higher, the Li ions began to interact with SiOC glasses. It could be attributed to three reasons, which were the stress accumulated in the first stage lithiation, the shift of fermi level of the systems and the effect of electric field at the interface between free carbon and SiOC glass phase.

First, the Li ions were absorbed on the oxygen atoms in the first lithiation stage. The coulombic interactions between Li ions and O atoms, which slightly distorted the Si-O-Si angles, induced the stress on the Si-O bonds in SiOC glass phase. The formation of strained bonds lowered several anti-bonding state of Si-O bonds, which thus made the electrons from Li more easily to transfer to the anti-bonding state of Si-O, resulting in the energetically favorable interaction between Li and SiOC glass.

Secondly, as the lithium concentration got higher and higher, the electrons from Li gradually filled the states that were originally unoccupied in the pristine SiOC structures, making the fermi level of the systems move to the higher states. The more Li ions were in the amorphous SiOCs, the closer the fermi level of the systems was to the conduction band minimum of the SiOC glass phase, which were Si-O anti-bonding states, allowing the electrons from Li to transfer to SiOC glass phase with less energy cost.

Third, the electrons accumulated on the carbon atoms in free carbon phase as well as the Li ions absorbed on the oxygen atoms from the surface of SiOC glass phase in the first stage lithiation generated an electric field at the interface between free carbon and SiOC glass phase as shown in Figure 5.13. The electric field at the interface region made the electrons be prone to move to the SiOC glass region. Therefore, the Li ions tends to interact with the SiOC glasses in the second stage lithiation.

The insertion of Li in amorphous SiO<sub>2</sub> is an energetically unfavorable reaction, which had been tested ourselves and also proposed by Kroll <sup>[43]</sup>. Nevertheless, with the

aid of the above effects as well as the carbon atoms in SiOC glass phase, the insertion of Li in SiOC glass becomes an energetically favorable reaction instead. Besides, during the second stage lithiation of amorphous SiOCs, we observed that not only the number of Li ions in the SiOC glass phase was increasing, but also the number of Li ions near the free carbon phase was slowly growing. It indicated that the free carbon was keeping receiving electrons from Li during the whole lithiation process.

Finally, the fully lithiated structures of  $\text{SiC}_{2.2}\text{O}_{1.6}$ ,  $\text{SiC}_{1.65}\text{O}_{1.6}$ ,  $\text{SiC}_{0.8}\text{O}_{1.6}$  and  $\text{SiC}_{1.65}\text{O}_{0.6}$  are shown in Figure 5.14 to Figure 5.17. It can be seen that the free carbon phase still remained complete, suggesting the function of stabilizing the whole systems of it. On the other hand, the break of Si-O bonds and the formation of Li-O as well as Si-Si bonds were observed in the SiOC glass region during the lithiation process.

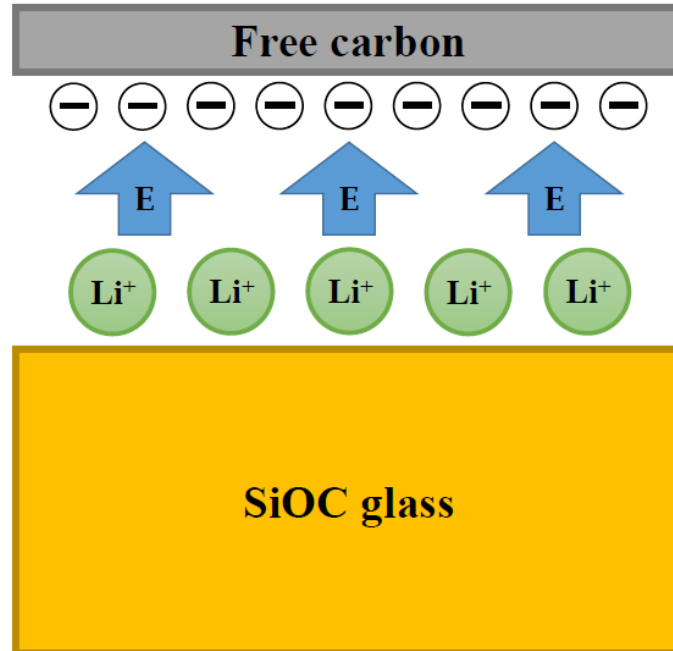


Figure 5.13 Schematic representation of electric field generated after the first stage lithiation in amorphous SiOCs



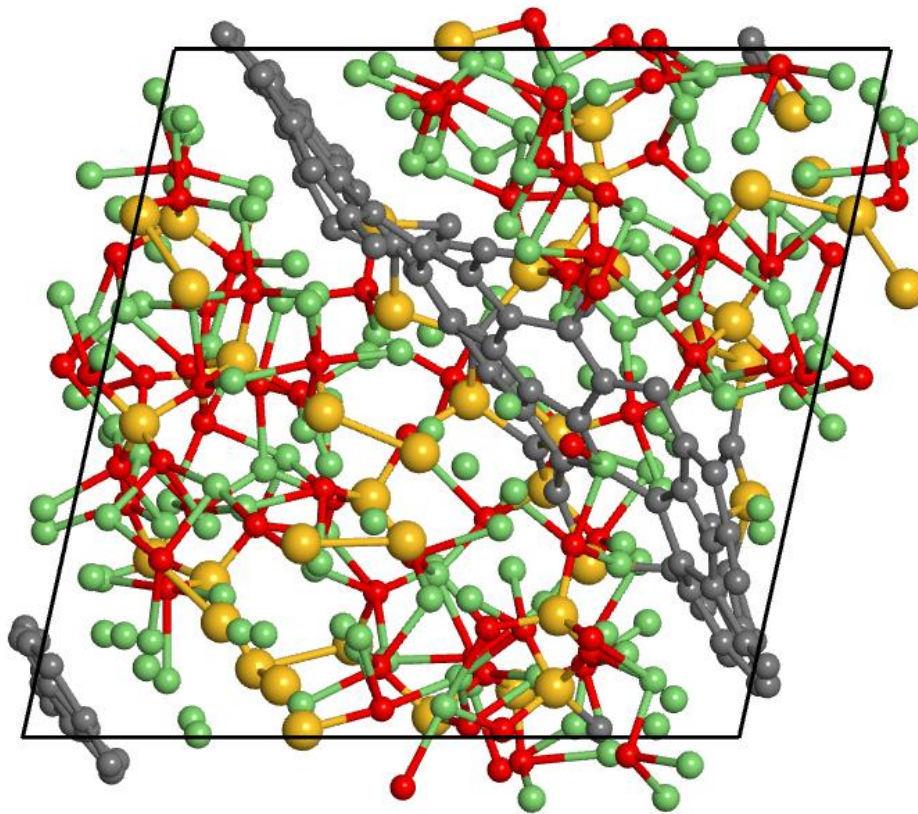


Figure 5.14 Fully lithiated structure of  $\text{SiC}_{2.2}\text{O}_{1.6}$

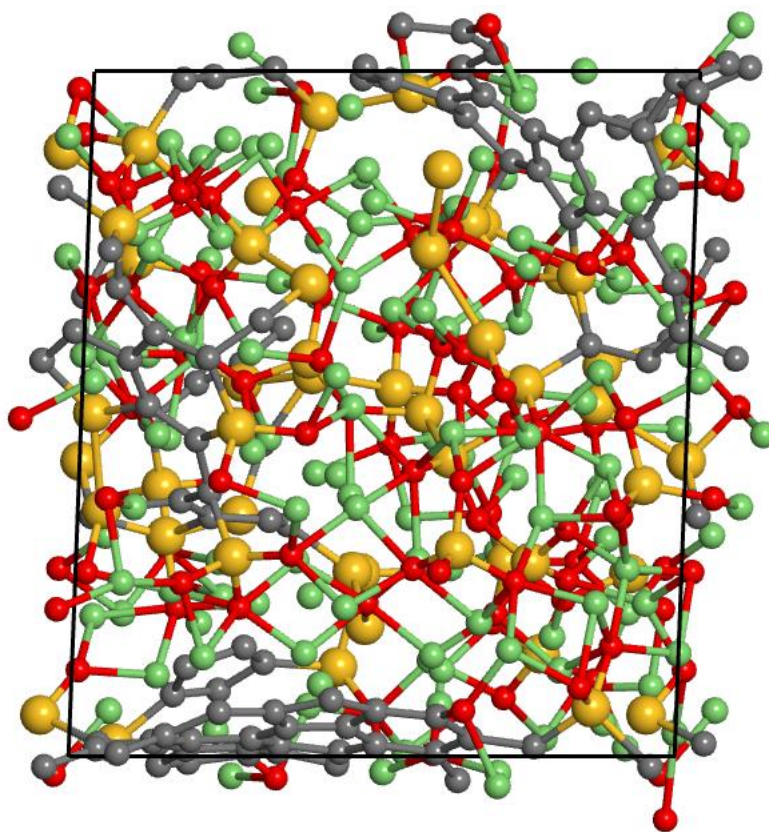


Figure 5.15 Fully lithiated structure of  $\text{SiC}_{1.65}\text{O}_{1.6}$

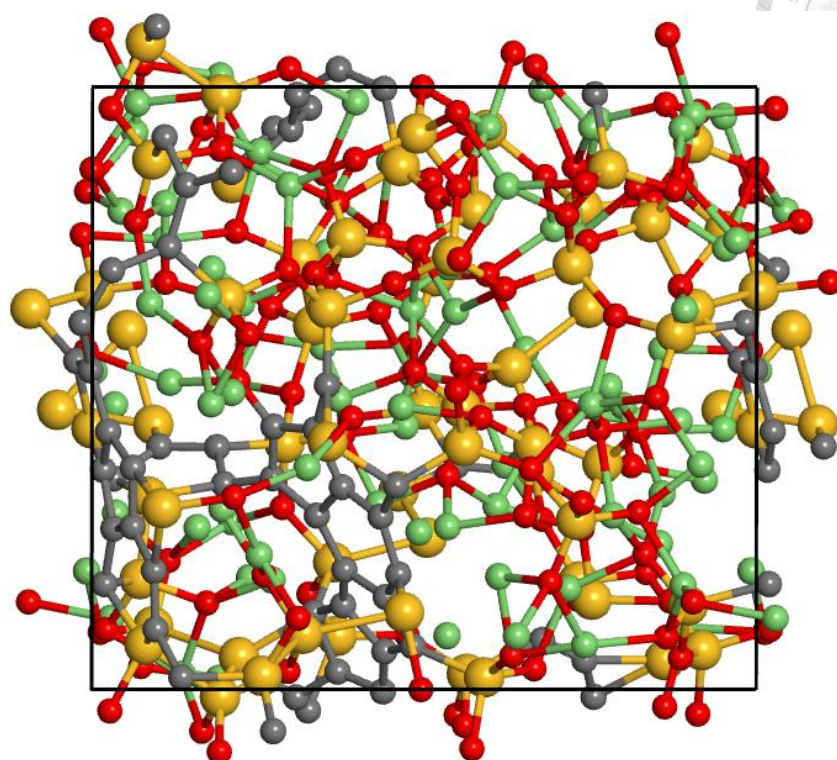


Figure 5.16 Fully lithiated structure of  $\text{SiC}_{0.8}\text{O}_{1.6}$

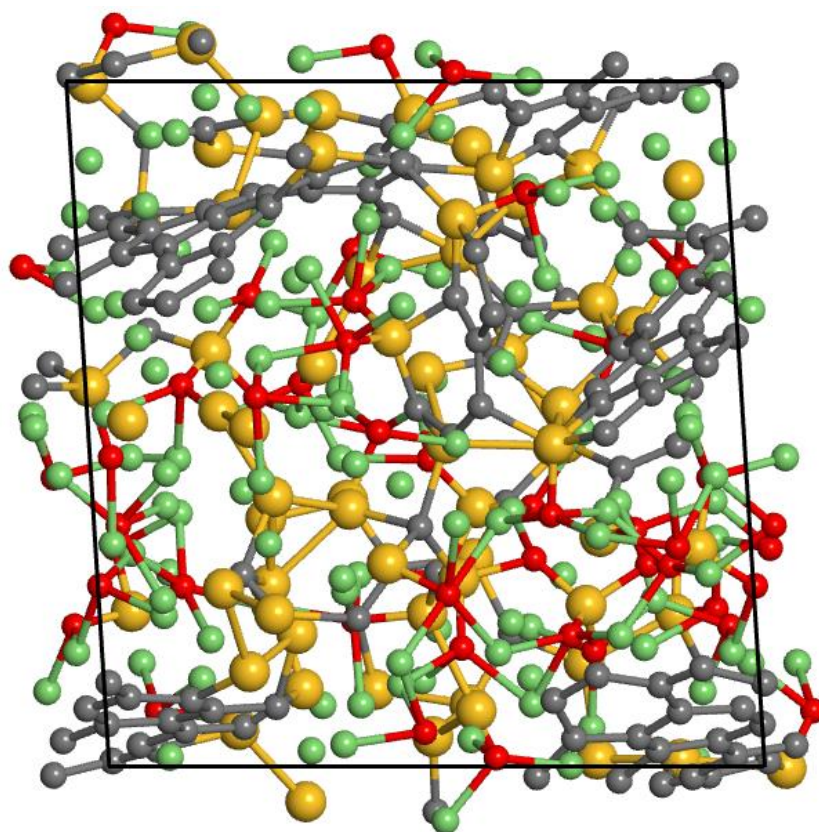
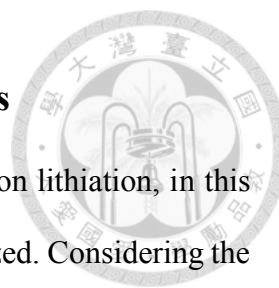


Figure 5.17 Fully lithiated structure of  $\text{SiC}_{1.65}\text{O}_{0.6}$

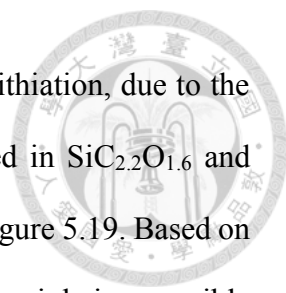


### 5.3.3 Structural evolution during the lithiation process

To explore the structural evolution of the amorphous SiOCs upon lithiation, in this section, the coordination number (CN) and relative volume are analyzed. Considering the first valley of the radial distribution functions of a-SiO<sub>2</sub> of 1.9,  $r \leq 1.9\text{\AA}$  is chosen as the representative cutoff radii for Si-O bonds. On the other hand,  $r \leq 2.15\text{\AA}$  is selected as the cutoff radii for Li-O bonds based on the O-Li bond length in lithium silicates, such as Li<sub>2</sub>Si<sub>2</sub>O<sub>5</sub> and Li<sub>4</sub>SiO<sub>4</sub><sup>[71], [72]</sup>.

The coordination numbers of O-Si and O-Li in lithiated SiC<sub>2.2</sub>O<sub>1.6</sub>, SiC<sub>1.65</sub>O<sub>1.6</sub>, SiC<sub>0.8</sub>O<sub>1.6</sub> and SiC<sub>1.65</sub>O<sub>0.6</sub> are shown in Figure 5.18. In all the pristine amorphous SiOCs, the initial CN of O-Si were very close to two, indicating that there were few coordination defects in SiOC glass phase. As the increasing Li concentration, the CN of O-Si slowly decreased in the first stage lithiation, which meant that electrons seldom filled to the Si-O anti-bonding states in the stage. Only the strained bonds that existed in the beginning would probably be broken by the electrons from Li. However, as the effect described in previous section, the electrons were prone to enter the SiOC glass phase in the second stage lithiation and filled the Si-O anti-bonding states. Therefore, the CN of O-Si decreased more rapidly in this stage compared to the first stage. Among the four different SiOC concentrations, the decrease of CN of O-Si in SiC<sub>1.65</sub>O<sub>0.6</sub> was the most radical because of the lowest oxygen content of it. In the other three systems, the evolution trends of CN of O-Si were almost the same on account of the same oxygen content of them.

The growing of CN of O-Li in lithiated SiOCs showed a reverse trend compared to the CN of O-Si, suggesting that Li was mainly attracted by O atoms in the structures. Among the four different SiOC concentrations, the growth of CN of O-Li in SiC<sub>1.65</sub>O<sub>0.6</sub> was the most rapidly, which was also thanks to the lowest oxygen content of it. The same as the trend of CN of O-Si, the evolution trend of CN of O-Si in SiC<sub>2.2</sub>O<sub>1.6</sub>, SiC<sub>1.65</sub>O<sub>1.6</sub>



and  $\text{SiC}_{0.8}\text{O}_{1.6}$  were similar to each other. During the late period of lithiation, due to the high lithium concentration, there was one  $\text{Li}_6\text{O}$  complex discovered in  $\text{SiC}_{2.2}\text{O}_{1.6}$  and  $\text{SiC}_{1.65}\text{O}_{0.6}$  respectively. The structure of  $\text{Li}_6\text{O}$  complex is shown in Figure 5.19. Based on the results from Chou et al. [73], the formation of  $\text{Li}_6\text{O}$  complex results mainly in reversible capacity rather than irreversible capacity, which caused by the formation of  $\text{Li}_2\text{O}$  or various lithium silicates.

In terms of volumetric changes, we calculate the relative volume by dividing the volume of lithiated SiOC structures by the volume of pristine SiOC structures. The relative volume expansions of amorphous SiOCs at different lithiation stages are calculated and compared to the calculation results of  $\text{Si}$  [74] and  $\text{SiO}_{1/3}$  [73], as shown in Figure 5.20. The results showed that the relative volumes of lithiated SiOCs increased linearly during the lithiation process. At the fully lithiated state, the maximum relative volumes for the amorphous SiOCs ranged from 1.24 to 1.44 and were much lower than the values of 3.69 for  $\text{Li}_4\text{Si}$  and 3.45 for  $\text{Li}_4\text{SiO}_{1/3}$ . In addition, the SiOC with higher carbon content presented a smaller volume expansion in the process of lithiation, suggesting that besides being a reservoir of electrons, the free carbon phase also effectively limited the volume expansion of the systems during the lithiation process.

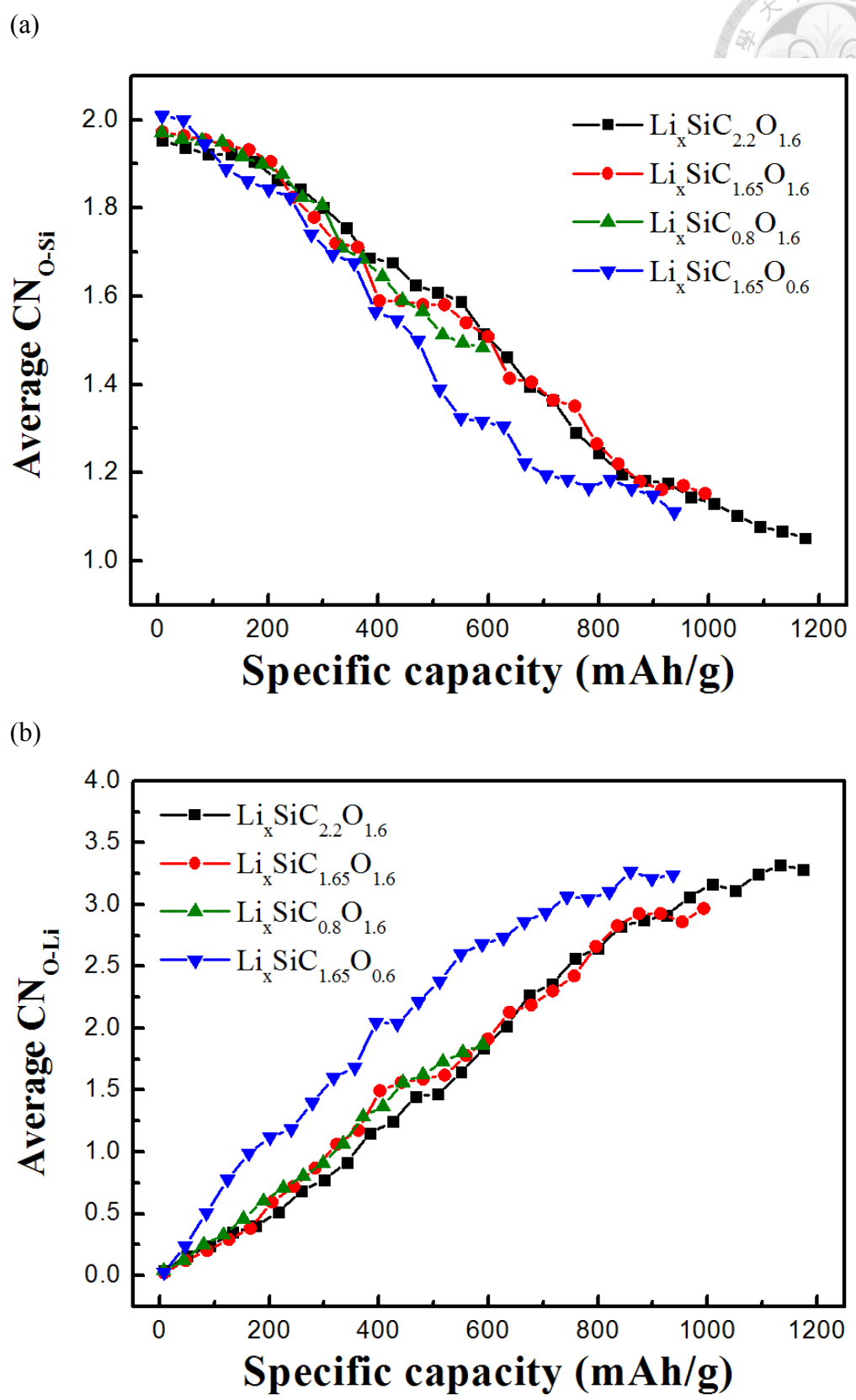
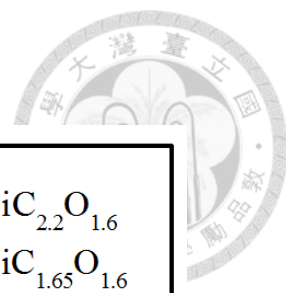


Figure 5.18 Average coordination numbers of: (a) O-Si, (b) O-Li in lithiated amorphous SiOCs

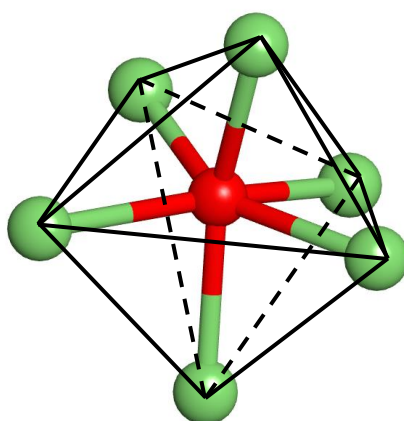


Figure 5.19 Structure of  $\text{Li}_6\text{O}$  complex

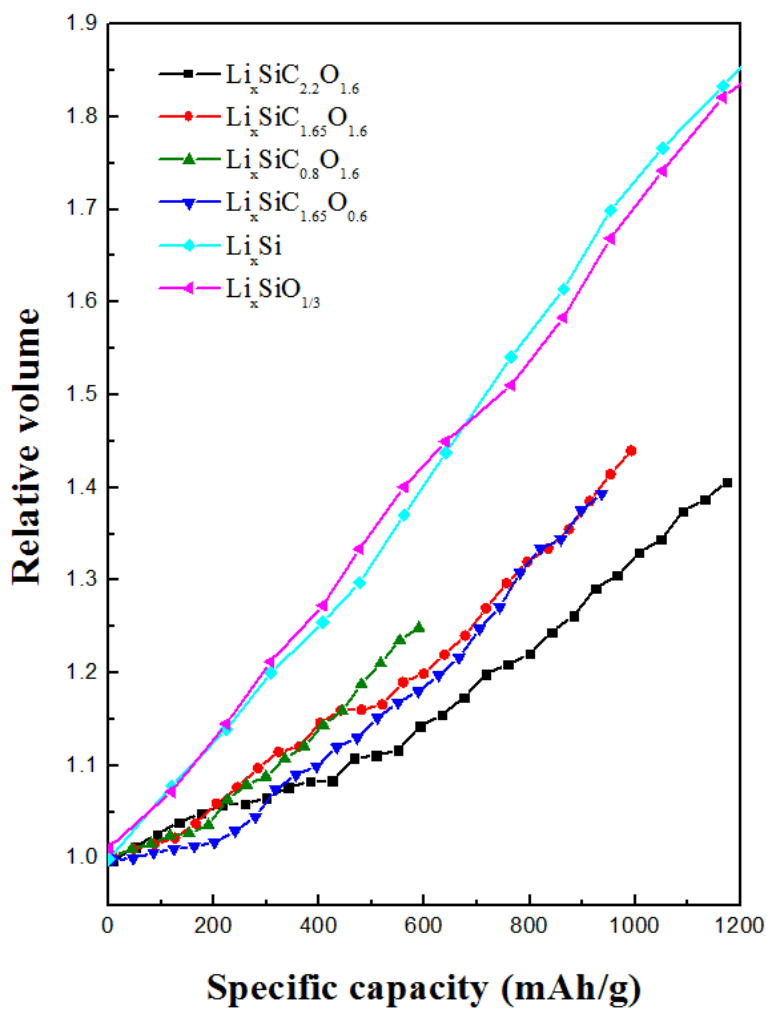
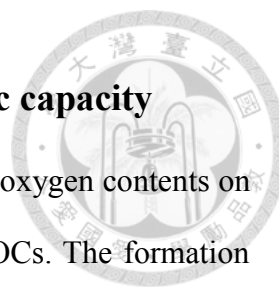


Figure 5.20 Relative volume of lithiated amorphous SiOCs, Si<sup>[74]</sup> and SiO<sub>1/3</sub><sup>[73]</sup>

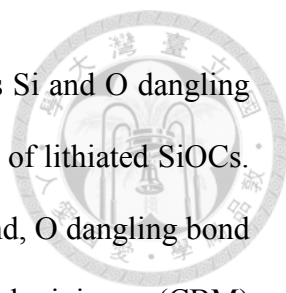


### 5.3.4 Effects of carbon and oxygen contents on specific capacity

In this section, we are going to discuss the effect of carbon and oxygen contents on the lithiation energetics and specific capacity of the amorphous SiOCs. The formation energies of lithiated  $\text{SiC}_{2.2}\text{O}_{1.6}$ ,  $\text{SiC}_{1.65}\text{O}_{1.6}$ ,  $\text{SiC}_{0.8}\text{O}_{1.6}$  and  $\text{SiC}_{1.65}\text{O}_{0.6}$  are shown in Figure 5.21 (a). The formation energies gradually decreased with the insertion of Li and reached a minimum value while the SiOCs were fully lithiated. The higher the carbon and oxygen contents, the lower the formation energy profile is, indicating that Li incorporation is energetically more favorable in the SiOCs with high carbon and oxygen concentrations. The most stable concentrations for  $\text{Li}_x\text{SiC}_{2.2}\text{O}_{1.6}$ ,  $\text{Li}_x\text{SiC}_{1.65}\text{O}_{1.6}$ ,  $\text{Li}_x\text{SiC}_{0.8}\text{O}_{1.6}$  and  $\text{Li}_x\text{SiC}_{1.65}\text{O}_{0.6}$  are calculated as  $x = 3.53$ ,  $2.74$ ,  $1.40$  and  $2.02$  respectively, corresponding to the theoretical lithium capacities of 1175, 993, 590 and 937 mAh/g.

The voltage profile of lithiated SiOCs are shown in Figure 5.21 (b) and Figure 5.21 (c). The initial voltages are higher in the SiOCs with high carbon and oxygen contents, which is also attributed to the stronger interactions between Li and the SiOCs with high carbon and oxygen concentrations. It also means that the rising proportion of free carbon in the systems make the initial voltage of the amorphous SiOCs higher. After the initial stage of lithiation, the voltages of lithiated SiOCs all ranged around 0.5-1.0 V, indicating the same mechanisms of lithiation, which are the break of Si-O bonds and the formation of Li-O bonds during Li insertion.

From the results above, it can be conclude that the higher the concentration of carbon, the better the performance of the amorphous SiOCs in theoretical capacity. However, the information of reversible and irreversible capacities of anode materials are much more important in practical use. First, the irreversible capacities usually comes from the too strong interactions between Li ions and the anode materials, SEI formations, poor conductivity of the systems, etc. In amorphous SiOCs, the breaks of Si-O bonds during



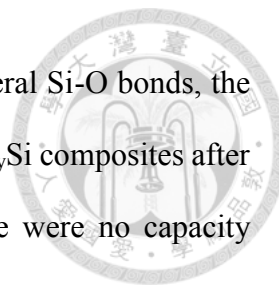
lithiation process induces a large number of localized states, such as Si and O dangling bonds, between the fermi level of pristine SiOCs and the fermi level of lithiated SiOCs. By calculations of amorphous SiO<sub>2</sub>, the alignment of Si dangling bond, O dangling bond together with the valence band maximum (VBM) and conduction band minimum (CBM) is shown in Figure 5.22. The 2.3 eV and 3.7 eV of energies between Si, O dangling bonds and the CBM, which is Si-O anti-bonding states, make it too difficult for electrons to be excited and transfer to the cathode in the spontaneous discharging process, finally leading to the stocked Li ions in SiOC phase, which is irreversible loss of the material. Thus, the electrons that fill to the states of Si and O dangling bonds are the major source of the irreversible capacity in amorphous SiOCs.

Based on the concept mentioned above, we calculate the charge gain on Si, C and O atoms according to the local density of states of fully lithiated SiOCs as shown in Figure 5.23 to Figure 5.26. The charge gain on Si, C, and O atoms in fully lithiated SiC<sub>2.2</sub>O<sub>1.6</sub>, SiC<sub>1.65</sub>O<sub>1.6</sub>, SiC<sub>0.8</sub>O<sub>1.6</sub> and SiC<sub>1.65</sub>O<sub>0.6</sub> are shown in Table 5.1. The charge gain on C atoms corresponds to reversible capacity, while the charge gain on Si and O atoms correspond to irreversible capacity of amorphous SiOCs. Finally, the reversible capacity, irreversible capacity and reversibility of SiC<sub>2.2</sub>O<sub>1.6</sub>, SiC<sub>1.65</sub>O<sub>1.6</sub>, SiC<sub>0.8</sub>O<sub>1.6</sub> and SiC<sub>1.65</sub>O<sub>0.6</sub> are listed in Table 5.2. The reversibility of SiC<sub>2.2</sub>O<sub>1.6</sub>, SiC<sub>1.65</sub>O<sub>1.6</sub>, SiC<sub>0.8</sub>O<sub>1.6</sub> and SiC<sub>1.65</sub>O<sub>0.6</sub> are 52.0, 50.7, 42.0 and 52.5% respectively, indicating that high carbon concentration as well as low oxygen concentration in amorphous SiOCs will lead to better performance on reversibility. Furthermore, the reversible capacities are in good agreement with the experimental results.

In addition, the local density of state of Si shows a dip at fermi level in all the lithiated SiOCs, suggesting that there are not Li-Si alloying in the SiOC systems. On the other hand, the average coordination numbers of Si atoms, including Si-Si, Si-O and Si-C, in fully lithiated SiC<sub>2.2</sub>O<sub>1.6</sub>, SiC<sub>1.65</sub>O<sub>1.6</sub>, SiC<sub>0.8</sub>O<sub>1.6</sub> and SiC<sub>1.65</sub>O<sub>0.6</sub> are 2.95, 3.28, 3.58



and 3.23 respectively, indicating that in spite of the breaking of several Si-O bonds, the Si atoms are still in the bond network of SiOCs instead of forming  $\text{Li}_y\text{Si}$  composites after lithiation. With the above evidence, it can be concluded that there were no capacity contribution from  $\text{Li}_y\text{Si}$  composites in our systems.



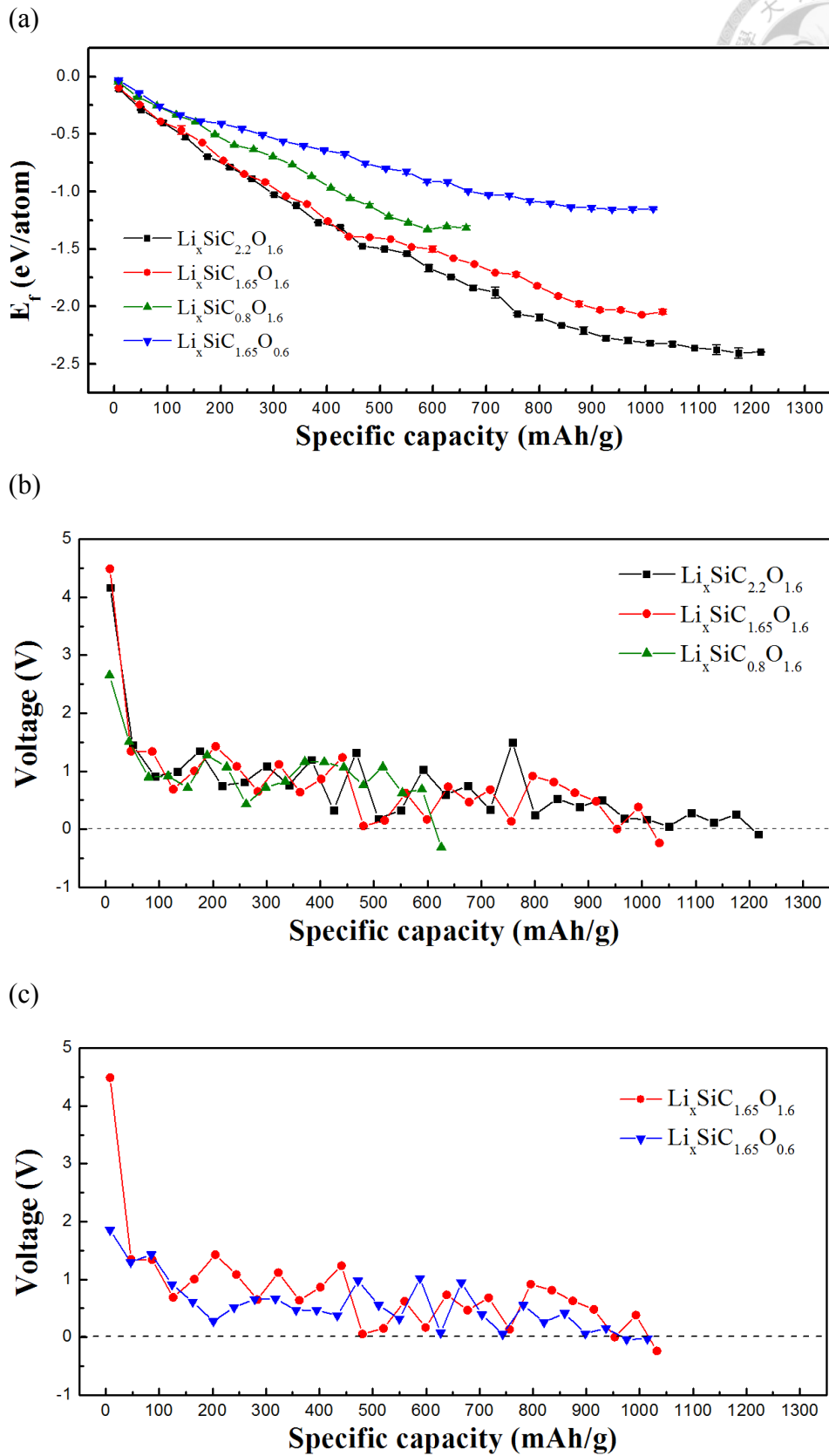


Figure 5.21 (a) Formation energies of lithiated SiOCs, (b) voltage of lithiated SiOCs in different C concentrations, (c) voltage of lithiated SiOCs in different O concentrations

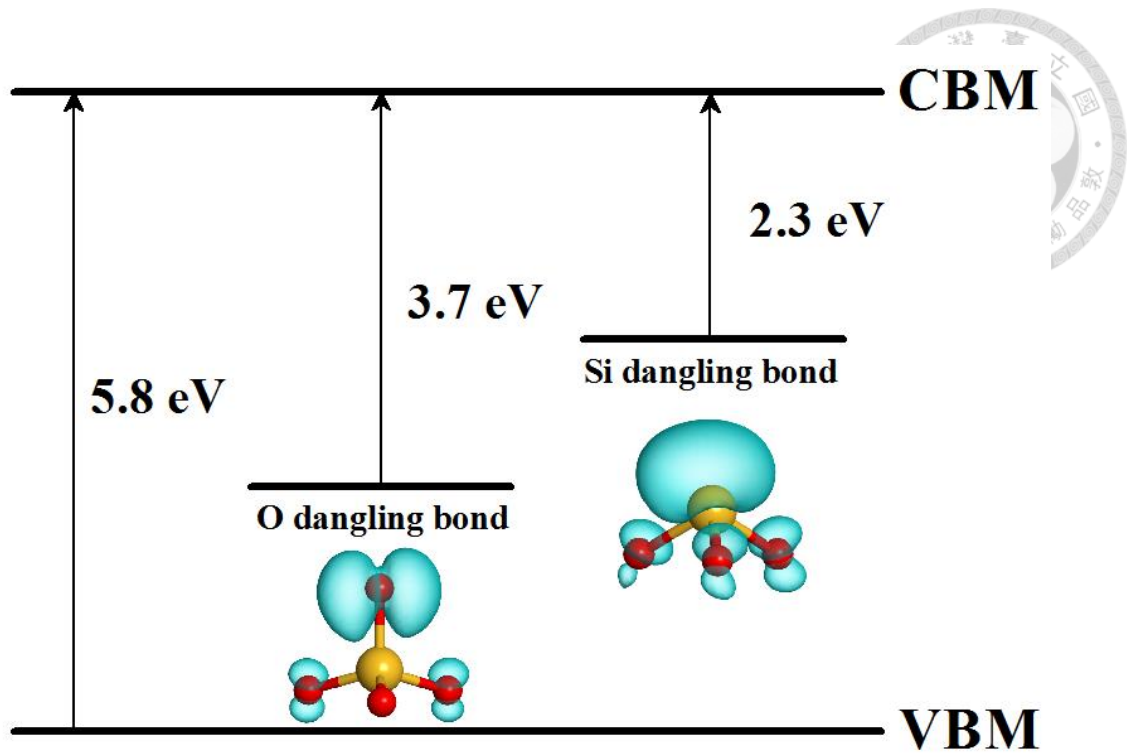


Figure 5.22 alignment of Si dangling bond, O dangling bond together with the valence band maximum (VBM) and conduction band minimum (CBM) of a-SiO<sub>2</sub>

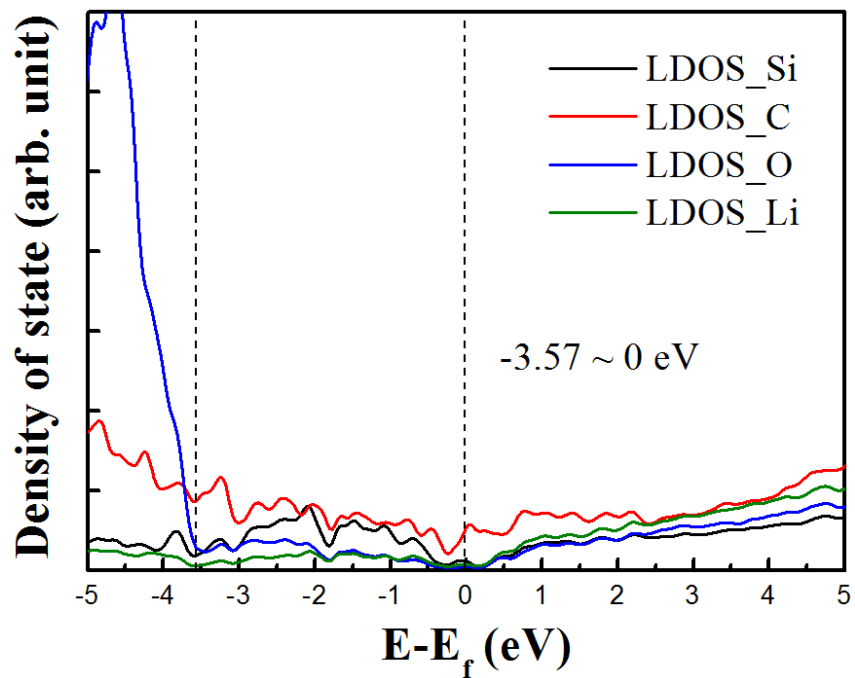


Figure 5.23 Local density of state of fully lithiated SiC<sub>2.2</sub>O<sub>1.6</sub>

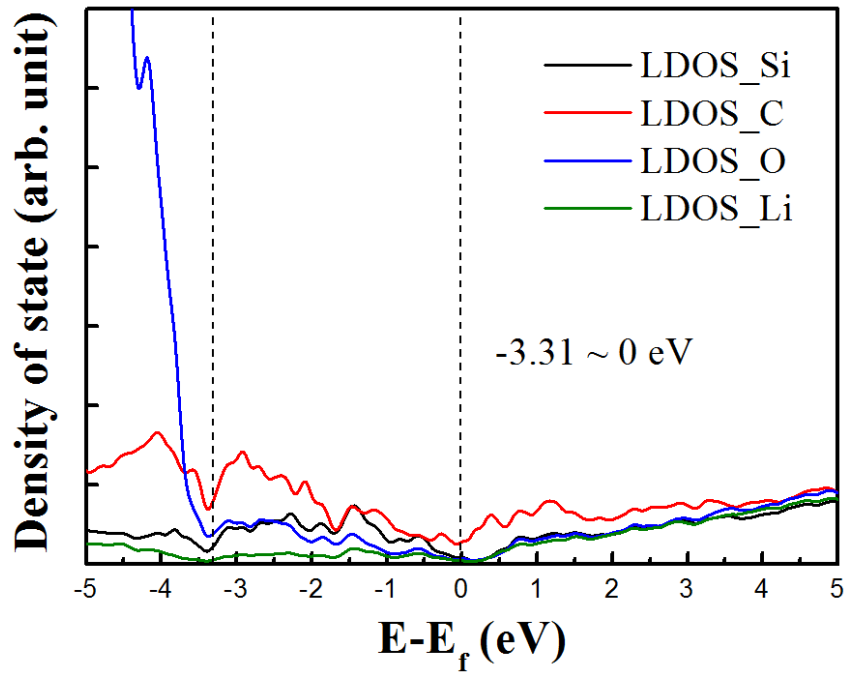


Figure 5.24 Local density of state of fully lithiated  $\text{SiC}_{1.65}\text{O}_{1.6}$

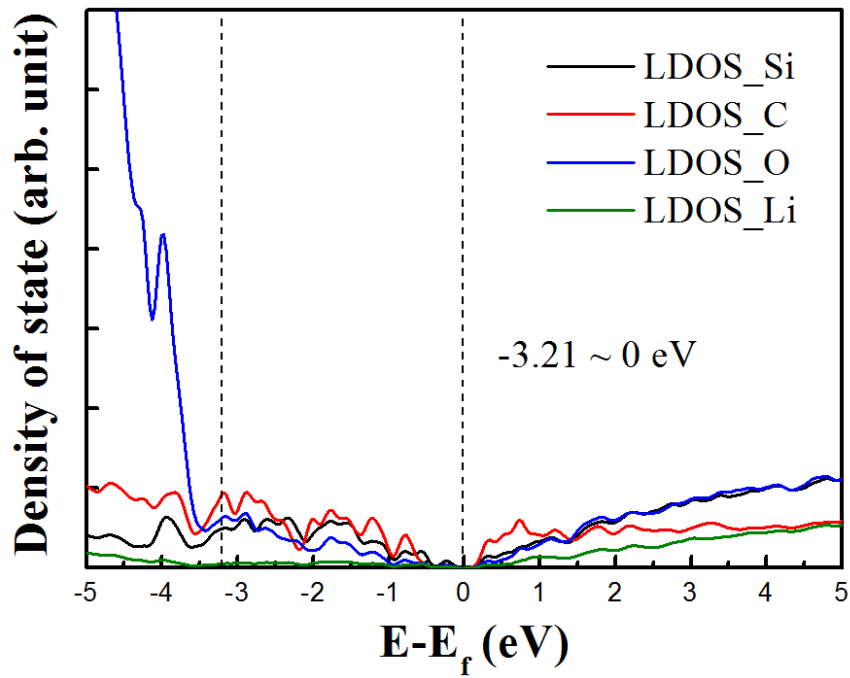


Figure 5.25 Local density of state of fully lithiated  $\text{SiC}_{0.8}\text{O}_{1.6}$

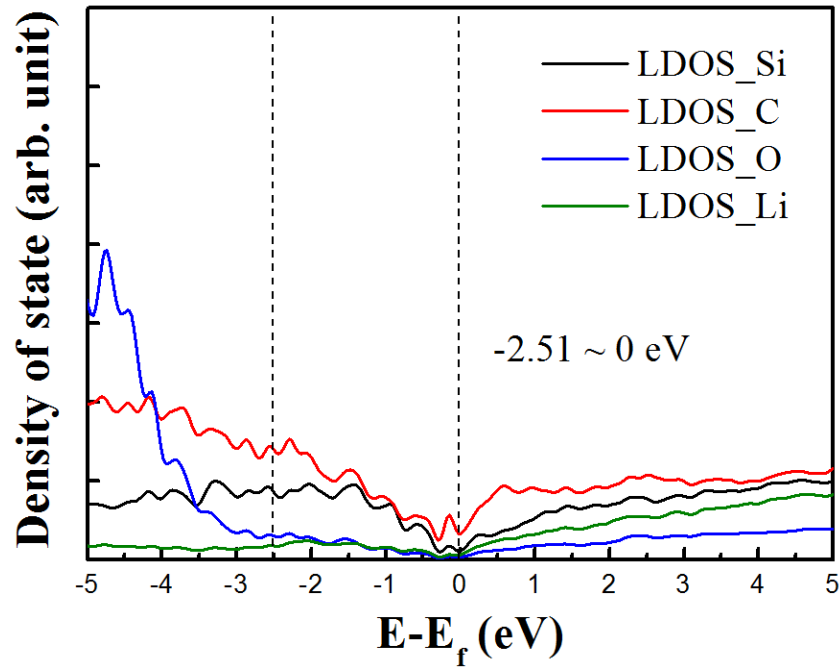


Figure 5.26 Local density of state of fully lithiated  $\text{SiC}_{1.65}\text{O}_{0.6}$

Table 5.1 Charge gain in different atoms of fully lithiated SiOCs

Charge gain (%)	Si	C	O
$\text{SiC}_{2.2}\text{O}_{1.6}$	30.6	52.0	17.4
$\text{SiC}_{1.65}\text{O}_{1.6}$	28.0	50.7	21.3
$\text{SiC}_{0.8}\text{O}_{1.6}$	34.0	42.0	24.0
$\text{SiC}_{1.65}\text{O}_{0.6}$	37.4	52.5	10.1

Table 5.2 Capacities and reversibility of the amorphous SiOCs

	Capacity (mAh/g)			Reversibility (%)
	Reversible	Irreversible	Total	
$\text{SiC}_{2.2}\text{O}_{1.6}$	611	564	1175	52.0
$\text{SiC}_{1.65}\text{O}_{1.6}$	503	490	993	50.7
$\text{SiC}_{0.8}\text{O}_{1.6}$	247	343	590	42.0
$\text{SiC}_{1.65}\text{O}_{0.6}$	492	445	937	52.5



## 5.4 Summary

In this chapter, we studied the lithiation mechanism of amorphous SiOCs in four different concentrations, which are  $\text{SiC}_{2.2}\text{O}_{1.6}$ ,  $\text{SiC}_{1.65}\text{O}_{1.6}$ ,  $\text{SiC}_{0.8}\text{O}_{1.6}$  and  $\text{SiC}_{1.65}\text{O}_{0.6}$ . The lithiation process can be briefly divided into two stages. In the first lithiation stage, the Li ions were absorbed on the oxygen atoms at the surface of SiOC glass phase, while the electrons from Li filled the states of carbon atoms in free carbon phase. In the second lithiation stage, as the lithium concentrations went higher, the Li ions began to interact with SiOC glasses because of stress accumulated in the first stage lithiation, the shift of fermi level of the systems and the effect of electric field at the interface between free carbon and SiOC glass phase. In this stage, not only SiOC glass but free carbon phase were receiving the electrons from Li, indicating that the free carbon acted as a reservoir of electrons in SiOC systems.

As the rising of Li concentration, the average CNs of O-Si and O-Li in lithiated SiOCs gradually decrease and increase respectively since the electrons from Li fill the Si-O anti-bonding states. In terms of volumetric changes, the maximum relative volumes for the fully lithiated amorphous SiOCs were much lower than those for  $\text{Li}_4\text{Si}$  and  $\text{Li}_4\text{SiO}_{1/3}$ . Moreover, the SiOC with higher carbon content presented a smaller volume expansion in the process of lithiation, suggesting that the free carbon effectively limited the volume expansion of the systems during the lithiation process.

Finally, the theoretical capacities of  $\text{SiC}_{2.2}\text{O}_{1.6}$ ,  $\text{SiC}_{1.65}\text{O}_{1.6}$ ,  $\text{SiC}_{0.8}\text{O}_{1.6}$  and  $\text{SiC}_{1.65}\text{O}_{0.6}$  are 1175, 993, 590 and 937 mAh/g respectively, suggesting that the higher carbon content will result in the higher specific capacities of amorphous SiOCs. In terms of reversible capacities of amorphous SiOCs, the high carbon concentration as well as low oxygen concentration in amorphous SiOCs will lead to better performance on reversibility.

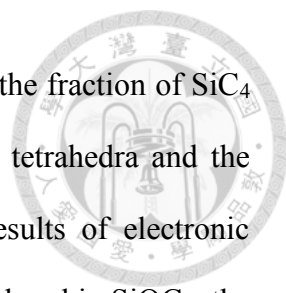
## Chapter 6 Conclusions



In this thesis, we performed ReaxFF and first principles calculations to model the structures of amorphous SiOCs. The electronic structures, the lithiation mechanism and the source of irreversible capacities of amorphous SiOCs are further studied by *ab initio* calculations.

In the first part of this thesis, we modify the ReaxFF parameter set for Si/O/C based on the parameters from Ponomarev et al. (UTA1). The cohesive energies, lattice constants as well as elastic constants for diamond, graphite, SiO<sub>2</sub> ( $\alpha$ -quartz) and SiC ( $\beta$ -SiC) are calibrated so that our potential model are able to construct reasonable and reliable structures of SiOCs. The results show that due to the improvements mentioned above, especially for the elastic constants of SiC, the carbon atoms are more likely to have the tendency to be discovered in SiOC glass phase. Thus, the decrease of carbon atoms in free carbon phase make the free carbon layers in our model flatter compared to those in UTA1's model. Furthermore, the calibrations of elastic constants and cohesive energies of SiO<sub>2</sub> and SiC indirectly improve the original high tolerance in over- and under-coordinated silicon atoms and three-coordinated oxygen atoms of UTA1 potential, leading to the less coordination defects in amorphous SiOC structures built via our potential parameters. Finally, thanks to the above improvements, the parameters fitted in this work are able to construct the amorphous SiOC structures that are thermodynamically more stable than the structures constructed via UTA1 parameters.

In the second part of this thesis, we construct the amorphous SiOC structures in six different concentrations, SiC<sub>3.3</sub>O<sub>1.6</sub>, SiC<sub>2.2</sub>O<sub>1.6</sub>, SiC<sub>1.65</sub>O<sub>1.6</sub>, SiC<sub>0.8</sub>O<sub>1.6</sub>, SiC<sub>1.65</sub>O<sub>1.1</sub> and SiC<sub>1.65</sub>O<sub>0.6</sub>, via *ab initio* melt-and-quench MD simulations. The results show that decreasing the carbon and oxygen contents will result in the lowering of the proportion of carbon atoms in free carbon phase. Besides, the increase of carbon concentration as



well as the decrease of oxygen concentration will induce the rise of the fraction of  $\text{SiC}_4$  and  $\text{SiC}_3\text{O}$  tetrahedra, the drop in the fraction of  $\text{SiCO}_3$  and  $\text{SiO}_4$  tetrahedra and the decline in PV and SSA in amorphous SiOC. Furthermore, the results of electronic structures suggest that the higher the fraction of Si-C bond and Si-Si bond in SiOCs, the narrower the band gap of the SiOC glass phase.

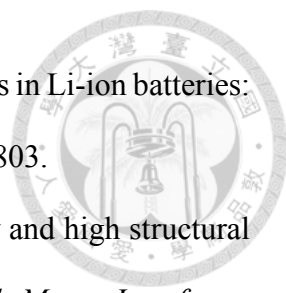
In the final part of this thesis, we conduct the lithiation calculations on four different SiOC concentrations,  $\text{SiC}_{2.2}\text{O}_{1.6}$ ,  $\text{SiC}_{1.65}\text{O}_{1.6}$ ,  $\text{SiC}_{0.8}\text{O}_{1.6}$  and  $\text{SiC}_{1.65}\text{O}_{0.6}$ , to clarify the lithiation mechanism of amorphous SiOCs. The lithiation process can be briefly divided into two stages. In the first lithiation stage, the Li ions are absorbed on the oxygen atoms at the surface of SiOC glass phase, while the electrons from Li fill the states of carbon atoms in free carbon phase. In the second lithiation stage, the Li ions start to interact with SiOC glasses leading to the gradual decrease and increase of the average CNs of O-Si and O-Li respectively in lithiated SiOCs. The SiOCs with higher carbon content present smaller volume expansions in the process of lithiation, suggesting that besides being a reservoir of electrons, the free carbon phase also effectively limit the volume expansion of the systems during the lithiation process. Finally, the higher the carbon content, the better the performance of amorphous SiOCs on reversible and total capacities. On the other hand, the high carbon concentration as well as low oxygen concentration in amorphous SiOCs will lead to better performance on reversibility.

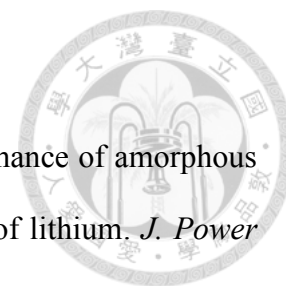


## Reference



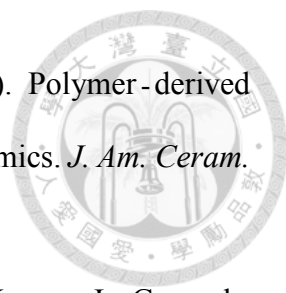
- [1] Liang, Y., Jing, Y., Gheyhani, S., Lee, K.Y., Liu, P., Facchetti, A., & Yao, Y. (2017). Universal quinone electrodes for long cycle life aqueous rechargeable batteries. *Nature Mater*, *16*, 841–848.
- [2] Turcheniuk, K., Bondarev, D., Singhal, V., & Yushin, G. (2018). Ten years left to redesign lithium-ion batteries. *Nature*, *559*, 467–470.
- [3] Schmuch, R., Wagner, R., Hörpel, G., Placke, T., & Winter, M. (2018). Performance and cost of materials for lithium-based rechargeable automotive batteries. *Nature Energy*, *3*, 267–278.
- [4] Yan, L., Yu, J., & Luo, H. (2017). Ultrafine TiO<sub>2</sub> nanoparticles on reduced graphene oxide as anode materials for lithium ion batteries. *Appl. Mater. Today*, *8*, 31–34.
- [5] Kasavajjula, U., Wang, C., & Appleby, A. J. (2007). Nano- and bulk-silicon based insertion anodes for lithium-ion secondary cells. *J. Power Sources*, *163*, 1003–1039.
- [6] Singh, V., Joung, D., Zhai, L., Das, S., Khondaker, S. I., & Seal, S. (2011). Graphene based materials: past, present and future. *Prog. Mater. Sci.*, *56*(8), 1178–1271.
- [7] Han, J., Kong, D., Lv, W., Tang, D.M., Han, D., Zhang, C., Liu, D., Xiao, Z., Zhang, X., Xiao, J., ... Yang, Q. H. (2018). Caging tin oxide in three-dimensional graphene networks for superior volumetric lithium storage. *Nat. Commun*, *9*, 402.
- [8] Shan, C., Yen, H.J., Wu, K., Lin, Q., Ming, Z., Guo, X., Di, W., Zhang, H., Gang, W., & Wang, H.L. (2017). Functionalized fullerenes for highly efficient lithium ion storage: structure-property-performance correlation with energy implications, *Nano Energy*, *40*, 327–335.
- [9] Zhang, S., Zhao, K., Zhu, T., & Li, J. (2017). Electrochemomechanical degradation of high-capacity battery electrode materials. *Prog. Mater. Sci.*, *89*, 479–521.


- 
- [10] Xu, R., & Zhao, K. (2016) Electrochemomechanics of electrodes in Li-ion batteries: a review. *J. Electrochem. Energy Convers. Storage*, 13(3), 030803.
- [11] Sun, H., & Zhao, K. (2017). Atomistic origins of high capacity and high structural stability of polymer-derived SiOC anode materials. *ACS Appl. Mater. Interfaces*, 9(40), 35001–35009.
- [12] Ryu, J., Chen, T., Bok, T., Song, G., Ma, J., Hwang, C., Luo, L., Song, H.K., Cho, J., & Wang, C. (2018). Mechanical mismatch-driven rippling in carbon-coated silicon sheets for stress-resilient battery anodes. *Nat. Commun*, 9, 2924.
- [13] Zhang, Q., Chen, H., Luo, L., Zhao, B., Luo, H., Han, X., Wang, J., Wang, C., Yang, Y., Zhu, T., & Liu, M. (2018). Harnessing the concurrent reaction dynamics in active Si and Ge to achieve high performance of lithium-ion batteries. *Energy Environ. Sci.* 11, 669–681.
- [14] Ogata, K., Jeon, S., Ko, D. S., Jung, I. S., Kim, J. H., Ito, K., Kubo, Y., Takei, K., Saito, S., Cho, Y. H., ...Han, S. (2018). Evolving affinity between Coulombic reversibility and hysteretic phase transformations in nano-structured silicon-based lithium-ion batteries. *Nat. Commun*, 9, 479.
- [15] Krishnan, R., Lu, T.-M., & Koratkar, N. (2011). Functionally strain-graded nanoscoops for high power Li-ion battery anodes. *Nano Lett*, 11(2), 377–384.
- [16] Kim, H., & Cho, J. (2008). Superior lithium electroactive mesoporous Si@carbon core-shell nanowires for lithium battery anode material. *Nano Lett*, 8(11), 3688–3691.
- [17] Yao, Y., McDowell, M. T., Ryu, I., Wu, H., Liu, N., Hu, L., Nix, W. D., & Cui, Y. (2011). Interconnected silicon hollow nanospheres for lithium-ion battery anodes with long cycle life. *Nano Lett*, 11(7), 2949–2954.
- [18] Ahn, D., & Raj, R. (2010). Thermodynamic measurements pertaining to the hysteretic intercalation of lithium in polymer-derived silicon oxycarbide. *J. Power*



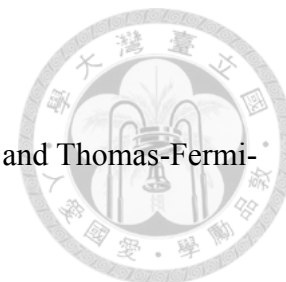
*Sources*, 195(12), 3900–3906.

- [19] Ahn, D., & Raj, R. (2011). Cyclic stability and C-rate performance of amorphous silicon and carbon based anodes for electrochemical storage of lithium. *J. Power Sources*, 196(4), 2179–2186.
- [20] Sanchez-Jimenez, P. E., & Raj, R. (2010). Lithium insertion in polymer-derived silicon oxycarbide ceramics. *J. Am. Ceram. Soc.*, 93(4), 1127–1135.
- [21] Bhandavat, R., & Singh, G. (2013). Stable and efficient Li-ion battery anodes prepared from polymer-derived silicon oxycarbide–carbon nanotube shell/core composites. *J. Phys. Chem. C*, 117(23), 11899–11905.
- [22] Fukui, H., Ohsuka, H., Hino, T., & Kanamura, K. (2010). A Si–O–C composite anode: high capability and proposed mechanism of lithium storage associated with microstructural characteristics. *ACS Appl. Mater. Interfaces*, 2(4), 998–1008.
- [23] Fukui, H., Harimoto, Y., Akasaka, M., & Eguchi, K. (2014). Lithium species in electrochemically lithiated and delithiated silicon oxycarbides. *ACS Appl. Mater. Interfaces*, 6(15), 12827–12836.
- [24] Kaspar, J., Graczyk-Zajac, M., Lauterbach, S., Kleebe, H.-J., & Riedel, R. (2014). Silicon oxycarbide/nano-silicon composite anodes for Li-ion batteries: considerable influence of nano-crystalline vs. nano-amorphous silicon embedment on the electrochemical properties. *J. Power Sources*, 269, 164–172.
- [25] Liao, N., Zheng, B., Zhou, H., & Xue, W. (2015). Effect of carbon content on the structure and electronic properties of silicon oxycarbide anodes for lithium-ion batteries: a first-principles study. *J. Mater. Chem. A*, 3, 5067–5071.
- [26] Halim, M., Hudaya, C., Kim, A. Y., & Lee, J. K. (2016). Phenyl-rich silicone oil as a precursor for SiOC anode materials for long-cycle and high-rate lithium ion batteries. *J. Mater. Chem. A*, 4, 2651–2656.

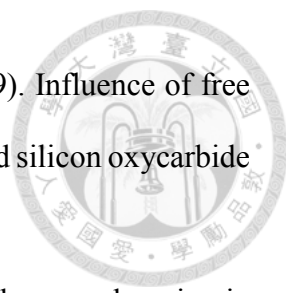
- 
- [27] Colombo, P., Mera, G., Riedel R., & Sorarù, G. D. (2010). Polymer-derived ceramics: 40 years of research and innovation in advanced ceramics. *J. Am. Ceram. Soc.*, *93*(7), 1805–1837.
- [28] Wilamowska-Zawlocka, M., Puczkarski, P., Grabowska, Z., Kaspar, J., Graczyk-Zajac, M., Riedel, R., & Sorarù, G. D. (2016). Silicon oxycarbide ceramics as anodes for lithium ion batteries: influence of carbon content on lithium storage capacity. *RSC Adv.*, *6*(106), 104597–104607.
- [29] Sadezky, A., Muckenhuber, H., Grothe, H., Niessner, R., & Pöschl, U. (2005). Raman microspectroscopy of soot and related carbonaceous materials: spectral analysis and structural information. *Carbon*, *43*(8), 1731–1742.
- [30] Tuinstra, F., & Koenig, L. (1970). Raman spectrum of graphite. *J. Chem. Phys.*, *53*, 1126–1130.
- [31] Sato, K., Saito, R., Oyama, Y., Jiang, J., Cançado, L. G., Pimenta, M. A., Jorio, A., Samsonidze, G. G., Dresselhaus, G., & Dresselhaus, M. S. (2006). D-band Raman intensity of graphitic materials as a function of laser energy and crystallite size. *Chem. Phys. Lett.*, *427*, 117–121.
- [32] Beyssac, O., Goffé, B., Petitet, J., Froigneux, P. E., Moreau M., & Rouzaud, J. N. (2003). On the characterization of disordered and heterogeneous carbonaceous materials by Raman spectroscopy. *Spectrochim. Acta Mol. Biomol. Spectros.*, *59*(10), 2267–2276.
- [33] Mera, G., Navrotsky, A., Sen, S., Kleebe, H.-J., & Riedel, R. (2013). Polymer-derived SiCN and SiOC ceramics - structure and energetics at the nanoscale. *J. Mater. Chem. A*, *1*, 3826–3836.
- [34] David, L., Bhandavat, R., Barrera, U., & Singh, G. (2016). Silicon oxycarbide glass-graphene composite paper electrode for long-cycle lithium-ion batteries. *Nat. Commun.*, *7*, 10998.

- 
- [35] Dibandjo, P., Graczyk-Zajac, M., Riedel, R., Pradeep, V. S., & Sorarù, G. D. (2012). Lithium insertion into dense and porous carbon-rich polymer-derived SiOC ceramics. *J. Eur. Ceram. Soc.*, 32(10), 2495–2503.
- [36] Liu, X., Zheng, M. C., & Xie, K. (2011). Mechanism of lithium storage in Si–O–C composite anodes. *J. Power Sources*, 196(24), 10667–10672.
- [37] Graczyk-Zajac, M., Vrankovic, D., Waleska, P., Hess, C., Sasikumar, P. V., Lauterbach, S., ...Sorarù, G. D. (2018). The Li-storage capacity of SiOC glasses with and without mixed silicon oxycarbide bonds. *J. Mater. Chem. A.*, 6, 93–103.
- [38] Liao, N., Zheng, B., Zhang, M., & Xue, W. (2016). Atomic investigating on reversible lithium storage in amorphous silicon oxycarbide as high power anode material. *J. Mater. Chem. A*, 4, 12328-12333.
- [39] Liao, N., Zheng, B., Zhang, M., & Xue, W. (2017). First-principles calculation of lithium insertion into homogeneous a-SiC<sub>2/5</sub>O<sub>6/5</sub> as high performance anode. *RSC Adv.*, 7, 30559-30563.
- [40] Tersoff, J. (1990). Modeling solid-state chemistry: interatomic potentials for multicomponent systems. *Phys. Rev. B*, 41, 3248.
- [41] Munetoh, S., Motooka, T., Moriguchi, K., & Shintani, A. (2007). Interatomic potential for Si–O systems using Tersoff parameterization. *Comput. Mater. Sci.*, 39(2), 334–339.
- [42] Oganov, A. R., & Glass, C. W. (2006). Crystal structure prediction using ab-initio evolutionary techniques: principles and applications. *J. Chem. Phys.*, 124, 244704.
- [43] Kroll, P. (2011). Tracing reversible and irreversible Li insertion in SiCO ceramics with modeling and Ab-Initio simulations. *MRS Online Proc Libr.*, 1313, 1–6.
- [44] Thomas, L. H. The calculation of atomic fields. In *Mathematical Proceedings of the Cambridge Philosophical Society*, (1927, January), (Vol. 23, No. 5, pp. 542-548).

Cambridge University Press.



- [45] Latter, R. (1955). Atomic energy levels for the Thomas-Fermi and Thomas-Fermi-Dirac potential. *Physical Review*, 99(2), 510.
- [46] Hohenberg, P., & Kohn, W. (1964). Inhomogeneous electron gas. *Physical review*, 136(3B), B864.
- [47] Kohn, W., & Sham, L. J. (1965). Self-consistent equations including exchange and correlation effects. *Physical review*, 140(4A), A1133.
- [48] Blöchl, P. E. (1994). Projector augmented-wave method. *Physical review B*, 50(24), 17953.
- [49] van Duin, A. C. T., Dasgupta, S., Lorant, F., & Goddard, W. A. (2001). ReaxFF: a reactive force field for hydrocarbons. *J. Phys. Chem. A*, 105(41), 9396–9409.
- [50] Chenoweth, K., van Duin, A. C. T., & Goddard, W. A. (2008). ReaxFF reactive force field for molecular dynamics simulations of hydrocarbon oxidation. *J. Phys. Chem. A*, 112(5), 1040–1053.
- [51] Plimpton, S. (1995). Fast parallel algorithms for short-range molecular dynamics. *J. Comput. Phys.*, 117(1), 1–19.
- [52] Aktulga, H. M., Fogarty, J. C., Pandit, S. A., & Grama, A. Y. (2012). Parallel reactive molecular dynamics: numerical methods and algorithmic techniques. *Parallel Comput.*, 38(4), 245–259.
- [53] Verlet, L. (1967). Computer "experiments" on classical fluids. I. Thermodynamical properties of Lennard-Jones molecules. *Physical review*, 159(1), 98.
- [54] Nosé, S. (1984). A unified formulation of the constant temperature molecular dynamics methods. *The Journal of chemical physics*, 81(1), 511-519.
- [55] Hoover, W. G. (1985). Canonical dynamics: equilibrium phase-space distributions. *Physical review A*, 31(3), 1695.

- 
- [56] Sorarù, G. D., Kundanati, L., Santhosh, B., & Pugno, N. (2019). Influence of free carbon on the Young's modulus and hardness of polymer-derived silicon oxycarbide glasses. *J. Am. Ceram. Soc.*, *102*(3), 907–913.
- [57] Saha, A., Raj, R. & Williamson, D. L. (2006). A model for the nanodomains in polymer-derived SiCO. *J. Am. Ceram. Soc.*, *89*(7), 2188–2195.
- [58] Newsome, D. A., Sengupta, D., Foroutan, H., Russo, M. F., & van Duin, A. C. T. (2012). Oxidation of Silicon Carbide by O<sub>2</sub> and H<sub>2</sub>O: a ReaxFF reactive molecular dynamics study, part I. *J. Phys. Chem. C*, *116*(30), 16111–16121.
- [59] Ponomarev, I., van Duin, A. C. T., & Kroll, P. (2019). Reactive force field for simulations of the pyrolysis of polysiloxanes into silicon oxycarbide ceramics. *J. Phys. Chem. C*, *123*(27), 16804–16812.
- [60] Gale, J. D. (1997). GULP: A computer program for the symmetry-adapted simulation of solids. *J. Chem. Soc., Faraday Trans.*, *93*(4), 629–637.
- [61] Gale, J. D., Raiteri, P., & van Duin, A. C. T. (2011). A reactive force field for aqueous-calcium carbonate systems. *Phys. Chem. Chem. Phys.*, *13*(37), 16666–16679.
- [62] Li, Z., & Bradt, R.C. (1987). The single-crystal elastic constants of cubic (3C) SiC to 1000° C. *J. Mater. Sci.*, *22*, 2557–2559.
- [63] Perdew, J. P., Burke, K., & Ernzerhof, M. (1996). Generalized gradient approximation made simple. *Physical review letters*, *77*(18), 3865.
- [64] Kresse, G., & Hafner, J. (1993). Ab initio molecular dynamics for liquid metals. *Phys. Rev. B*, *47*, 558.
- [65] Kresse, G., & Hafner, J. (1994). Ab initio molecular-dynamics simulation of the liquid-metal-amorphous-semiconductor transition in germanium. *Phys. Rev. B*, *49*, 14251.



- [66] Kresse, G., & Furthmüller, J. (1996). Efficiency of ab-initio total energy calculations for metals and semiconductors using a plane-wave basis set. *Comput. Mat. Sci.*, 6, 15.
- [67] Kresse, G., & Furthmüller, J. (1996). Efficient iterative schemes for ab initio total-energy calculations using a plane-wave basis set. *Phys. Rev. B*, 54, 11169.
- [68] Blöchl, P. E. (1994). Projector augmented-wave method. *Physical review B*, 50(24), 17953.
- [69] Rigby, D., & Roe, R. J. (1990). Molecular dynamics simulation of polymer liquid and glass. 4. free-volume distribution. *Macromolecules*, 23, 5312-5319.
- [70] Pan, F., Peng, F., & Jiang, Z. (2007). Diffusion behavior of benzene/cyclohexane molecules in poly(vinyl alcohol)-graphite hybrid membranes by molecular dynamics simulation. *Chem. Eng. Sci.*, 62(3), 703-710.
- [71] de Jong, B., Super, H. T. J., Spek, A. L., Veldman, N., Nachtegaal, G., & Fischer, J. C. (1998). Mixed alkali systems: structure and  $^{29}\text{Si}$  MASNMR of  $\text{Li}_2\text{Si}_2\text{O}_5$  and  $\text{K}_2\text{Si}_2\text{O}_5$ . *Acta Cryst.*, B54, 568–577.
- [72] Tranqui, D., Shannon, R. D., & Chen, H. Y. (1979). Crystal structure of ordered  $\text{Li}_4\text{SiO}_4$ . *Acta Cryst.*, B35 2479–2487.
- [73] Chou, C.-Y., & Hwang, G. S. (2013). Lithiation behavior of silicon-rich oxide ( $\text{SiO}_{1/3}$ ): a first-principles study. *Chem. Mater.*, 25(17), 3435–3440.
- [74] Chan, M. K., Wolverton, C., & Greeley, J. P. (2012). First principles simulations of the electrochemical lithiation and delithiation of faceted crystalline silicon. *J. Am. Chem. Soc.*, 134(35), 14362–14374.



## Appendix



Reactive MD-force field: C/O/Si force field  
39 ! Number of general parameters  
50.000000 !Overcoordination parameter  
9.546900 !Overcoordination parameter  
26.5405 !Valency angle conjugation parameter  
0.0000 !Triple bond stabilisation parameter  
0.0000 !Triple bond stabilisation parameter  
0.0000 !C2-correction  
1.058800 !Undercoordination parameter  
0.0000 !Triple bond stabilisation parameter  
12.117600 !Undercoordination parameter  
13.305600 !Undercoordination parameter  
0.0000 !Triple bond stabilization energy  
0.0000 !Lower Taper-radius  
10.0000 !Upper Taper-radius  
0.0000 !Not used  
33.866700 !Valency undercoordination  
6.089100 !Valency angle/lone pair parameter  
1.056300 !Valency angle  
2.038400 !Valency angle parameter  
0.0000 !Not used  
6.929000 !Double bond/angle parameter  
0.398900 !Double bond/angle parameter: overcoord  
3.995400 !Double bond/angle parameter: overcoord  
0.0000 !Not used  
5.779600 !Torsion/BO parameter  
10.000000 !Torsion overcoordination  
1.948700 !Torsion overcoordination  
0.0000 !Conjugation 0 (not used)  
2.164500 !Conjugation  
1.559100 !vdWaals shielding  
0.0010 !Cutoff for bond order (\*100)  
2.1365 !Valency angle conjugation parameter  
0.699100 !Overcoordination parameter  
50.000000 !Overcoordination parameter  
1.851200 !Valency/lone pair parameter



0.0000 !Not used  
0.0000 !Not used  
0.0000 !Molecular energy (not used)  
0.0000 !Molecular energy (not used)  
2.6962 !Valency angle conjugation parameter  
3 ! Nr of atoms; cov.r; valency;a.m;Rvdw;Evdw;gammaEEM;cov.r2;#  
alfa;gammavdW;valency;Eunder;Eover;chiEEM;etaEEM;n.u.  
cov r3;Elp;Heat inc.;n.u.;n.u.;n.u.;n.u.  
ov/un;vall;n.u.;val3,vval4  
C 1.3924 4.0000 12.0107 2.1841 0.073608 0.7920 1.1956 4.0000  
8.278687 1.5000 4.0000 27.5134 0.0000 6.7638 6.0000 0.0000  
1.1168 0.0000 0.0000 14.2732 24.4406 6.7313 0.0000 0.0000  
-4.1021 5.2529 0.0000 4.0000 2.9617 0.0000 0.0000 0.0000  
O 1.2477 2.0000 15.9990 1.9236 0.0904 1.0503 1.0863 6.0000  
10.2127 7.7719 4.0000 38.5944 0.0000 7.89268.9989 0.0000  
0.9088 1.0100 0.0000 20.4140 3.3754 0.2702 0.0000 0.0000  
-3.4588 2.7025 0.0000 4.0000 2.9225 0.0000 0.0000 0.0000  
Si 2.0291 4.0000 28.0600 2.0043 0.1247 0.8218 1.5023 4.0000  
13.0000 2.0618 4.0000 13.2088 0.0000 2.9322 7.3852 0.0000  
-1.0000 0.0000 0.0000 3.6038 8.5961 0.2368 0.0000 0.0000  
-3.1468 4.2105 0.0000 6.2998 2.5791 0.0000 0.0000 0.0000  
6 ! Nr of bonds; Edis1;LPpen;n.u.;pbe1;pbo5;l3corr;pbo6  
pbe2;pbo3;pbo4;n.u.;pbo1;pbo2;ovcorr  
1 1 76.2660 69.49424 52.0636 0.68125 -0.3636 1.0000 34.9876 1.0528  
3.69041 -0.1693 8.0804 0.0000 -0.0586 8.1850 1.0000 0.0000  
2 2 54.1463 158.6202 46.1430 -0.2802 -0.1244 1.0000 29.6439 0.9114  
0.2441 -0.1239 7.6487 0.0000 -0.1302 6.2919 1.0000 0.0000  
1 3 88.6687 1.5294 0.0000 0.3948 -0.5558 1.0000 17.2117 0.6721  
0.7672 -0.2085 7.7141 0.0000 -0.0909 5.4645 1.0000 0.0000  
2 3 284.7953 98.9409 50.3072 -0.3617 -0.3000 1.0000 36.0000 0.3527  
1.0607 -0.3684 4.6725 0.0000 -0.3975 4.5782 1.0000 0.0000  
1 2 150.4802 95.1693 23.3059 -0.3873 -0.1613 1.0000 10.8851 1.0000  
0.5341 -0.3174 7.0303 0.0000 -0.1463 5.2913 0.0000 0.0000  
3 3 72.8867 50.0318 30.0000 0.9983 -0.3000 1.0000 16.0000 0.1000  
1.0538 -0.0447 10.6176 0.0000 -0.1452 8.0404 0.0000 0.0000  
3 ! Nr of off-diagonal terms; Ediss;Ro;gamma;rsigma;rpi;rpi2  
1 2 0.1131 1.8523 9.8442 1.2775 1.1342 1.0621  
1 3 0.0318 1.5871 14.3990 1.5402 1.4279 -1.0000  
2 3 0.2073 1.8627 11.1116 1.5871 1.1632 -1.0000

18 ! Nr of angles;at1;at2;at3;Thetao,o;ka;kb;pv1;pv2;val(bo)

1	1	1	74.9085	46.0916	1.5663	0	0.0050	0.3556	2.5715
1	1	2	49.5561	7.3771	4.9568	0	0.7533	15.9906	1.0010
2	1	2	77.1171	39.8746	2.5403	0	1.7740	-42.9758	2.1240
1	2	1	74.3994	44.7500	0.7982	-24.3902	3.0000	0.0000	1.0528
1	2	2	77.9854	36.6201	2.0201	0	0.7434	67.0264	3.0000
2	2	2	80.7324	30.4554	0.9953	0	1.6310	50.0000	1.0783
3	3	3	71.6771	13.0081	3.6376	0	0.2384	0.0000	1.3185
2	3	3	79.8040	14.5686	6.3008	0	0.5590	0.0000	1.5404
2	3	2	74.5157	20.2102	2.4046	0	0.5463	0.0000	1.9054
3	2	3	25.8323	8.2183	3.3368	0	4.0000	0.0000	1.2809
2	2	3	53.7034	38.8349	7.5900	0	2.6430	0.0000	2.9367
1	1	3	61.4696	39.2472	0.9265	0	4.0000	0.0000	1.2334
1	3	1	81.9281	74.0099	1.0884	0	0.3867	0.0000	1.0816
3	1	3	66.5207	33.6220	3.3661	0	0.2121	0.0000	1.8864
1	3	3	69.5137	28.4326	1.2511	0	1.1385	0.0000	1.8352
1	2	3	37.9692	12.4930	3.8114	0	3.8885	0.0000	1.3498
1	3	2	68.9023	24.5811	0.9796	0	3.4865	0.0000	1.0400
2	1	3	59.2401	31.3887	2.7892	0	0.5392	0.0000	1.4564

10 ! Nr of torsions;at1;at2;at3;at4;;V1;V2;V3;V2(BO);vconj;n.u;n.u.

1	1	1	1	2.1207	26.8713	0.5160	-7.0599	-7.0306	0.0000	0.0000
1	1	1	2	-0.7098	22.2951	0.0060	-2.5000	-2.1688	0.0000	0.0000
2	1	1	2	-0.0528	6.8150	0.7498	-5.0913	-1.0000	0.0000	0.0000
1	1	2	1	2.0007	25.5641	-0.0608	-2.6456	-1.1766	0.0000	0.0000
1	1	2	2	-0.0179	5.0603	-0.1894	-2.5000	-2.0399	0.0000	0.0000
2	1	2	1	-2.5000	76.0427	-0.0141	-3.7586	-2.9000	0.0000	0.0000
2	1	2	2	-2.5000	66.3525	0.3986	-3.0293	-3.0000	0.0000	0.0000
1	2	2	1	2.5000	-0.5332	1.0000	-3.5096	-2.9000	0.0000	0.0000
1	2	2	2	0.0531	-17.3983	1.0000	-2.5000	-2.1584	0.0000	0.0000
2	2	2	2	-2.5000	-25.0000	1.0000	-2.5000	-1.0000	0.0000	0.0000

0 ! Nr of hydrogen bonds;at1;at2;at3;Rhb;Dehb;vhb1

